Effect of Subglacial Shear on Geomechanical Properties of Glaciated Soils

by

Bing Quan Huang

A dissertation submitted for the partial fulfillment of

degree of Master of Science

at

University of Saskatchewan

(Department of Civil and Geological Engineering)

Permission to Use

In presenting this thesis in partial fulfillment of the requirements for the degree of Master of Science from the University of Saskatchewan, I agree that the Libraries of this University may make it freely available for inspection. I further agree that permission for copying of this thesis in any manner, in whole or in part, for scholarly purposes may be granted by Dr. Jitendra Sharma who supervised my thesis work or, in his absence, by the Head of the Department or the Dean of the College in which my thesis work was done. It is understood that any copying or publication or use of this thesis or parts thereof for financial gain shall not be allowed without my written permission. It is also understood that due recognition shall be given to me and to the University of Saskatchewan in any scholarly use which may be made of any material in my thesis.

Requests for permission to copy or to make other use of material in this thesis in whole or part should be addressed to:

Head of the Department of Civil and Geological Engineering
57 Campus Drive
University of Saskatchewan
Saskatoon, Saskatchewan, S7N 5A9
Canada

Bing Quan Huang
Date:June 08, 2005

Abstract

Continental glaciers covered as much as thirty percent of the present-day inhabited earth during the Quaternary period. Traditionally, one-dimensional consolidation has been considered as the main process of formation for the soils deposited during glaciation. One of the outcomes of accepting one-dimensional consolidation as the main process of formation is that the geomechanical properties of soil in a horizontal plane are isotropic (known as cross-anisotropy). Recent measurements of subglacial pore pressure and preconsolidation pressure profile have indicated that this might not be the case. The role of subglacial shear action has probably been long neglected. The main objective of this research is to investigate the effects of subglacial shearing on the geomechanical properties of glaciated soils.

Recent research has found evidence of horizontal property anisotropy associated with the direction of the ice-sheet movement. A testing program was thus proposed to explore the relationship between the anisotropy of property and the direction of past glacier movement. The program involves several fundamental engineering parameters of soils. These parameters together with the corresponding test methods are as follows: (i) Conventional oedometer test – yield stress anisotropy; (ii) Oedometer test with lateral stress measurement – stiffness anisotropy; (iii) Load cell pressuremeter (LCPM) test – in situ stress anisotropy.

The physical meaning of yield stress determined by conventional oedometer tests was interpreted as the critical state of structural collapse. The literature review and an experimental study on kaolin samples with a known stress history suggested that yield stress possesses certain dependency on the sampling direction. The anisotropy of yield stress for Battleford till from Birsay, Saskatchewan was also explored by testing directional oedometer samples. In addition, the anisotropy of stiffness was also investigated using a newly developed lateral stress oedometer that is capable of independent measurement of horizontal stresses at three different points with angles of 120 degrees. Preliminary evidence of a correlation between the direction of maximum

stiffness in a horizontal plane and the known direction of glacial shear was observed. The correlation between the direction of maximum yield stress and known direction of glaciation was rather poor. Anisotropy of in situ stresses was investigated by conducting LCPM tests in Pot clay in the Netherlands. Based on the LCPM test results, it was concluded that the evidence of a correlation between the anisotropy of in situ stress and known direction of glacial advance is still rather obscure.

Although both the laboratory studies and field studies cannot sufficiently confirm the existence of lateral anisotropy of geomechanical properties and its relationship to the direction of the Quaternary ice-sheet movement, the effects of subglacial shearing should not be neglected in assessing the geotechnical properties of glaciated soils. In practice, it is usually found that the preconsolidation pressure profile does not follow the gravitational line as predicted by the one-dimensional consolidation theory and its magnitude is not compatible with the measured effective pressure values at the base of the glacier. It has been suggested that changes in seepage gradient (upward or downward) are responsible for the deviation of preconsolidation pressure profile away from the gravitational line. In this thesis, a new glacial process model – consolidation coupled shearing – was proposed. This model is based on the framework of traditional soil mechanics (critical state theory, Modified Cam-clay model and one-dimensional consolidation theory) and is consistent with the general geological and glaciological evidences. This model may provide an alternative explanation for the preconsolidation pressure patterns generally observed in practice. It can also be combined with groundwater flow characteristics to explain the diversity of the preconsolidation consolidation patterns. The proposed model was used successfully to obtain the preconsolidation pressure profile observed in Battleford till at Birsay and the subglacial shear-softening phenomenon.

Acknowledgements

The work presented in this thesis was carried out in the Department of Civil and Geological Engineering at the University of Saskatchewan under the direction of Professor Jitendra Sharma, to whom I am grateful for his invaluable suggestions and encouragement.

I would also like to thank other members of my Advisory Committee: Professor S. Lee Barbour, Professor Dennis E. Pufahl, and Mr. Jorge Antunes. I would also like to extend my appreciation to Laurent Gareau, not only for his helpful discussions but also for babysitting me at TU Delft; and to Alex Kozlow for his assistance in the Soil Laboratory.

I would also like to express my gratitude to Lyle Sinclair and the rest of the Saskatchewan Department of Highways and Transport rotary drilling crew for providing the directional undisturbed samples of Battleford till from Birsay, Saskatchewan.

I am also thankful for the financial support towards my research stipend provided by the Saskatchewan Department of Highways and Transport and the Natural Sciences and Engineering Research Council of Canada (NSERC).

Finally, but certainly foremost, I express my gratitude to my families, without whom this project would not have been completed. As son of my parents and father of my son, Chang-Chang, I owe them too much. In particular my thanks are due to my wife, Chao Zhu, who had to put up with me throughout the course of this work.

Contents

Notation

Roman

a_v	Coefficient of compressibility – Virgin compression
a_s	Coefficient of compressibility – Unloading-reloading
c_v	Coefficient of consolidation – Virgin compression
c_s	Coefficient of consolidation – Unloading-reloading
e	Void ratio
g	Gravitational acceleration
G'	Shear modulus
h	Total head
k	Coefficient of permeability
K_0	Coefficient of earth pressure at rest
K'	Bulk modulus
m_v	Coefficient of volume compressibility – Virgin compression
m_s	Coefficient of volume compressibility – Unloading-reloading
M	Critical state frictional constant (semi-axial ratio)
n	Porosity
N	Ordinate of the isotropic normal compression line at p'=1 kPa in e-lnp' space
OCR	Overconsolidation ratio
p'_0	Hardening parameter controlling the size of the yield locus
p'	Mean (volumetric) effective stress
q	Deviatoric stress
q_{surf}	Basal (penetrative) deviatoric stress
q_f	Deviatoric strength of a soil element
u_h	Hydrostatic pore-water pressure
u_e	Excess pore-water pressure
v	Discharge velocity
V	Specific volume

t	Time
W	Work done
z	Depth below the top of the soil layer

Greek

σ, σ'	Total and effective normal stresses, respectively
σ'_1, σ'_3	Major and minor effective principle stresses, respectively
τ	Shear stress
τ_{surf}	Basal (penetrative) shear stress
τ_f	Shear strength of a soil element
σ_p' , p'_c	Yield stress or preconsolidation pressure
ρ	Bulk density
ρ_w	Density of water
ρ_s	Density of soil particles
γ_w	Unit weight of water
φ'	Internal friction angle
ψ	Potential pore water pressure
η	Stress ratio (q/p')
λ	Gradient of the normal compression line in e-lnp' space
κ	Gradient of the swelling line in e-lnp' space
Γ	Ordinate of the critical state line at p'=1 kPa in e-ln p' space

List of Tables

List of Figures

Chapter 1 Introduction

In order to cope with the complex behaviour of soils in response to loading, geotechnical engineers rely on numerous simplifying assumptions. Whereas these assumptions are based on sound material behaviour models, such as Hooke's Law, and are generally supported by experience (i.e., satisfactory performance of structures), the fact is that a high degree of uncertainty arises from these necessary assumptions. One fundamental assumption made routinely in geotechnical practice is that soils are "cross-anisotropic", which infers that geomechanical properties (e.g. stiffness, in situ stresses, permeability, etc.) in the horizontal plane are isotropic. Elasticity and one-dimensional consolidation theories certainly support this conclusion for soils consolidated under geological sedimentation and/or erosion. Unfortunately, this underlying conclusion is tacitly assumed for soils that have been affected by processes other than one-dimensional consolidation and rebound, such as glaciated soils. Published data on the properties of glaciated clays and tills (Sauer et al. 1990; Boulton and Dobbie 1993; Sauer et al. 1993) suggest one-dimensional consolidation models that depend significantly on the boundary conditions imposed. All of these models assume that glaciated soils reach their present (overconsolidated) state as a result of compression under the effective (or buoyant) weight of glacier ice followed by erosion. None of these models considered shearing during glacial advance and its effect on the formation of soils.

There is considerable evidence available that demonstrates that shear deformation broadly exists beneath ice sheets. One of the key evidences comes from the field measurements at Breidamerkurjökull, Iceland (Boulton and Jones, 1979). Here, a tunnel system was dug in the ice about 1 to 2 m above the glacier sole and probes were inserted into the underlying till at several points (Fig 1.1(a)). The probes consisted of a series of contiguous annuli which fitted around a central rod and which could be detached by a counter-clockwise turn. The probe was inserted to depths varying from 0.6 to 0.85 m, and the central rod was withdrawn. The narrow access holes were then sealed off using wooden plugs. After a period of 10 days, the till was partially drained by pumping. The annuli were carefully excavated and their positions plotted.

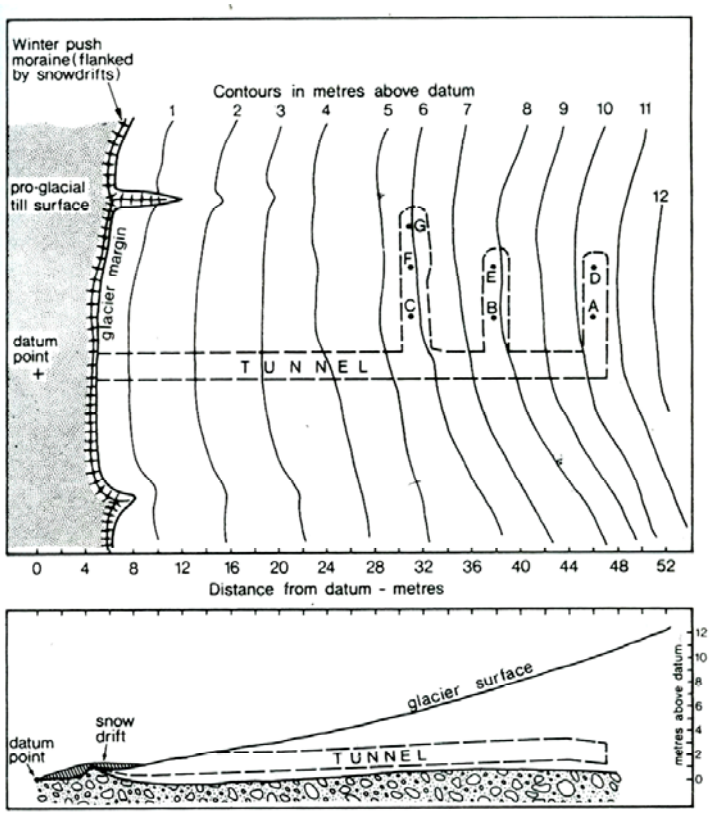

(a)

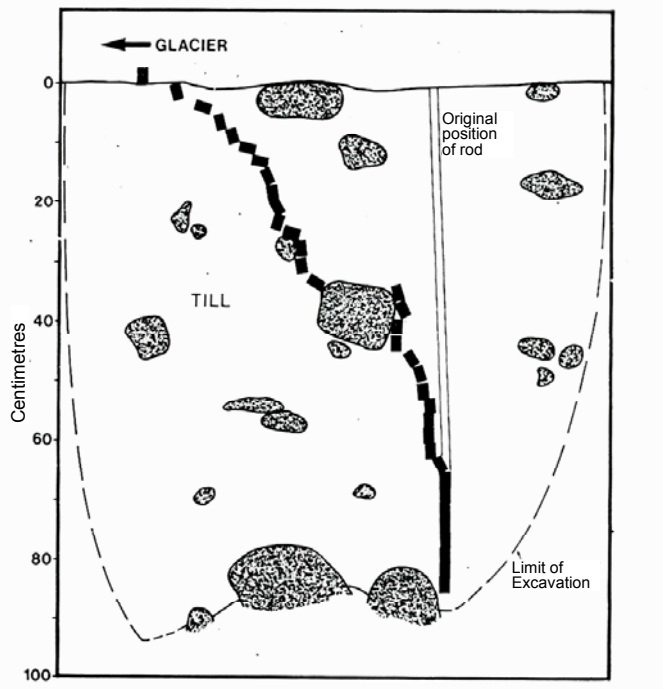

(b)

Fig 1.1 (a) The plan of the tunnels and the positions of successful subglacial probes at Breidamerkurjökull, Iceland; (b) The position of individual annuli at probe A 244h after their original emplacement (Boulton and Jones, 1979)

Water pressures had been measured by piezometer at each site during the whole process. Fig 1.1(b) shows the results at one site. It was found that about 90% of the total basal movement of the glacier is contributed by deformation of the bed materials and only 10% by slip between the glacier sole and till surface. Subglacial shear deformations have also been observed to occur beneath ice stream B, West Antarctica (Alley et al., 1986; Engelhardt et al., 1990) and Trapridge glacier, Canada (Blake and Clarke, 1989). Such deformation can occur when subglacial drainage is so poor that high pore water pressures build up in the sediment immediately beneath the glacier sole, resulting in loss of strength of the sediment and subsequent shear deformation (Boulton, 1996).

Several articles in the published literature suggest anisotropic horizontal stresses that likely occurred as a result of glacial shearing (Dalton and Hawkins, 1982; Douma and Helbig, 1990; Schokking, 1998). Anisotropic lateral stresses suggest that one-dimensional consolidation may not be the main process that resulted in the present stress state of these clays. Clearly, there is a need to examine the effect of subglacial shear stresses on the geomechnical properties of glaciated soils. By studying the mechanics of glaciation vis-à-vis measurements on glaciated soils, significant contributions can be made to our understanding of spatial distribution of soil properties leading to a reduction in uncertainty in geotechnical design of structures founded on glaciated soils.

1.1 Objectives of the Research Program

The main goal of the research program is to provide answers to the following fundamental questions that relate to glaciated soils:

1. Are yield stresses (as measured in a conventional oedometer test) anisotropic?
2. Is stiffness (as given by the ratio of horizontal to vertical effective stress) anisotropic?
3. Are in situ stresses anisotropic?
4. Is there a correlation between anisotropy of yield stresses, stiffness and in situ stresses and the known direction of glacial advance?
5. What is the effect of subglacial shear on the variation of preconsolidation pressure with depth?

From theoretical considerations of continuum mechanics and plasticity theory, the yield surface of a laterally anisotropic soil should have different orientation and shape in general stress space compared to a yield surface of an isotropic or cross-anisotropic soil. This is due to the preferred orientation of yield stresses in the horizontal plane. As one of the fundamental engineering properties of soils, yield stress can be easily measured by routine geotechnical laboratory tests (e.g. oedometer test). Therefore, the first objective is to obtain evidence of yield stress anisotropy in the horizontal plane. As mentioned above, anisotropic yield stresses must also exhibit orientation dependence. Therefore, the experiments designed to characterize yield stress anisotropy should also focus on establishing this preferred orientation and correlating it with past stress-strain history of the soil.

The concept of cross-anisotropy, i.e. a constant ratio of horizontal to vertical effective stress (known as the coefficient of earth pressure at rest, K_0) irrespective of the radial orientation in the horizontal plane at a given depth is ingrained in the traditional one-dimensional deposition and consolidation model that is generally assumed to apply to all the soils. As mentioned above, there is strong evidence that subglacial shear may have played an important role in the formation of glaciated soils. Therefore, the second objective is the characterization of the stiffness (or K_0) anisotropy in the horizontal plane. This objective was achieved by testing high-quality undisturbed samples of glaciated soils in a newly developed oedometer apparatus that is capable of measuring horizontal stresses in three different radial directions.

The third objective is to obtain evidence of anisotropy of in situ horizontal stresses as a consequence of shear stresses imposed by the glacier overrun. This objective was achieved by conducting several Load Cell Pressuremeter (LCPM) tests in situ in a clayey soil deposited in the valleys during glacial retreat and overrun by subsequent glaciation. An LCPM is a self-boring type of pressuremeter that can install itself (with minimum disturbance to the surrounding soil) at any given depth in a soil and measures in situ lateral stresses using six load cells mounted around its periphery. In its present form, it is not suitable for testing in tills because of the presence of gravel-sized particles. Therefore, the in situ stress measurements using LCPM were conducted in a fairly uniform clay layer.

The fourth objective is to confirm if there is any correlation between the anisotropy of yield stress, stiffness and in situ stresses with known directions of glacial advance. The directions of glacial advance are established using published glaciogeology literature.

It is generally observed that the patterns of preconsolidation pressure (yield stress in vertical direction) do not follow a gravitational gradient but are almost constant with depth (e.g. Sauer et al., 1993; Shaw and Hendry, 1998). Additionally, their magnitudes are not consistent with measured effective vertical stresses at the base of present day glaciers. The fifth objective of the research program is to examine the role of subglacial basal shear in imparting observed patterns of preconsolidation pressures in glaciated soils. This objective was achieved by coupling consolidation and shear effects in the framework of traditional soil mechanics, i.e. Terzaghi's theory of one-dimensional consolidation and critical state theory, in combination with an elastoplastic soil constitutive model. The resulting model is used to "predict" the preconsolidation pressure profiles for one of the glaciated soils of Saskatchewan.

1.2 Scope of the Research Program

In order to draw general conclusions about the effect of subglacial shear on geomechanical properties of glaciated soils, it is mandatory to investigate the behaviour of several different glaciated soils taken from several different geographical locations. However, this research is limited to investigation of just two natural soils: a glaciated soil, namely Battleford till, from Birsay in Saskatchewan and a fine-grained glaciolacustrine soil that has been overrun by glaciers, namely Pot clay, from Marum in the Netherlands. Battleford till from Birsay was selected because of relatively horizontal ground conditions at Birsay and the convenience and the ease with which directional undisturbed samples could be obtained. The choice of using Pot clay for in situ stress measurements was beyond the control of the author; it was chosen by the researchers at Technical University Delft, largely on the basis of the availability of fair amounts of published data on this soil.

Additional tests have been performed using kaolin samples prepared in lab by consolidating kaolin slurry under precise loading conditions. The objectives of these

tests are to calibrate new equipment and to check the validity of certain assumptions and hypotheses.

The proposed coupled shearing model that is used to obtain the patterns of preconsolidation pressure in glaciated soils is based on an axisymmetric stress condition (commonly known as triaxial condition in soil mechanics) and isotropic soil behaviour. It is possible to incorporate a more realistic plane strain condition and anisotropic soil behaviour into this model. However, it is believed that the accuracy that could be achieved by consideration of such details will never exceed the uncertainties of the geological process itself. A complicated model may also end up masking the essential features of the effect of subglacial shear.

In light of the rather limited scope of the research program, the reader is advised to refrain from deriving general conclusions on the behaviour of glaciated soils. Clearly, more results (and their statistical interpretation) are needed in order to achieve a better understanding of the role of subglacial shear in imparting anisotropic geomechanical properties to glaciated soils.

1.3 Structure of the Thesis

In Chapter 1 (this chapter), the framework of the research program and its main objectives are presented.

Chapter 2 provides a comprehensive review of the literature pertaining to glaciated soils.

In Chapter 3, the details and the results of conventional oedometer tests conducted to explore yield stress anisotropy are presented.

Chapter 4 gives the details and the results of tests performed using the newly developed lateral stress oedometer to investigate the stiffness anisotropy.

Chapter 5 deals with the measurement of anisotropy of in situ stresses using the Load Cell Pressuremeter.

In Chapters 3, 4 and 5, the existence of a correlation between anisotropic properties and the known orientation of the Quaternary ice sheet advance is also assessed.

In Chapter 6, a new glacial deposition process model – consolidation coupled with shearing – is proposed. Preconsolidation pressure patterns obtained using this model are compared with observed preconsolidation pressure patterns for a glaciated soil from the province of Saskatchewan.

In Chapter 7, the main findings of this research program are summarized and recommendations are given for further research on this topic.

Derivations and formulations of key equations used in this thesis are presented in Appendices towards the end of this thesis.

Chapter 2 Review of the Literature

2.1 Introduction

This chapter gives an overview of the engineering geology of glacial soils. Several theories of subglacial deformation and deposition are reviewed. In particular, the one-dimensional consolidation theory applied on glacial soils is discussed in detail so as to reveal its essential feature - an effective stress-volume-drainage relationship along the depth in the sediment. A review of other literature relevant to the research program is also presented in this chapter.

2.2 Relevant Geological and Glaciological Theories

2.2.1 Thermal regimes

Both proglacial deformation and subglacial deformation can act upon frozen or unfrozen sediments (Echelmeyer and Wang, 1987; Boulton, 1996). However, theoretical analysis and most geological evidences suggest that unfrozen subglacial deformation should be more common beneath the Quaternary ice sheets. This unfrozen condition is due to high friction heating by the deforming ice (e.g. Hart, 1995; Boulton, 1996).

2.2.2 Bed conditions

There are two types of conditions associated with subglacial ice sheet/sediment interface (Hart, 1995): (i) Hard-bed conditions, where glaciers are overlying undeformable beds, i.e., hard igneous and metamorphic rocks or well drained soft sediments; and (ii) Soft-bed conditions, where glaciers are overlying soft unconsolidated sedimentary rocks or till. Since large areas of the Pleistocene glaciers in the mid-latitudes of Europe and North America were underlain by thick, unlithified sediment sequences (Hart, 1995; Boulton, 1996; Fowler, 2003), this thesis will be limited to the study of the soft-bed conditions.

2.2.3 Glacial drainage system

Field investigations and theoretical studies during the past decades prove that a network of passages enable water to percolate through a temperate glacier. The passage tends to

close by plastic deformation due to the overburden pressure. On the other hand, energy generated by viscous dissipation in the water flow continually enlarges the passage by melting its wall. Theoretical models have been developed by numerous researchers based on the analysis of these two competing processes (Shreve, 1972; Hooke, 1984).

A typical drainage system in temperate glacier will consist of three distinct parts – superglacial, englacial and subglacial (Shreve, 1972). In subpolar glaciers that are at the melting temperature only at or near their beds, or in temperate glaciers during winter, the entire superglacial portion and part or the entire englacial portion will be missing. The subglacial part is the most complicated among them, due to the presence of a sediment load and the influence of bed topography. It is also the only part to leave a permanent record after a glacier retreats. In general, subglacial water is discharged by one or a combination of the following patterns: (i) through channels at the ice-bed interface; (ii) in a sheet between a glacier and its bed; (iii) by groundwater flow through subglacial sediments and rocks.

2.2.4 Classification of subglacially-deformed materials

Several classification systems for subglacially deformed materials can be found in the literature. Most of these classification systems are built up based on the corresponding deformation characteristics. Some of these classification systems are reviewed here.

Banham (1977) introduced the term glacitectonite that refers to the general subglacially-deformed rocks and sediments, and described an idealized fourfold vertical sequence of subglacial structure that consists of (from the base up):

(i) undeformed parent material (i.e. bedrock or sediment),
(ii) parent material with non-penetrative deformation structure,
(iii) parent material with penetrative deformation structure, and
(iv) till.

Different amounts of primary structure are reserved in divisions (ii) and (iii). Division (iv) was originally termed endiamict glaciotectonite, and consists of materials that have been so highly remoulded by subglacial shear that all primary structures have been destroyed and the material is homogenized. Both far travelled and local material may be categorized into division (iv).

Hart and Boulton (1991) used a different terminology to describe the same fourfold vertical sequence recognized by Banham (1977), which was called (from the bottom up):

(i) the undeformed zone,

(ii) the overturned zone,

(iii) the sheared zone, and

(iv) the homogeneous zone.

Benn and Evans (1996) proposed a general classification of subglacially-deformed materials in which styles of subglacial deformation were taken into account. Deformation till was defined as homogenized, usually diamictic material formed by glacially induced shear of subsole materials. Glaciotectonite refers to materials that have undergone subglacial shear but retain some of the structural characteristics of the parent material (equivalent to the divisions (ii) and (iii) suggested by Banham, 1977).

2.2.5 Subglacial deformation, erosion and deposition processes

When glaciers move over a deformable bed, it has been shown by many authors (e.g. Boulton and Jones, 1979; Boulton and Hindmarsh, 1987; Boulton and Dobbie, 1993; Hart, 1995) that there is a strong coupling between the glacier and the underlying bed deformation. This subglacial deformation could be a major determinant of the dynamic behaviour of the ice sheet. The main points can be summarized as follows:

1) There exists a self-adjusted subglacial drainage system. Subglacial shear deformation occurs when drainage is so poor that high pore water pressures and thus low effective pressures (even equal to zero) develop in the bed.
2) Beneath the sole, a tectonic structure is defined (Fig 2.1: Case (c)): "A-Horizon within which shear deformation tends to cause dilation of the grain skeleton, producing a much lower density than in the underlying, undeformed and consolidated B-Horizon".
3) Sediments in the A-Horizon deform as a "viscous fluid". The rate of erosion (E) could be defined as:

$$E = \frac{\delta Q_A}{\delta x} \tag{2.1}$$

where Q_A = the horizontal flux of sediment within A-horizon.

4) Erosion will occur when *E* is positive, i.e. more material enters the deforming A-Horizon; and deposition will occur when *E* is negative, i.e. more material leaves the deforming A-Horizon (Fig 2.2).
5) The deformation, erosion and/or deposition processes are temporally and spatially dynamic processes through a complete glacial cycle.

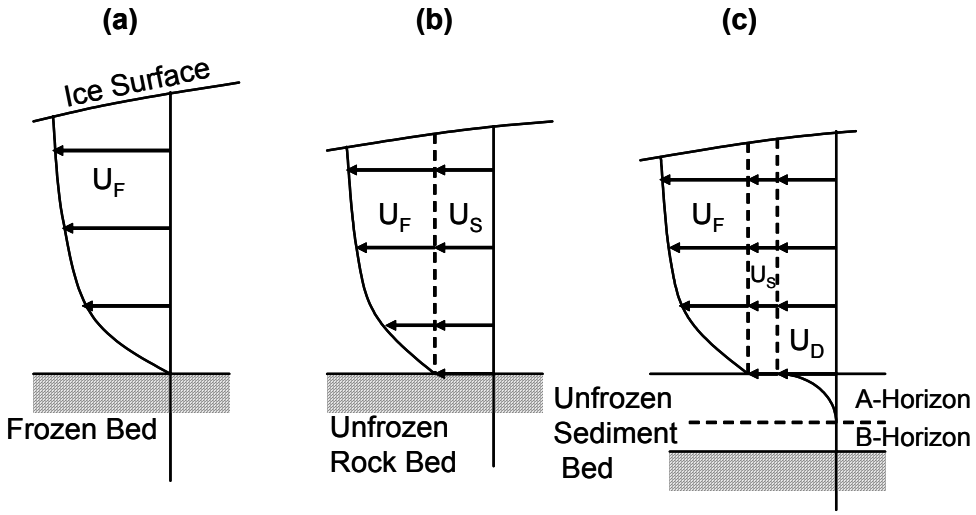

Fig 2.1 Subglacial deformation model (after Boulton, 1996) [U_F – Internal flow velocity; U_S – Basal sliding velocity; U_D – Subglacial deformation velocity; Case (c) is for an unfrozen deforming bed condition]

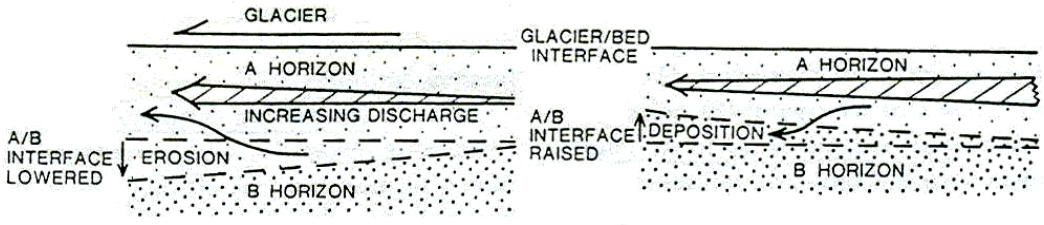

Fig 2.2 The conditions for erosion and deposition on an unfrozen deforming bed (Boulton, 1996)

Theoretically, the subglacial zone can be divided into four parts longitudinally along the ice sheet (Fig 2.3): the marginal area, the equilibrium line area, the intermediate area and the divide area (Hart, 1995). At the margin area, there is low basal shear action but high rate of deposition along with active glaciotectonic deformation. In the equilibrium line area, the basal shear action increases and there is active glaciotectonic deformation and an interaction of erosion and deposition. In the divide area, there is very low basal shear strain and little, if any, deformation, deposition and erosion.

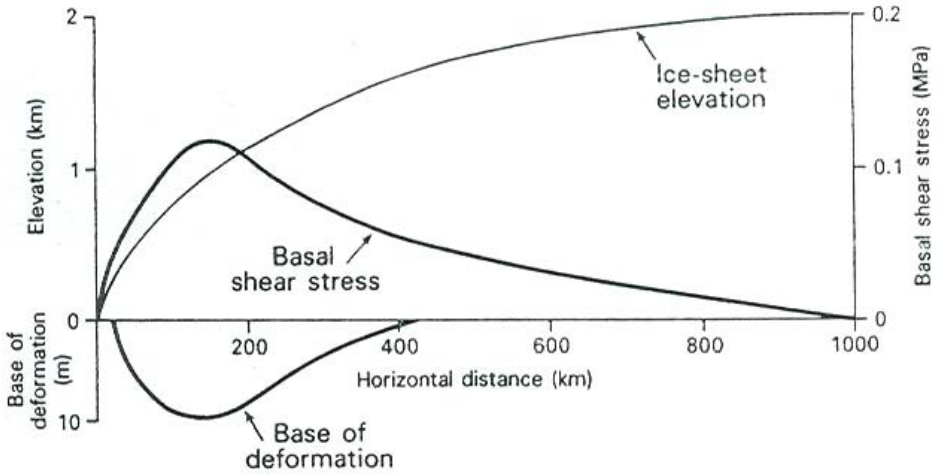

Fig 2.3 Theoretical subglacial shearing-deformation environment: marginal area approximately 0-20 km; equilibrium line area approximately 20-200 km; divide area approximately 800-1000 km (Hart, 1995).

2.3 Formation Process Models for Glaciated Soils

2.3.1 Flint's model

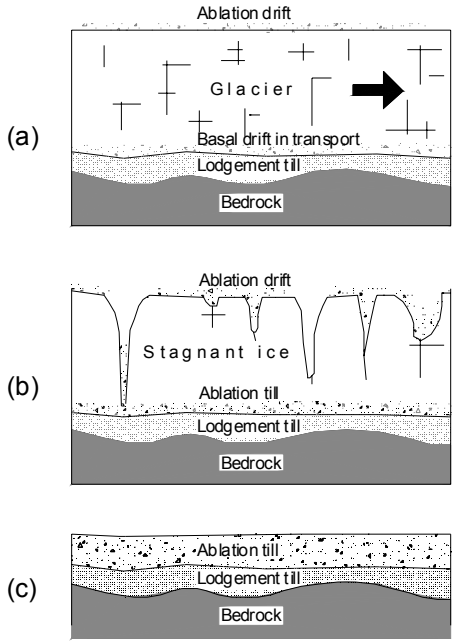

Fig 2.4 Flint's (1971) model for deposition of glaciated soils: (a) active glacier; (b) stagnant ice; (c) final sedimentation

Flint's (1971) model proposes that there are two depositional processes occurring underneath an ice sheet: melt-out that consists of the passive melting out of debris underneath a stagnant ice mass, and lodgement that is essentially a frictional process by which basal debris is plastered against the underlying substrate (Fig 2.4). The fundamental difficulty with Flint's model is that it fails to deal with the basic physics of the stress environments within the glaciers in terms of hydraulics and the principles of effective stress. For instance, Sauer et al. (1993) reported that preconsolidation pressures in pre-Battleford tills in Saskatchewan were generally in the range of 1800 ± 200 kPa, where the ice was known to be over 1000 m thick (9000 kPa).

2.3.2 Sauer's model

Sauer et al. (1993) presented a temperate glacier model (Fig 2.5) to explain the origin of the preconsolidation pressures in the pre-Battleford formations. The temperature of the ice within a temperate glacier is approximately at the pressure melting point throughout its thickness. Thus, the subglacial sediments are not frozen and an abundance of free water exists within the glacier. Under this environment a network of drainage channels throughout the glacier maintained a steady "hydraulic grade line" within the ice. This hydraulic grade line served as a potentiometric surface for the subglacial sediments. In southern Saskatchewan, a steady hydraulic grade line averaging 210 ± 30 m below the surface of the Laurentide glacier would have produced preconsolidation pressures of 1800 ± 200 kPa consistently over such a large area.

Sauer et al. (1993) suggested that the Battleford formation was formed in a stagnant ice environment (Fig 2.6). When the ice stagnated, it melted from the top down because of warming atmospheric conditions, and from the bottom upwards because of the geothermal flux. This resulted in two sedimentary and stress environments occurring simultaneously in the stagnant ice fields creating (i) surface ablation till released from the surface and originally normally consolidated by its own weight, and (ii) subglacial till released from the basal zone preloaded to a moderately overconsolidated state from the overlying stagnant ice. In addition, it was found that the preconsolidation pressures in the till and intertill clays were more or less constant with depth, i.e. they did not follow a gravitational gradient (geostatic stresses increasing with depth at a rate of about 10 kPa/m).

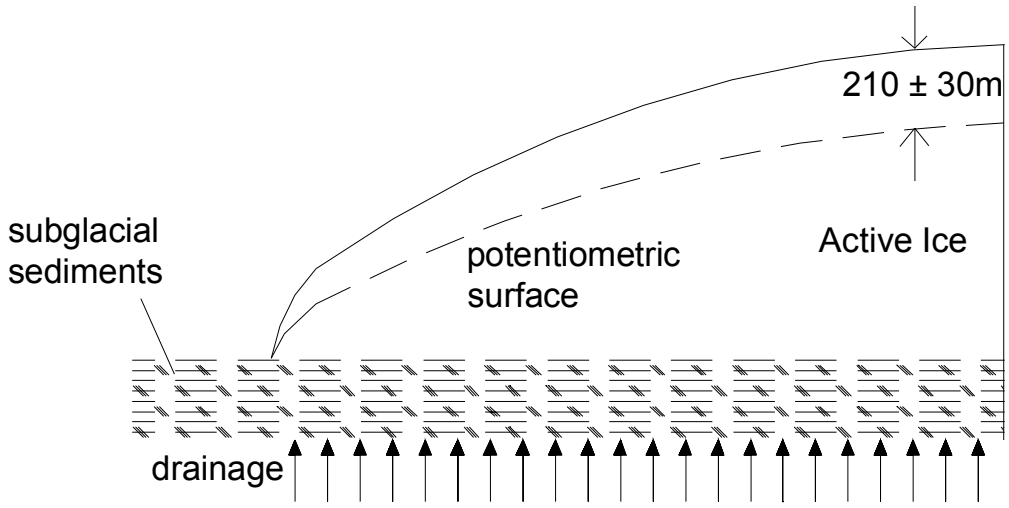

Fig 2.5 Sauer's temperate glacier model for consolidation behaviour of pre-Battleford formations (after Sauer et al., 1993)

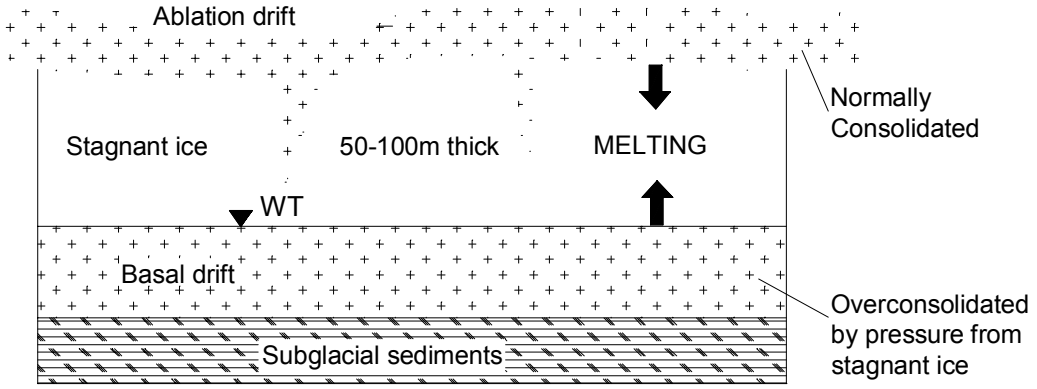

Fig 2.6 Sauer's stagnant glacier model for consolidation behaviour of Battleford formation (after Sauer et al., 1993)

2.3.3 Feeser's model

From a structural geology viewpoint, Feeser (1988) presented a glacial process model on the basis of the genesis of joints and fissures found in Lauenberg Clay from northern Germany. On the basis of careful logging of conjugate pairs of joints, he proposed that these joints are formed as a result of unloading of the ground during glacial retreat. It can be argued that such pairs of joints could just as easily be formed during glacial advance in response to basal shear stresses. The observation of fairly low levels of

effective stresses underneath modern day glaciers (Fountain, 1994; Boulton, 1996) also appears to cast doubt over the rebound of ground during glacial retreat as the main reason for the formation of these joints. He observed that a majority of these joints have a rough texture, indicating their formation during a brittle failure of the ground. He concluded that brittle failure of the ground during glaciation is possible only when the ground is frozen. Therefore, Feeser's model appears to contradict theoretical analysis and most geological evidences that suggest that unfrozen subglacial deformation should be more common beneath the Quaternary ice sheets.

In Feeser's model, the stress paths experienced by the ground during glacial advance and retreat are categorized into four distinct phases: pre-glacial phase, glaciodynamic phase, glaciostatic phase and post-glacial phase (Fig 2.7). He suggested that the orientations of principal stress axes would be changed as the glacier approaches, rotating along the direction of the glacier movement. In this respect, Feeser's model acknowledges the effect of shear stresses applied by the ice sheet on the in situ stress state in the underlying ground. It is likely that the deforming ground is undergoing consolidation at critical state during the glaciodynamic phase. However, for the reasons mentioned above (low basal effective stresses), the in situ stress scenarios predicted by Feeser's model during the glaciostatic and post-glacial phases, particularly the existence of a horizontal major principal stress, are probably unlikely.

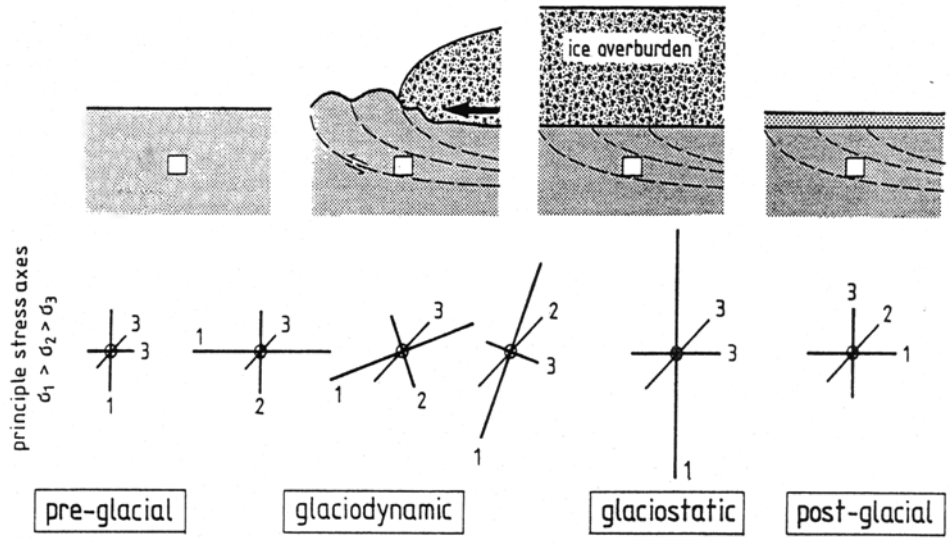

Fig 2.7 Stress history during a complete glaciation cycle proposed by Feeser (1988)

2.3.4 Boulton and Dobbie's model

Boulton and Dobbie (1993) suggested that the state of consolidation of subglacial sediments was determined by: (i) the basal melting rate; (ii) the distribution of subglacial permeability and the ease of draining into the proglacial environment; (iii) the effective pressure-dependent flow law for the sediments; (iv) the extent of the glacier. It was shown that the preconsolidation pressure profile could greatly exceed or be approximately gravitational depending on the permeability of the aquifer.

2.3.5 Casagrande's hypothesis

As mentioned above, numerous researchers have developed theories to explain the consolidation behaviour of glaciated soils. All of these are one-dimensional consolidation models and depend significantly on the boundary conditions imposed. In fact, these theories can be retraced back to Casagrande's hypothesis (1936). One of the reasons that the preconsolidation pressure profile deviates from the gravitational gradient can be due to the effect of the potential water pressure gradient in the vertical direction.

One-dimensional consolidation theory has long been considered as the fundamental mechanism on the formation process of soils and is of great significance in practice. Consolidation is a gradual process of increasing the density of a saturated soil by draining some of the water out of the voids. This process continues until the excess pore water pressure dissipates. Sediments, subjected to a greater effective vertical stress at some time in the past than that at present, are said to be overconsolidated whereas those that have never experienced a vertical effective stress greater than its present value are said to be normally consolidated. The ratio of maximum past vertical effective stress over present vertical effective stress is defined as overconsolidation ratio (OCR). The maximum past vertical effective stress is termed preconsolidation pressure. Consolidation is commonly described with a spring analogy (e.g. Holtz and Kovacs, 1981). This sort of description usually conceals its essential feature – an effective stress-volume-drainage relationship along the depth in the sediment. Consider the following cases:

Case 1:

Consider a saturated sediment layer with the water table at the top surface of the layer. If the layer is not loaded and there is no water flowing into or out of the layer, the effective stress (σ') at any point within the sediment is the difference between the total stress (σ) and the hydrostatic pore water pressure (u_h):

$$\sigma' = \sigma - u_h = (\sigma')_g \tag{2.2}$$

where $(\sigma')_g$ is the effective stress due to self-weight of soil (solid + water). The vertical effective stress gradient ($\partial\sigma'/\partial z$) will be completely gravitational:

$$\frac{\partial\sigma'}{\partial z} = \frac{\partial\sigma}{\partial z} - \frac{\partial u_h}{\partial z} \tag{2.3}$$

$$\frac{\partial\sigma'}{\partial z} = (1-n)(\rho_S - \rho_W)g = \left(\frac{\partial\sigma'}{\partial z}\right)_g \tag{2.4}$$

where ρ_W = density of water, ρ_S = density of soil particles, n = porosity, g = gravitational acceleration and $(\partial\sigma'/\partial z)_g$ = gravitational effective stress gradient.

Case 2:

When this sample is subjected to a normal stress ($\delta\sigma$) at its surface, the effective stress (σ') at any point within the sediment, given by the difference between the total stress ($\sigma + \delta\sigma$) and the pore water pressure ($u_h + u_e$), becomes

$$\sigma' = (\sigma + \delta\sigma) - (u_h + u_e) = (\sigma')_g + \delta\sigma' \tag{2.5}$$

where $\delta\sigma' = \delta\sigma - u_e$ and u_e is the excess pore-water pressure. If the interstitial water is not allowed to escape, the increase in total vertical stress is carried entirely by the pore water (i.e. $\delta\sigma = u_e$, $\delta\sigma' = \delta\sigma - u_e = 0$), the effective stress (σ') and its vertical gradient

($\partial\sigma'/\partial z$) will not change. If the sample is permitted to drain at the base, a common consolidation process occurs. During this process, the burden of the external load ($\delta\sigma$) will be gradually transited from the interstitial water to the solid skeleton. This process continues until the drainage ceases (i.e. $u_e = 0$). Eventually, the effective stress (σ') at any point within the sediment is given by

$$\sigma' = (\sigma + \delta\sigma) - u_h = (\sigma')_g + \delta\sigma \tag{2.6}$$

Since $\delta\sigma$ is constant, the vertical effective stress gradient ($\partial\sigma'/\partial z$) will not change.

Case 3:

The sample is still subjected to a normal stress ($\delta\sigma$) at its surface. If a downward (or upward) seepage is allowed by keeping a constant total head difference between the top and the bottom of the sample, the soil will consolidate to a greater (or smaller) density. This process continues until the seepage reaches a steady state (i.e. the volume of water flowing into the sample is equal to that flowing out of it). Eventually, the effective stress (σ') at any point within the sediment becomes

$$\sigma' = (\sigma + \delta\sigma) - (u_h + u_e) = (\sigma')_g + (\delta\sigma - u_e) \tag{2.7}$$

Since a steady seepage exists within the sediment sample, a vertical excess pore-water pressure gradient ($\partial u_e/\partial z$) develops. And the vertical effective stress gradient ($\partial\sigma'/\partial z$) is given by

$$\frac{\partial\sigma'}{\partial z} = \left(\frac{\partial\sigma'}{\partial z}\right)_g - \frac{\partial u_e}{\partial z} \tag{2.8}$$

$$\frac{\partial\sigma'}{\partial z} = (1-n)(\rho_S - \rho_W)g - \frac{\partial u_e}{\partial z} \tag{2.9}$$

Suppose that the potential gradient will cause water to escape at a rate (v) given by Darcy's law:

$$v = \frac{-k}{\rho_W g}\frac{\partial u_e}{\partial z} \tag{2.10}$$

where k = coefficient of permeability. Because permeability and porosity are dependent on effective stress, both the excess pore-water pressure gradient ($\partial u_e / \partial z$) and the vertical effective stress gradient ($\partial \sigma' / \partial z$) are non-linear with depth.

2.3.6 Discussion

Based on a review of existing models for the formation of glaciated soils, it can be concluded that all of these models (with the exception of Feeser's (1988) model) do not take into account the basal shear stress applied by the glaciers. All these models are primarily based on one-dimensional consolidation theory and rely on particular boundary conditions to explain the spacing/orientation of joints or fissures or the patterns of preconsolidation pressure observed in glaciated soils. Only Feeser's model appears to acknowledge the possibility of inducing anisotropic stress states in the ground deforming underneath the glacier. It is evident that a ground that has experienced rotation of principal stresses during the glaciodynamic phase is likely to consolidate differently from a ground that has experienced no such rotation. Clearly, there is a need to explore the role played by basal shear stresses in modifying the in situ stress state. In particular, the possibility of the existence of anisotropic geomechanical properties (stiffness and strength) in glaciated soils is worth investigating both theoretically and experimentally. From an experimental point of view, a device that can measure horizontal (lateral) stresses during the consolidation (and swelling) process would be quite useful in the assessment of anisotropy of geomechanical properties. Several such devices have been described in the literature; these will be reviewed in the next section.

2.4 Lateral Stress Measurement using Oedometer

It has long been recognized that an accurate determination of K_0 is important for a variety of geotechnical analysis (e.g. foundations, embankments, excavations). The in situ vertical effective stress at any depth can be easily determined if the unit weight of the soil and location of the water table are known, but the determination of horizontal

stress is always a challenge. In laboratories, many experimental techniques and equipment for the measurement of the lateral stress have been presented by many researchers. The oedometer ring and the triaxial cell with a special device are the basis of all these developments. Some typical designs of the oedometer type are reviewed as follows:

2.4.1 Brooker and Ireland (1965)

The arrangement developed by Brooker and Ireland (1965) is shown in Fig 2.8. As an axial load is applied to a soil specimen, the strains in the surrounding steel membrane are registered by electrical resistance strain gauges. By adjusting the hydraulic pressure (through a pair of solenoid valves) in the oil behind this membrane a null strain condition can be maintained. The corresponding hydraulic pressure is equal to the lateral pressure.

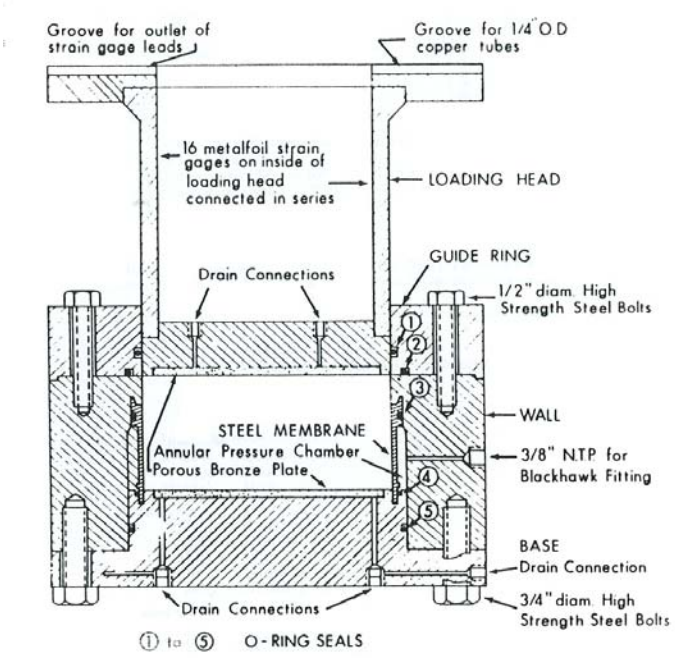

Fig 2.8 Equipment with lateral stress measurement used by Brooker and Ireland (1965).

2.4.2 Dyvik et al. (1985)

Fig 2.9 shows the cross-sectional view of the arrangement developed by Dyvik et al. (1985) to measure the lateral stress around an oedometer specimen. The central portion of the inside vertical face of the ring contains a Teflon membrane. Behind this

membrane is a chamber that completely surrounds the perimeter of the specimen and is filled with de-aired water. A very stiff and sensitive pressure transducer is directly connected to the chamber fluid and measures the lateral stress.

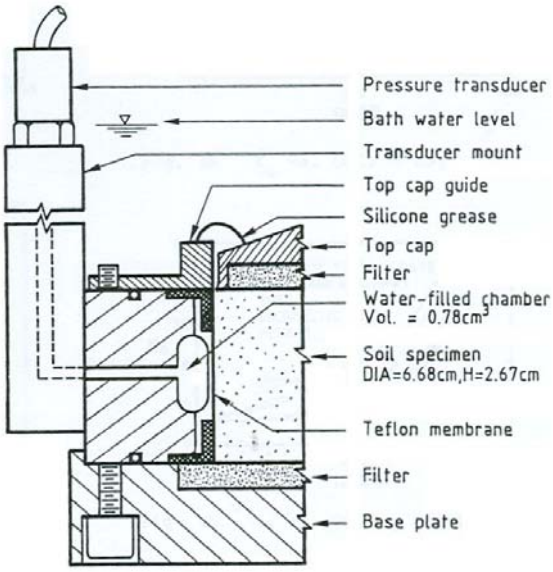

Fig 2.9 Equipment with lateral stress measurement used by Dyvik et al. (1985).

2.4.3 Senneset (1989)

The lateral stress oedometer developed by Senneset (1989) is shown in Fig 2.10. The supporting ring was split into three parts. In each part of the ring a sensitive LVDT records the contact pressure between sample and ring during the oedometer test. By this design, several advantages can be obtained. The mounting of an undisturbed sample is easy as the ring is clamped around the sample. The three separated parts of the split ring allow the application of a controlled initial contact pressure state. It is also possible to perform a test with a controlled lateral deformation. However, the zero lateral strain condition is not satisfied for this design.

2.4.4 Colmenares (2001)

In the lateral stress oedometer developed by Colmenares (2001), there are four diaphragms of 10 mm diameter located orthogonally around the ring wall (Fig 2.11). The diaphragms are equipped with strain gauges. A hydraulic pump is connected to the oil reservoir behind the diaphragms, and pressure is applied to maintain a null average strain condition in the diaphragms. The oil pressure is assumed to be the average radial

stress acting on the specimen. It should be pointed out that most of the developments similar to the above, including the corresponding data interpretations, are implicitly based on an "average horizontal stress" assumption.

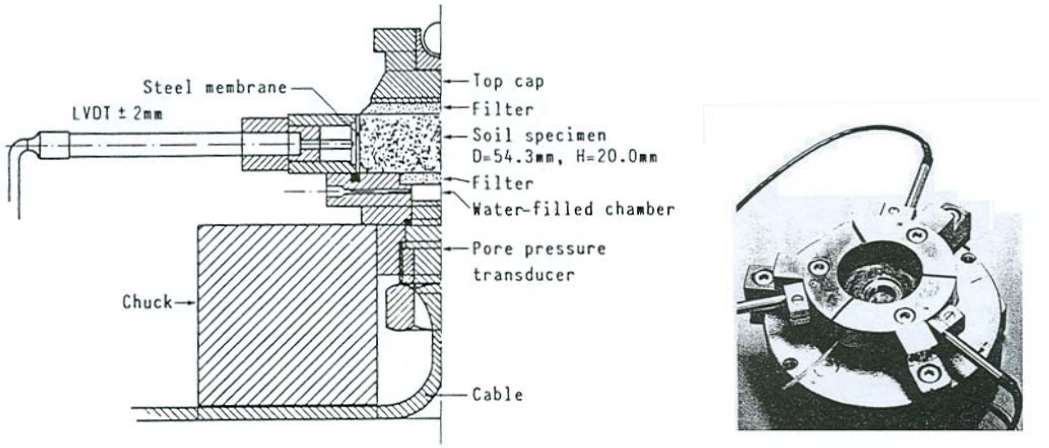

(a) (b)

Fig 2.10 Equipment with lateral stress measurement used by Senneset (1989). (a) Simplified cross-section of the ring; (b) The split ring

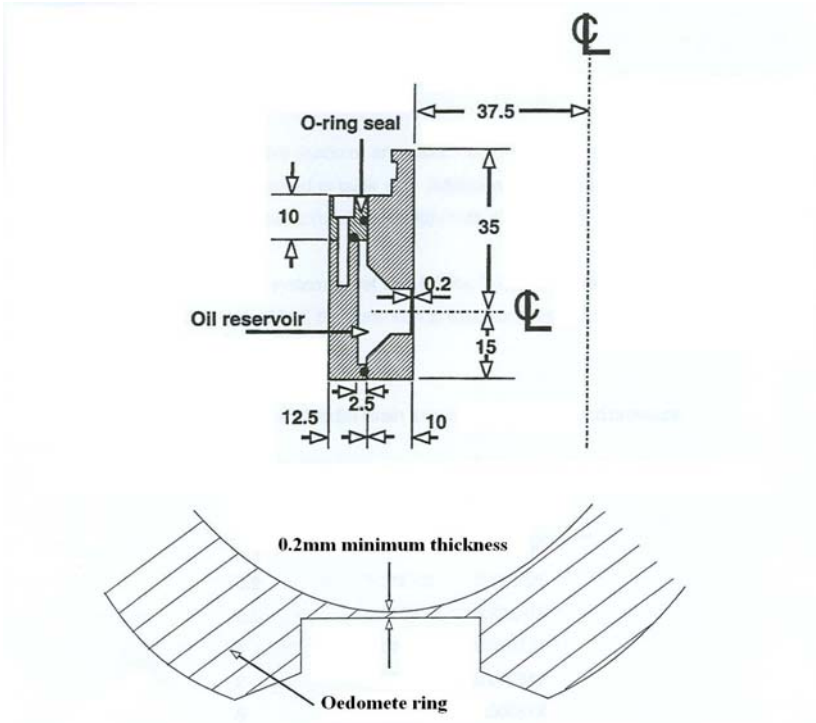

Fig 2.11 Equipment with lateral stress measurement used by Colmenares (2001). (top) Vertical section; (bottom) Horizontal section.

2.4.5 Discussion

It can be seen from the review of various oedometers capable of measuring lateral stresses that none of these oedometers are capable of measuring anisotropic lateral stresses while maintaining the condition of zero lateral strain. Such a measurement is possible using independent pressure cells located along different radial directions in the horizontal plane. Only the design proposed by Senneset (1989) is capable of achieving such a measurement but it cannot satisfy the condition of zero lateral strain. Therefore, a new oedometer (called the lateral stress oedometer) has been designed for the current research program. Its design details and operations procedure can be found in Chapter 4. It should also be pointed out that laboratory measurement of anisotropy is likely to suffer from disturbance to which a soil could be subjected during the sampling or during its insertion into the oedometer ring. This can be avoided by conducting in situ measurement of anisotropy using a self-boring pressuremeter equipped with several load cells along its periphery. Such a device can be installed inside a borehole with minimum disturbance to the surrounding soil. It can be used to measure the stresses as the surrounding soil closes around it. Details of this device are given in Chapter 5.

2.5 Summary

From the review of relevant literature, it can be concluded that there is a strong case for the study of the effect of subglacial shear on the geomechanical properties of glaciated soils. In particular, the possibility of anisotropic geomechanical properties as a consequence of subglacial shear should be explored. Since the geotechnical practice assumes (or expects) all the natural soils to be cross-anisotropic (isotropic in lateral direction), almost all the routine experimental techniques are geared towards testing such soils. Therefore, there is a need to develop innovative equipment capable of testing truly anisotropic soils.

There is also a need to explain the inconsistency between the observed patterns of preconsolidation pressure and the relatively low values of effective stresses measured at the base of modern day glaciers. It is likely that the basal shear stress that has been ignored by all the deposition models has a role to play in imparting such preconsolidation pressure patterns to glaciated soils.

Chapter 3 Measurement of Yield Stress Anisotropy

3.1 Background

In geotechnical engineering practice, the consolidation characteristics of soils with low permeability are often determined using the oedometer test. The rate and the magnitude of deformation can be predicted with reasonable accuracy from oedometer test results. Oedometer test results are also important from the point of view of establishing the stress history of natural soils, especially, marine clays and glacial tills. For instance, these simple laboratory tests can provide information leading to a better understanding of the processes associated with glaciation.

The results of an oedometer test are usually interpreted using Casagrande's method (Casagrande, 1936; see also Holtz and Kovacs, 1981) which is based on the analysis of an e-log σ' curve where e is the void ratio of the soil sample and σ' is the vertical effective stress acting on the soil sample. Fig 3.1 shows such a typical e-log σ' curve obtained from an oedometer test. This curve is usually divided into two distinct sections: the unloading-reloading curve and the virgin compression curve. The maximum effective stress level that the sample has experienced during its geological history corresponds to a marked difference in the slopes of the two sections of the e-log σ' curve. This level of stress is termed the preconsolidation pressure, σ_p'.

In addition to Casagrande's method, several other methods of estimating preconsolidation pressure have been proposed; for instance, the work per unit volume approach (Becker et al., 1987), the bilogarithmic approach with the ln(1+e)-ln p' plot (Butterfield, 1979) or the log(1+e)-log p' plot (Oikawa, 1987) or the ln(1+e)-log p' plot (Onitsuka et al., 1995). Almost all of these methods (with the exception of the method proposed by Becker et al., 1987) establish preconsolidation pressure using an empirical observation of a change in soil compressibility.

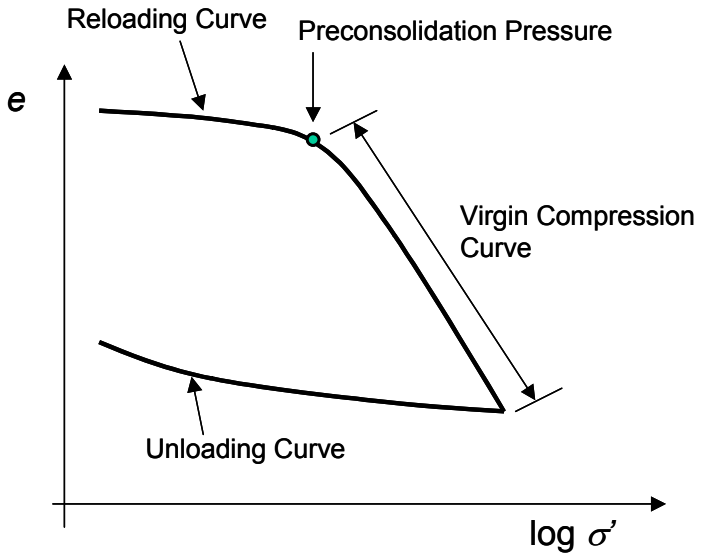

Fig 3.1 A typical consolidation curve in oedometer tests.

Before we draw the conclusion that we can use any of these techniques for the interpretation of the oedometer tests data, the preconsolidation pressures defined in all these approaches should be theoretically verified as identical (and therefore representing identical physical meanings). Obviously, the semi-logarithmic and bilogarithmic methods are essentially identical: both are based on the relationship between the void ratio and the pressure. The only difference lies at the skill of the mathematical treatment. Many researchers found that ambiguous values of compression-swelling indices and preconsolidation pressure are obtained for natural clays when the data is analyzed using the *e*-log σ' plot. This is because the logarithmic values of void ratio (*e*) better fit the actual variation of the consolidation process than the arithmetic values of *e*. Also, Onitsuka et al. (1995) proved that the preconsolidation pressures defined by the work method and the bilogarithmic method are theoretically identical. This can be demonstrated as follows:

(i) Based on the work approach, the bilinear relationship between W and p' can be expressed as:

$$W = A_{i1} + B_{i1} \times \sigma' \quad [\mathrm{i} = 1, 2] \tag{3.1}$$

(ii) Based on the bilogarithmic method (e.g. natural logarithm), the bilinear relationship in the bilogarithmic plots can be expressed as:

$$\ln(1+e) = A_{i2} + B_{i2} \times \ln(\sigma') \qquad [\text{i} = 1, 2] \tag{3.2}$$

For both approaches, the stress at the intersection point is defined as the preconsolidation pressure. From Becker et al. (1987), the work done per unit volume, W, to the material can be expressed as:

$$W = \int (\sigma_1' d\varepsilon_1 + \sigma_2' d\varepsilon_2 + \sigma_3' d\varepsilon_3) \tag{3.3}$$

where σ_1', σ_2' and σ_3' are principal effective stresses and $d\varepsilon_1$, $d\varepsilon_2$ and $d\varepsilon_3$ are increments of principal strains.

For an oedometer test, equation (3.3) can be rewritten as:

$$W = \int \sigma' d\varepsilon_V \tag{3.4}$$

where σ' is the vertical effective stress acting on the oedometer sample. Through substituting (3.4) into (3.1) and differentiating, we have $B_{i1}(d\sigma'/d\varepsilon_V) = \sigma'$. According to the definition of volumetric strain $d\varepsilon_V = de/(1+e)$, we have:

$$d\varepsilon_V = de/(1+e) = B_{i1}(d\sigma'/\sigma') \qquad [\text{i} = 1, 2] \tag{3.5}$$

Integrating Eq. (3.5), we have:

$$\ln(1+e) = A_{i3} + B_{i3} \times \ln(\sigma') \qquad [\text{i} = 1, 2] \tag{3.6}$$

This is similar to Eq. (3.2). Therefore, the preconsolidation pressures defined in all these approaches are theoretically identical.

3.2 Preconsolidation Pressure or Yield Stress?

The oedometer test data for natural clays reported by Becker et al. (1987) demonstrates that the work incremental rate dW/dp' increases dramatically at an intersection point in the W-p' plot. This phenomenon can only be explained as the complete collapse of the bonds of natural clays at the intersection point (Onitsuka et al., 1995). Therefore, the

physical meaning responsible for the stress value at the intersection point in the work approach is definite for natural clays, that is, this stress level corresponds to the critical state of structure collapse. In this sense, the so-called preconsolidation pressure determined using the oedometer tests should not be simply comprehended as the maximum "historical memory". Burland (1990) recommends that that the term "yield stress" is more precise. The term "preconsolidation pressure" should be reserved for situations in which the magnitude of such a pressure can be established by geological means. Similarly the term "overconsolidation ratio" (OCR) should be reserved for describing a known stress history. Otherwise the term "yield stress ratio" (YSR) should be used.

3.3 Tests on Kaolin Samples

3.3.1 Apparatus

Kaolin slurry was consolidated in a 15 cm diameter Rowe cell in accordance with British Standard BS1377-6:1990 (BSI, 1990a). Oedometer tests were conducted using a consolidation rig with a 50 mm diameter fixed ring in accordance with British Standard BS1377-5:1990 (BSI, 1990b). Loading was applied using dead weights with a lever ratio of 11 to 1. Settlement and swelling of the sample were recorded using analogue dial gauges with a range of 25 mm and a resolution of 0.002 mm.

3.3.2 Sample preparation

First, the liquid limit of the kaolin powder was determined using both the Casagrande apparatus as well as the fall cone apparatus. The average value of the liquid limit for the kaolin powder was found to be 52%. Five kg of dry kaolin powder was then mixed mechanically with 3.25 kg of distilled water. Therefore, the water content of the resulting slurry was equal to 1.25 times the liquid limit. The slurry was allowed to settle for at least 24 hours under its own weight. The slurry was then consolidated in a Rowe cell. The maximum imposed axial effective stress was 250 kPa. On completion of primary consolidation at this stress, a "cake" of kaolin was formed inside the Rowe cell. This "cake" was completely unloaded (i.e. allowed to swell freely), removed from the Rowe cell, and stored in a humid environment. Six oedometer specimens were trimmed

from the kaolin "cake". Two specimens were trimmed horizontally, two were trimmed vertically and two were trimmed at inclinations of 21° and 35° with respect to vertical. The material left over after trimming of the oedometer specimens was used to determine the water content of the kaolin "cake".

3.3.3 Testing procedure

At the beginning of an oedometer test, the sample was saturated using the constant volume method. Vertical load was applied at the top of the sample using the conventional load increment ratio (LIR = 1). During the oedometer tests, each individual load increment was applied for a sufficient period to permit primary consolidation to occur and to minimize the secondary compression effects. Typically, the loading duration varied between 60 and 180 minutes. Once the specimen had finished consolidating under the maximum pressure (around 1600 kPa), it was unloaded in stages with each successive load roughly one fourth of the preceding load (e.g. 1600 kPa, 400 kPa, 100 kPa, 25 kPa). Sufficient readings were taken to verify that rebound was essentially complete. After unloading was finished and the final load was released, the specimen was dismantled quickly; the excess water was wiped from the ring and specimen and the combined weight of the ring and the sample was recorded. The sample was then placed in a 110°C oven for water content determination.

3.3.4 Results and discussions

The oedometer results for a typical, horizontally trimmed kaolin specimen interpreted using the five different methods (Casagrande, 1936; Oikawa, 1987; Onitsuka et al., 1995; Butterfield, 1979; Becker et al., 1987) are shown in Fig 3.2. The summary of yield stresses that were determined using the five different methods is given in Table 3.1. Yield stresses obtained using different methods agreed reasonably well with each other. It can be seen from Table 3.1 that the yield stresses for the horizontally trimmed (H) samples are about 60-70% of the maximum imposed loading, about 72-78% for the inclined (I) samples and about 90% for the vertically trimmed (V) samples. In this sense, these results are fairly consistent with the data reported by Becker et al. (1987). Therefore, it can be inferred that the yield stress determined by conventional oedometer

test exhibits certain dependence on the direction of sampling and this dependence is related to the stress condition that the soil is subjected to in corresponding direction.

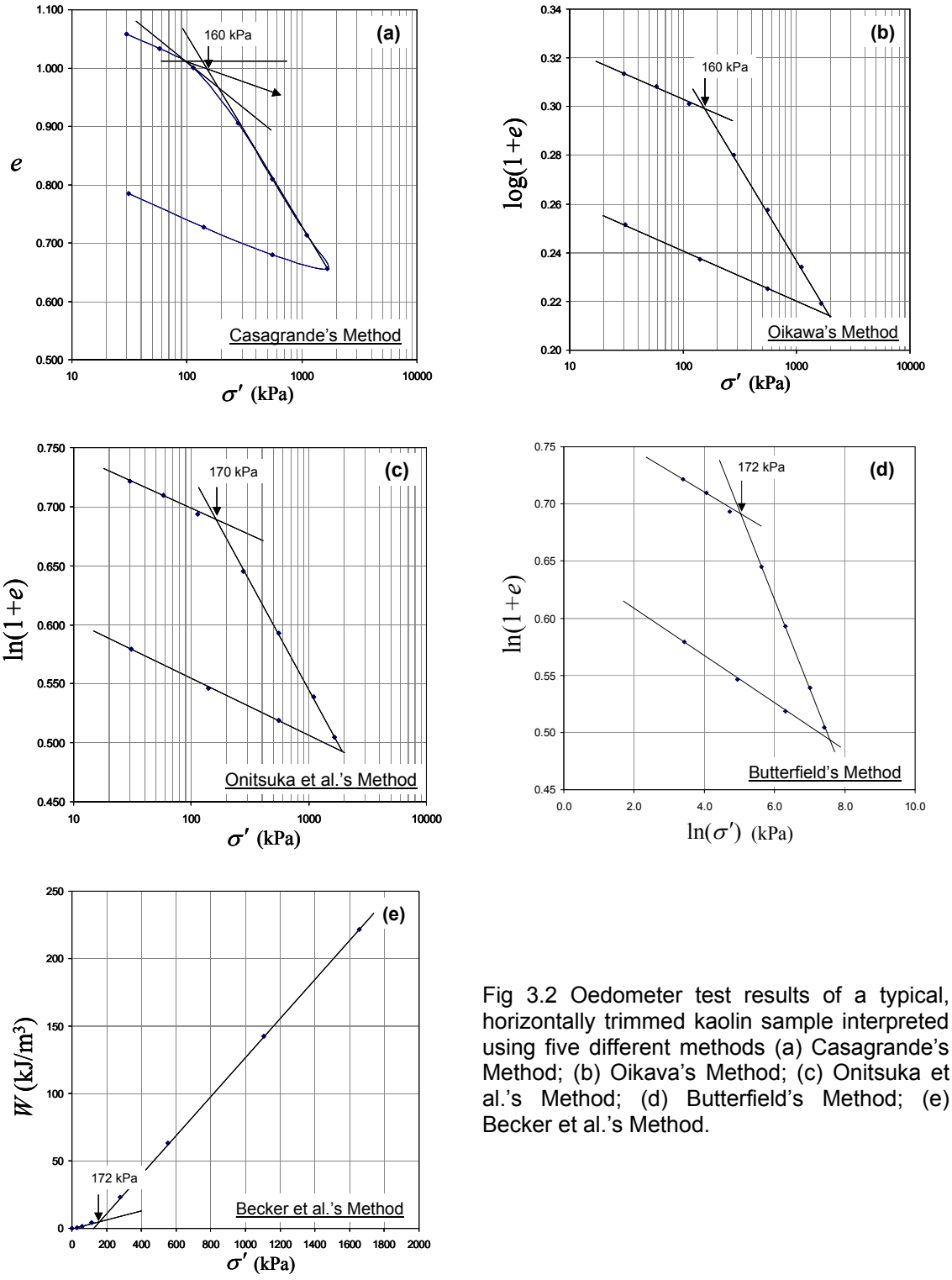

Fig 3.2 Oedometer test results of a typical, horizontally trimmed kaolin sample interpreted using five different methods (a) Casagrande's Method; (b) Oikava's Method; (c) Onitsuka et al.'s Method; (d) Butterfield's Method; (e) Becker et al.'s Method.

Table 3.1 Summary of yield stress values for all the kaolin samples

Sample #	**1**	**2**	**3**	**4**	**5**	**6**
Orientation	H	I	V	H	I	V
Casagrande	160	180	210	160	175	205
Ratio (%)	64	72	84	64	70	82
Oikawa	160	180	220	160	190	220
Ratio (%)	64	72	88	64	76	88
Onisuka	170	195	235	175	200	235
Ratio (%)	68	78	94	70	80	94
Butterfield	172	192	221	174	191	221
Ratio (%)	69	77	88	70	76	88
Becker	170	195	230	170	190	230
Ratio (%)	68	78	92	68	76	92
Average Ratio:		H – 67%		I - 76%		V - 89%

It should be pointed out that:

(1) Although all the specimens were trimmed from the same kaolin "cake", their boundary conditions during the stage of formation in the Rowe cell are different: the vertical and horizontal directions are associated with stress-controlled and strain-controlled boundary conditions, respectively. In the subsequent oedometer tests, the imposed boundary condition for the V- samples exactly reflects the original boundary condition. However, for the H- samples, the boundary condition changes from a strain-controlled boundary condition to a stress-controlled boundary condition. The influence of this boundary condition change on the yield stresses was not investigated in the present study.

(2) The test results clearly show the influence of the boundary conditions during the unloading of the kaolin cake in Rowe cell prior to the trimming of oedometer samples. As the vertical stress is removed from the top surface of the kaolin cake, the horizontal (radial) stress is also removed. However, the cake is allowed to swell only in the vertical direction. Therefore, it recovers most of the strain experienced in the vertical direction but not in the horizontal direction. Khera and Schulz (1984) have shown that if an overconsolidated soil is allowed to

recover part or all of the strain while in contact with water, a lower value of yield stress is obtained. This could be the reason that the H- samples can "remember" the maximum past stress more exactly than the V- samples. Using a K_0 value of 0.69 for kaolin (Airey, 1984; Al-Tabbaa, 1984), we obtain maximum past horizontal stress to be 0.69 x 250 = 172.5 kPa. This is quite close to the measured yield stress for H- samples. For the V- samples, the measured yield stress is only 89 % of the maximum past vertical stress.

3.4 Tests on Undisturbed Battleford Till Samples

3.4.1 Battleford Till

As mentioned before, undisturbed directional samples of Battleford till were collected from Birsay in Saskatchewan, Canada. Fig 3.3 shows the geographical location of the sampling site.

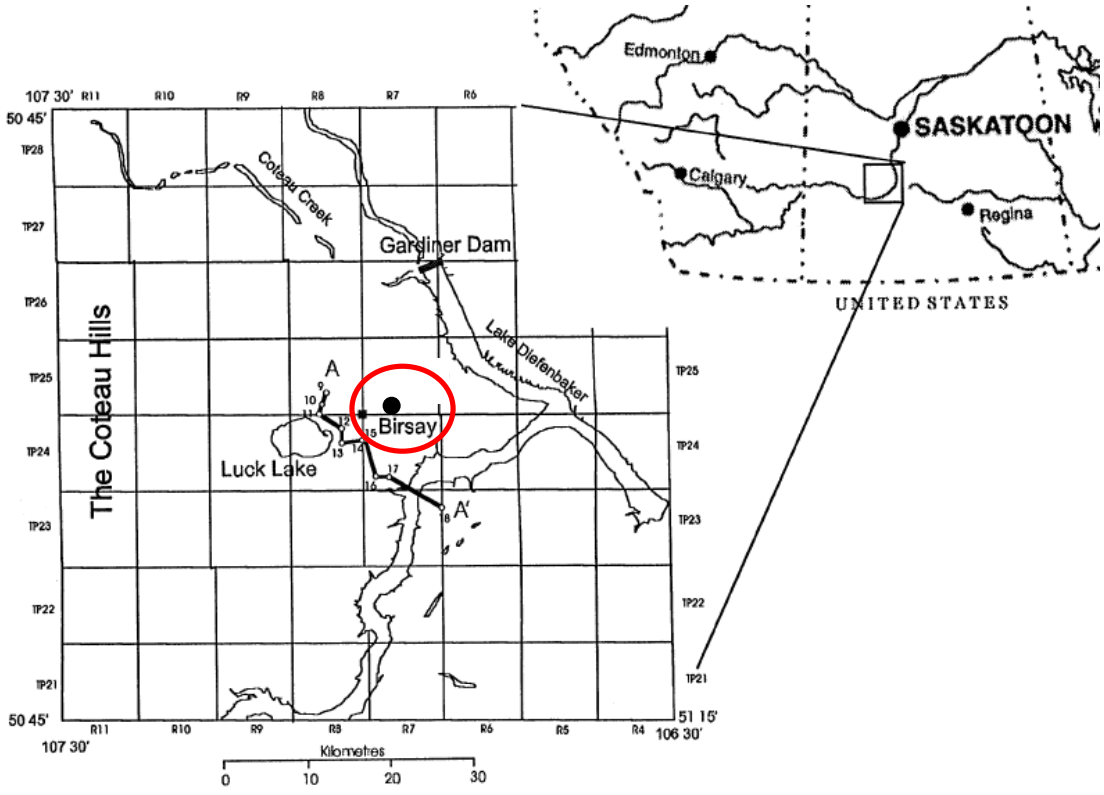

Fig 3.3 Geographical location of Birsay, Saskatchewan (after Shaw and Hendry, 1998)

For each of the undisturbed sample, the direction of magnetic north was established by positioning the rotary drilling rig using an on-board Global Positioning System (GPS). Samples were collected using 76 mm diameter thin-walled, open drive samplers. All the samples were sealed using paraffin wax at the site to prevent moisture loss during transportation and subsequent storage. The depth of sampling was between 8 and 42 m. Geological and geophysical analysis indicated that all samples were obtained within the Battleford formation.

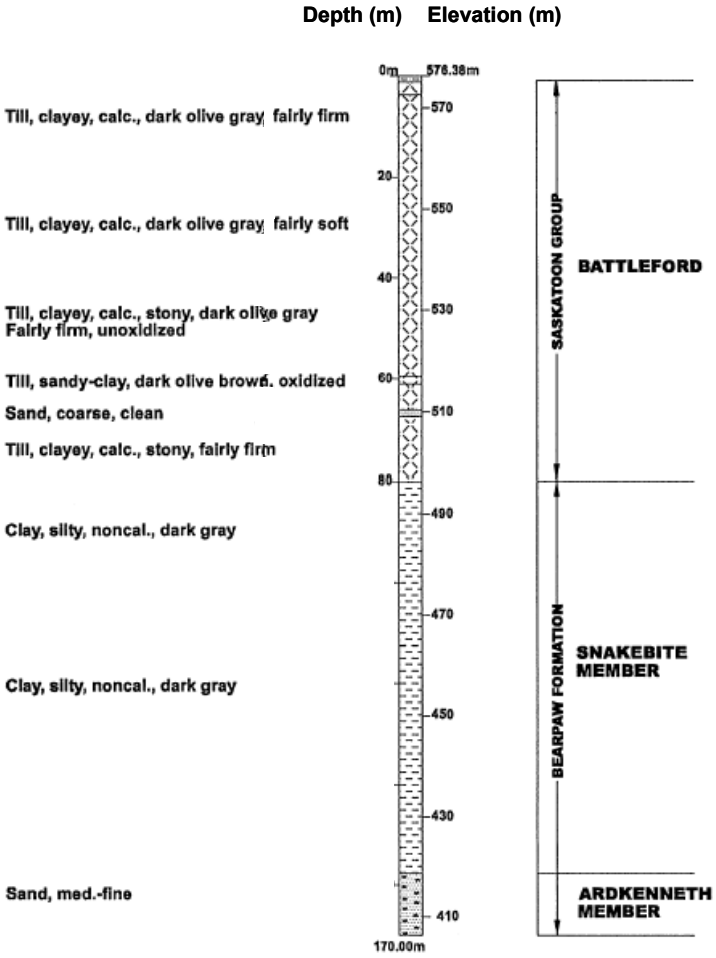

Fig 3.4 Ground profile at Birsay, Saskatchewan showing Battleford till overlying Cretaceous shale of Bearpaw Formation (after Shaw and Hendry, 1998)

Fig 3.4 shows the ground profile at Birsay, Saskatchewan obtained by Shaw and Hendry (1998). In general, for the Saskatchewan Rivers Plain, the Saskatoon Group (Christiansen, 1968) is composed of lower and upper tills of the Floral Formation, tills

of the Battleford Formation, and surficial stratified deposits that are chiefly glaciolacustrine clays. The Battleford Formation is composed of a lower till unit (basal melt-out) and an upper till and clay unit (ablation melt-out) (Sauer and Christiansen, 1991).

At Birsay, about 80 m thick layer of Battleford till lies unconformably over Cretaceous shale of the Bearpaw Formation. The Battleford glaciation is the youngest known glacial episode (equivalent to the Weichselian glaciation). Although an estimated 7 glacial episodes have been interpreted in the Saskatchewan Rivers Plain (Christiansen, 1992) it appears that the till sheets from the older glaciations were either never deposited at this site, or were eroded during advance of the Battleford ice sheet.

3.4.2 Apparatus

The conventional equipment with fixed oedometer ring and dead-weight loading of lever ratios of 11, 8, or 7 was used. The deflection of the specimens was measured with dial gauges reading directly to 0.001 mm.

3.4.3 Sample preparation

Several (usually five) specimens were continuously trimmed from the same tube: one in the vertical direction and the others in some random horizontal directions. Specimens were acquired in the laboratory by carefully hand-trimming the parent sample to the correct diameters of the stainless rings. The material left over after trimming of a specimen was used to determine the water content of the specimen. Core samples that showed penetration of drilling fluid or distortion from pebbles were discarded. A total of twenty specimens were successfully tested in the oedometer.

3.4.4 Experimental techniques

The experimental techniques that were followed during the testing are summarized below:

(1) A careful determination of the initial height and weight of the specimen was made prior to each oedometer test. It was, therefore, possible to make an important crosscheck between computed and measured overall compression thus ensuring that there were no major inaccuracies in the test results. The

compressibility of the loading frame and the oedometer apparatus was neglected.

(2) In order to make primary consolidation occur completely and minimize secondary consolidation effects, a continuous time-deflection plot (semi-logarithmic) was kept for each load increment and three methods were used to determine the end of primary settlement: (i) Casagrande's logarithm of time fitting method (Casagrande, 1936); (ii) Taylor's square root of time fitting method (Taylor, 1948); (iii) Rectangular hyperbola fitting method (Sridharan and Sreepada Rao, 1981).

(3) At the end of the test, oven-dried specimens were cracked open to establish the presence of pebbles. The results for specimens that contained pebbles exceeding 15 mm in diameter were discarded.

3.4.5 Results

Fig 3.5 shows the lateral distribution of yield stresses for undisturbed Battleford till samples taken from four different depths (16 m, 24 m, 32 m and 48 m). These yield stress values were determined using the ln(1+e)-log p' approach proposed by Onitsuka et al. (1995). Because of its general acceptance in geotechnical practice, yield stress values were also obtained using Casagrande's method (Casagrande, 1936). Table 3.2 gives a summary of yield stress values. The anisotropy state of the yield stresses was interpreted using a generalized anisotropy analysis procedure that involves plotting of a Mohr's stress circle based on 3 values of normal stresses measured along 3 arbitrary radial directions in a horizontal plane. The larger the difference in 3 normal stresses, the larger will be the diameter of the Mohr's stress circle. An increase in the diameter of the Mohr's stress circle represents an increase in the extent of anisotropy in the horizontal plane. The details of the generalized anisotropy analysis procedure are given in Appendix A. It must be emphasized that:

(1) The yield stresses determined with several samples laterally trimmed from the same tube are assumed to represent the yield stresses in different directions for one unique soil element. This can be considered as reasonable since the

samples are continuously acquired with intervals of 10 to 15 cm at approximately the same depth.

(2) The anisotropy analysis procedure proposed in this thesis is based on the analysis of Mohr's circle. Therefore, an implicit assumption is adopted here that the potential reason for the existence of this anisotropy state is due to a unique past stress state. This may or may not be true.

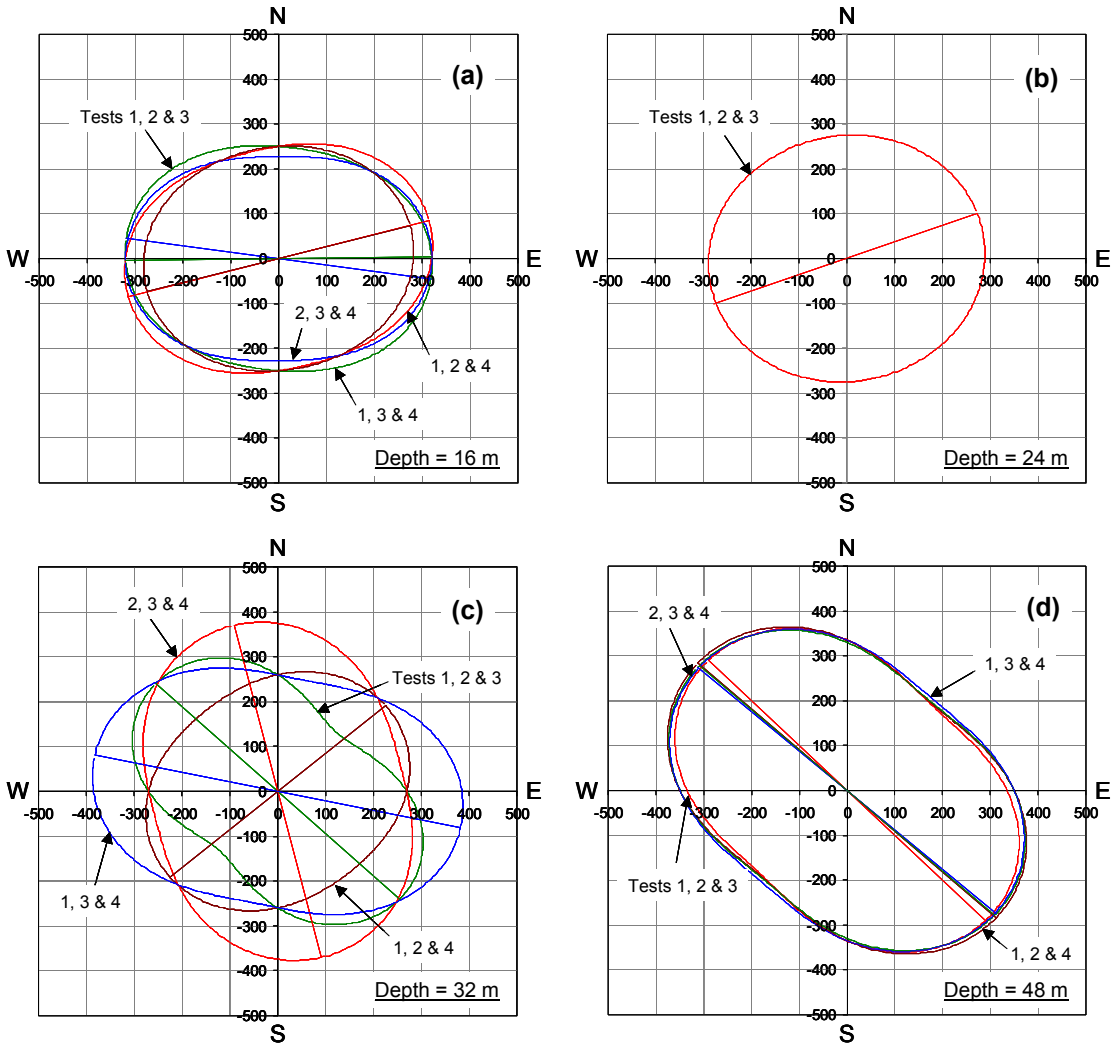

Fig 3.5 Lateral distribution of yield stresses for undisturbed Battleford till samples (a) Depth = 16 m; (b) Depth = 24 m; (c) Depth = 32 m; (d) Depth = 48 m

Table 3.2 Summary of yield stress values for undisturbed Battleford till samples

Sample # 15; Depth = 16 m

Test #	1	2	3	4	5
Orientation	N-S	W-E	N45E-S45W	N30W-S30E	Vertical
Yield Stress (kPa; Casagrande's Method)	250	320	275	250	400
Yield Stress Ratio	0.63	0.80	0.69	0.63	1.00
Yield Stress (kPa; Onisuka's Method)	250	340	275	240	385
Yield Stress Ratio	0.65	0.88	0.71	0.62	1.00

Sample # 22; Depth = 24 m

Test #	1	2	3
Orientation	N-S	N60E-S60W	N60W-S60E
Yield Stress (kPa; Casagrande's Method)	275	290	280
Yield Stress Ratio	n/a	n/a	n/a
Yield Stress (kPa; Onisuka's Method)	260	300	270
Yield Stress Ratio	n/a	n/a	n/a

[Note: No test on vertically oriented samples.]

Sample # 29; Depth = 32 m

Test #	1	2	3	4	5
Orientation	N-S	W-E	N45W-S45E	N45E-S45W	Vertical
Yield Stress (kPa; Casagrande's Method)	260	270	350	295	360
Yield Stress Ratio	0.72	0.75	0.97	0.82	1.00
Yield Stress (kPa; Onisuka's Method)	260	280	340	300	350
Yield Stress Ratio	0.74	0.80	0.97	0.86	1.00

Sample # 42; Depth = 48 m

Test #	1	2	3	4	5
Orientation	N-S	N30E-S30W	N30W-S30E	W-E	Vertical
Yield Stress (kPa; Casagrande's Method)	335	270	400	350	390
Yield Stress Ratio	0.86	0.69	1.03	0.90	1.00
Yield Stress (kPa; Onisuka's Method)	335	280	400	350	390
Yield Stress Ratio	0.86	0.72	1.03	0.90	1.00

It can be seen from Fig 3.5 that the distribution of the lateral yield stresses does not follow a consistent trend with depth. However, samples taken from the same depth tend to show an approximately consistent orientation of the maximum yield stress. The only exception is the rather random orientation exhibited by samples taken from a depth of 32 m. It can also been seen from Fig 3.5 that the orientation of maximum yield stress changes from an approximately E-W direction at a depth of 16 m to a NW-SE direction at a depth of 48 m. Clearly, more tests are needed before any correlation between the maximum yield stress direction and the direction of glacial movement could be

established. However, the procedure adopted for the investigation of lateral anisotropy of yield stress appears to be promising.

3.5 Summary

A procedure based on standard oedometer test is adopted to investigate the dependence of maximum yield stress orientation for a given soil sample on its stress history. The procedure involves testing several oedometer samples trimmed in horizontal, vertical and inclined directions. The term yield stress is used in the interpretation of test results as it represents a stress level corresponding to the collapse of the structure of the soil. Five different methods of establishing yield stress values were used. It was found that the yield stress values obtained using these five methods were quite close to each other, implying that any one of the five methods can be used to establish the magnitude of yield stress. Results of tests conducted on kaolin samples prepared in the lab and subjected to a precise stress history suggest that yield stress exhibits certain orientation dependence that can be related to the stress history experienced by the soil. However, the effect of different boundary conditions during consolidation and oedometer testing was not investigated. Undisturbed samples of Battleford till taken from four different depths were also tested using the above-mentioned procedure. Samples taken from the same depth exhibit a consistent orientation of maximum yield stress in the horizontal plane. However, this orientation was observed to change with depth of sampling. Based on the limited number of tests done on Battleford till samples, the orientation dependence of yield stress cannot be confirmed. More tests are needed before any correlation between the maximum yield stress orientation and the direction of glacial movement could be established.

Chapter 4 Measurement of Stiffness Anisotropy

4.1 Introduction

The coefficient of earth pressure at rest (K_0) is defined as the ratio of the horizontal to vertical effective stress in soil resulting from the application of vertical load under a condition of zero lateral deformation. If the soil is assumed to be in elastic state, K_0 can be shown to be a function of Young's modulus (E) and Poisson's ratio (ν) of the soil. Therefore, it can be considered as representing the "stiffness" of the soil skeleton. For an isotropic soil, K_0 is given by:

$$K_0 = \frac{\nu}{1-\nu} \tag{4.1}$$

For a cross-anisotropic soil, K_0 is given by:

$$K_0 = \frac{E_v}{E_h}\left(\frac{\nu_{vh}}{1-\nu_{hh}}\right) \tag{4.2}$$

where E_v is the Young's modulus in the vertical direction; E_h is the Young's modulus in the horizontal direction; ν_{hh} is the Poisson's ratio in the horizontal plane and ν_{vh} is the Poisson's ratio in the vertical plane. Eq. (4.1) and Eq. (4.2) can be derived based on generalized Hooke's law (e.g. Timoshenko and Goodier, 1970).

It is possible to obtain elastic constants for a given soil from oedometer test results. For an isotropic soil, only one oedometer test conducted on a sample oriented in any direction is sufficient provided stresses and strains along two mutually orthogonal axes are measured (or controlled). For a cross-anisotropic soil, it is necessary to conduct a minimum of two oedometer tests: one along the axis of cross-anisotropy (usually vertical axis for most soils) and one along a direction inclined at an angle (not perpendicular) with respect to the axis of cross-anisotropy.

For a cross-anisotropic or an isotropic soil, K_0 at a given depth is the same irrespective of the radial direction. However, for a truly anisotrpic soil, K_0 value at a given depth changes with a change in the radial direction. In an oedometer test, if the horizontal normal stresses in all directions always have the same values, the Mohr's

circles in the horizontal plane will be a series of dots (radius = 0, no shear components occur). If the horizontal normal stresses in different directions are different, the Mohr's circles in the horizontal plane will have non-zero radii and shear stresses are present.

It should be noted that the above description based on Mohr's stress circle masks a fairly complex constitutive relationship. A constitutive relationship is a set of mathematical equations describing the stress-strain behaviour of a material. These equations usually express increments of strain in terms of stress increments, or vice versa. During the last few decades, significant progress has been made on the development of isotropic and cross-anisotropic constitutive models for soils. However, the constitutive laws of a truly anisotropic soil have not been well understood so far. For a specimen in an oedometer test, the test is stress-controlled in the vertical direction and strain-controlled in the horizontal (radial) direction. The case thus becomes more complicated. Herein, the constitutive theory will be excluded and the thesis will be limited in the most straightforward experimental studies, i.e. the Mohr's circle of horizontal stresses.

It is shown in Appendix A that a Mohr's circle can be resolved by measuring the radial reactions in any three directions in oedometer tests. Anisotropic ratio (e.g., Gareau et al., 2004) is defined as the ratio of the maximum normal stress (major principal stress on the Mohr's circle) to the minimum normal stress (minor principal stress on the Mohr's circle). From the following expression, this part of the experimental study can then be essentially interpreted as K_0-anisotropy, or "stiffness"-anisotropy.

$$\text{Anisotropic Ratio} = \frac{\sigma'_{h\max}}{\sigma'_{h\min}} = \frac{\sigma'_v K_{0\max}}{\sigma'_v K_{0\min}} = \frac{K_{0\max}}{K_{0\min}} \tag{4.3}$$

In the present study, eleven samples (two at TU Delft, nine at U of S) of Battleford till were successfully tested by a newly developed oedometer ring with lateral stress measurement capability (described later in this chapter). All these samples were vertically trimmed samples. In order to assess the performance of the new oedometer ring, kaolin samples with known stress history were also tested using this ring.

4.2 Development of Lateral Stress Oedometer used in the Present Study

4.2.1 Oedometer Ring with Machined Diaphragms

In Chapter 2, several designs of oedometer ring with lateral stress measurements (Brooker and Ireland, 1965; Dyvik et al., 1985; Senneset, 1989; Colmenares, 2001) were reviewed. From this review, it can be seen that none of these oedometer rings can be used to study lateral anisotropy. In fact, only the design proposed by Senneset (1989) can measure the values of lateral stresses in different directions, but in this case, the zero lateral strain condition is not satisfied. In order to perform this research, a specially designed oedometer ring (Gareau et al., 2004) was developed. Fig 4.1 shows the layout of this new oedometer ring. It was built from a single piece of stainless steel. The inside diameter of the ring is 50 mm (19.64 cm^2 specimen cross-sectional area). The ring accommodates a 30 mm high trimmed specimen (specimen H/D = 0.6). A high H/D ratio is necessary to ensure proper contact between the soil and the diaphragms.

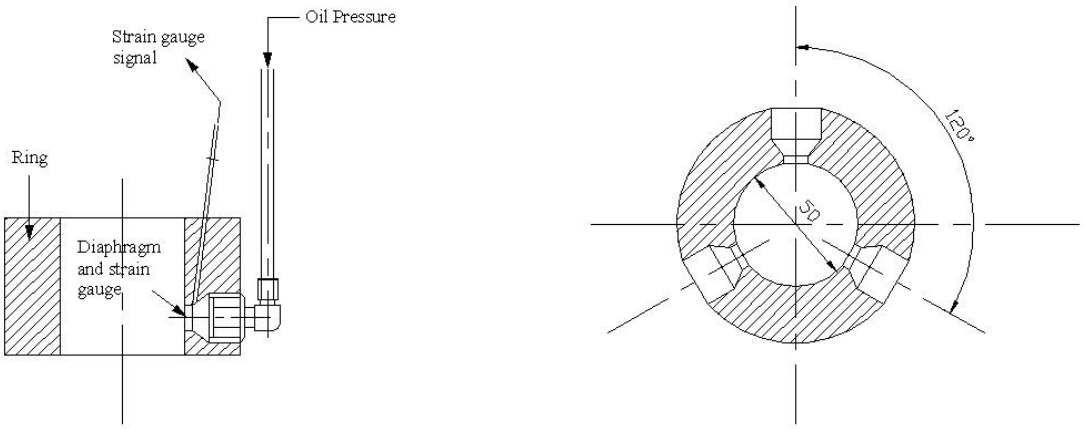

Fig 4.1 Lateral stress oedometer ring developed for this research (after Gareau et al., 2004). (a) Cross-sectional side view; (b) Cross-sectional top view.

Three independent 0.2 mm thick diaphragms were machined into the steel ring. These diaphragms were spaced at 120° angles around the periphery of the ring as shown in Fig 4.1. Four strain gauges (350 Ω resistance, full Wheatstone bridge) are glued on the outside surface (i.e. the surface that is not in contact with soil sample) of each diaphragm. The space behind each of the diaphragm is filled with silicone oil and is connected to a digital pressure-volume (P-V) controller (described in the next section). During a test,

the P-V controllers constantly adjust the pressures to maintain a "zero-reading" on the strain gauges. In this way, the hydraulic pressure against the diaphragm can be adjusted to offset the normal stress applied by the soil sample inside the testing ring. Therefore, the null lateral strain condition is obtained. The pump output pressure is considered to represent the radial stress at that point in the specimen.

4.2.2 Digital Pressure-Volume (P-V) Controllers

The digital P-V controllers used in the present study were manufactured by GDS Instruments Ltd, UK. Each P-V controller is able to apply, measure and log both the liquid pressure and volume change precisely. It can apply a maximum output pressure of 2000 kPa with a resolution of 1 kPa in "Normal Precision" mode. When controlled using a computer, the GDS digital P-V controller enables computer-automated test control and data logging via the standard IEEE-488 computer interface. The communication between the host computer and the hydraulic pumps is realized through a plug-n-play NI-488.2 GPIB (General Purpose Interface Bus) card manufactured by the National Instruments Inc, USA. The digital P-V controller uses an inert oil to apply the pressure at the back of a diaphragm. In the present study, Shell Tellus 22 oil was used. An inert oil is necessary because the extension wires of the strain gauges are directly immersed in the oil reservoir.

4.2.3 Data Acquisition System

A USB-based data acquisition module (PMD-1208LS manufactured by Measurement Computing Inc, USA) is used for acquiring output from the strain gauge bridges. This module is capable of logging up to 8 single-ended or up to 4 differential analog input signals. For the present study, all of the analog input channels were used in differential input mode. Three input channels were connected to each of the three strain gauge bridges and the fourth channel was used for the measurement of vertical deflection of the oedometer sample using a linear variable differential transformer (LVDT).

4.2.4 The Computerized Control System

The working principle of the control system is quite straightforward. As a vertical load is applied to the specimen (i.e. loading), an increment of total stress is partially transferred to the wall of the oedometer ring and thus to the thin wall diaphragms. In response to

this stress increment, the diaphragm tends to deflect outwards, resulting in an out-of-balance strain gauge bridge. The computer responds to this condition by instructing the P-V controllers to increase the oil pressure until the strain gauge bridge returns to its original null (balanced) position. As excess pore water pressure dissipates, the computer correspondingly instructs the P-V controllers to decrease the oil pressure. Thus, the strain gauge maintains zero deformation. Theoretically, the lateral stress will reach a steady value, and the stabilized oil pressure is the lateral stress for this applied vertical stress. Oil pressures for a typical loading/unloading step follow the pattern shown in Fig 4.2. The computer controls the P-V controllers using a standard IEEE 488 interface and a program written in Visual C++. The essential components of the control system are shown schematically in Fig 4.3 and pictorially in Fig 4.4.

The flow diagram of the control loop is illustrated in Fig 4.5. A two-coefficient control loop that is somewhat analogous to a typical PI control in electronic engineering is designed for this system. The "apparent" tolerance is zero in "raw data" of the strain gauges. Restrained by the transmission rate of the GPIB and/or the reaction time of the digital P-V controllers, the duration for one controlling loop (on all three controllers) is 8 seconds.

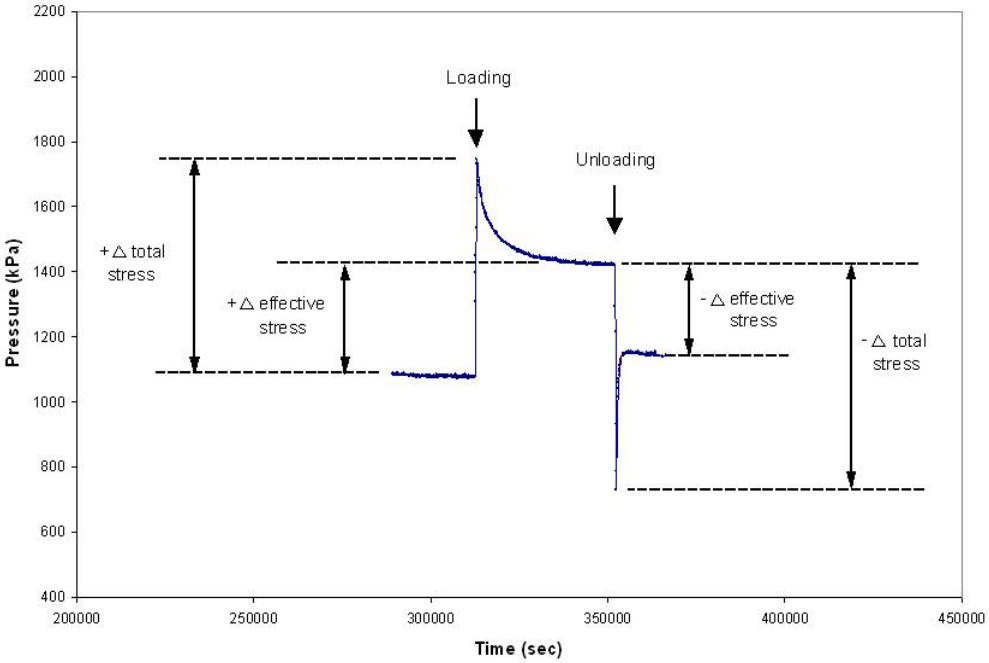

Fig 4.2 Typical measured pressures for a loading/unloading cycle.

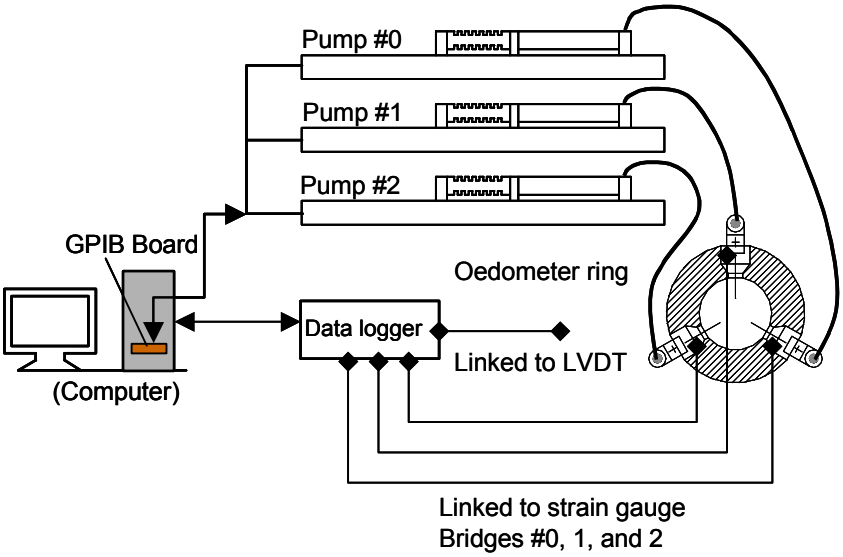

Fig 4.3 Schematic Diagram of the Control System for the U of S Lateral Stress Oedometer

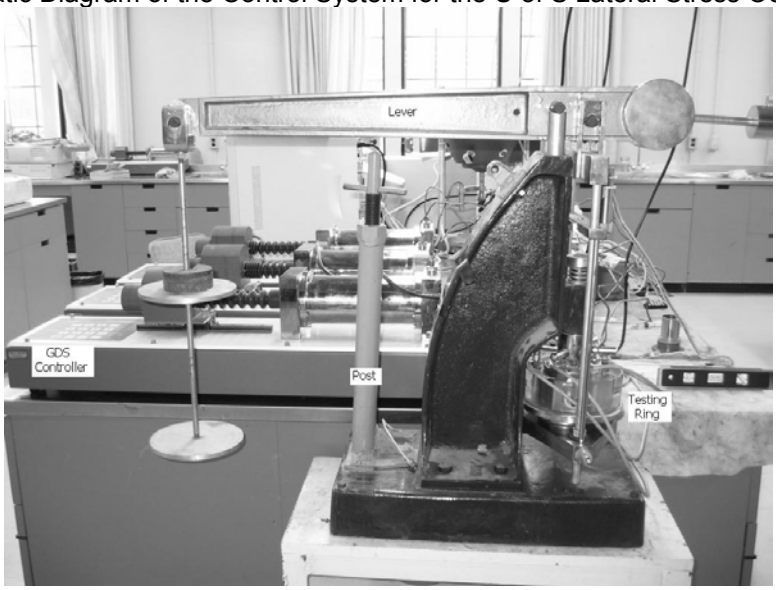

Fig 4.4 The U of S Lateral Stress Oedometer

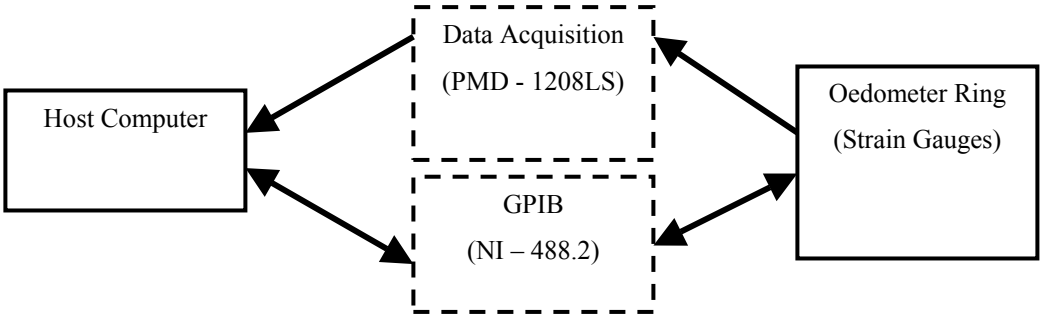

Fig 4.5 Flow Diagram for the Control Loop

4.3 Calibration and Corrections

4.3.1 GDS Digital P-V Controllers

Each GDS digital P-V controller is provided with a calibration certificate. The default setting of zero pressure is such that when the end of the flexible outlet is held level with the pressure outlet located at the end of the piston block, the controller reads zero pressure. However, of more interest is the difference of the measured pressures of all these pumps. Therefore, a special calibration procedure was performed as follows (see Fig 4.6 for the schematic diagram of the calibration set-up):

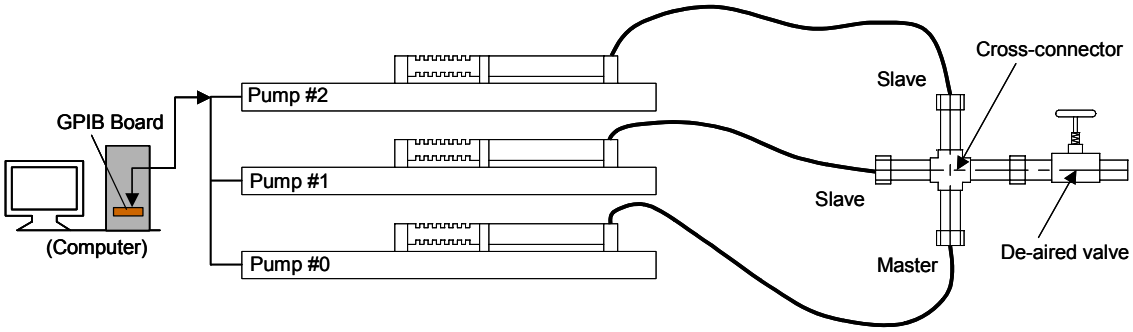

Fig 4.6 Schematic diagram of calibration set-up for the P-V controllers

(1) Using a cross connector, the pressure outlets of all three pumps were connected together (the last one was for a de-aired valve). The computer and all the pumps were also linked by interface bus cables.

(2) One pump was selected as the master controller. The other two were designated as slave controllers.

(3) The computer now took control of the master, setting various applied pressures and taking readings from all the controllers including the master.

(4) After loading and unloading over the full range has been carried out a correlation can be acquired for the correction of the output pressures in the formal testing.

The results of the calibration are shown in Fig 4.7. It can be seen from Fig 4.7 that the regression lines for the three P-V controllers were straight with R^2 value of 1. It was found that when P-V controller #0 (Pump#0 in Fig 4.6) read 0 kPa, P-V controllers #1 and #2 read 3 kPa and 6 kPa, respectively.

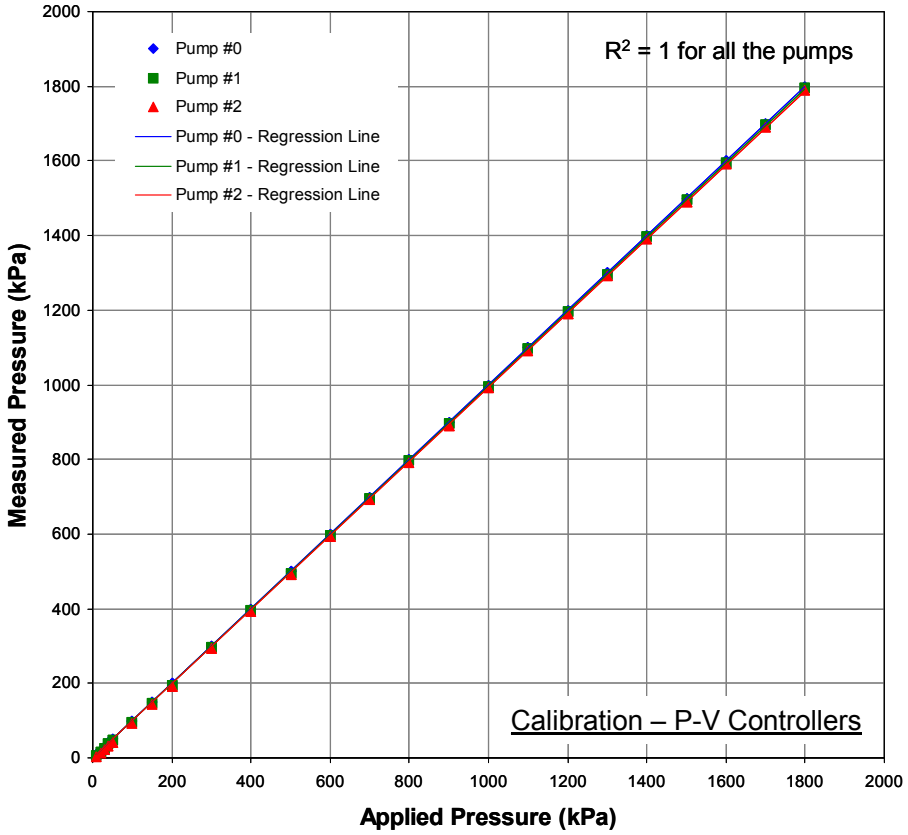

Fig 4.7 Results of Calibration for all the P-V controllers

4.3.2 Calibration of the Entire System

The lateral stress oedometer ring, strain gauges and the digital P-V controllers were calibrated together as a whole. Initially, a latex cylinder was used to simulate loading/unloading of a soil sample. Eventually, kaolin samples with known stress history were tested to verify the reliability of the apparatus.

The latex calibration involved inserting a latex cylinder of 50 mm diameter into the oedometer ring, applying vertical pressures and measuring the pump reactions. The latex used for calibration was assumed be linear elastic and isotropic with a Poisson's ratio close to 0.5. Thus, it was expected that the pump reaction would equal the applied vertical pressure exactly. Three loading and unloading cycles were carried out. Fig 4.8 shows a plot of applied vertical pressure versus pump reaction for these three cycles.

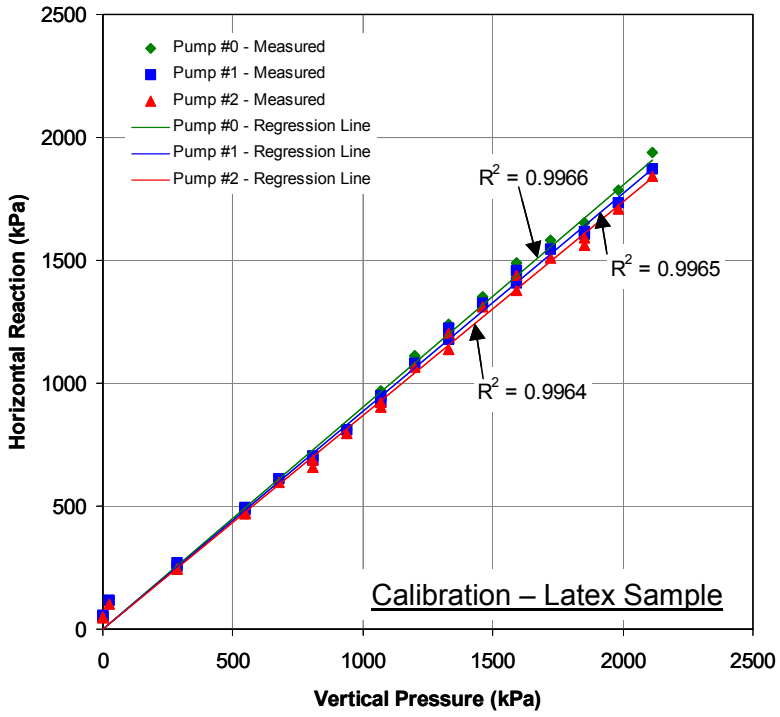

Fig 4.8 Results of the calibration of the entire system using latex sample

The data for each pump fall onto a straight line, with a high degree of statistical significance (R^2 values higher than 0.99). However, it was found that at low pressures, there were significant variations between the applied vertical pressure and the measured pump pressures. This is mainly due to the extent of the contact between the latex sample and the diaphragms. In instances where the latex sample was resting against the diaphragm after installation and thus having deflected the diaphragm, the measured pump reaction would be higher than the vertical pressure since an extra pressure was required to counter the initial deflection of the strain gauge. In instances where there existed a gap between the latex sample and the diaphragm at the start of testing, the measured pump reaction is likely to be much lower than the applied pressure since part of the action was buffered. Therefore, the influence of initial pressures must be taken into account during the testing process. This will be discussed further in Section 4.3.3.

The objective of tests on kaolin samples that were produced with isotropic lateral stresses was to ascertain if they would exhibit cross-anisotropy, i.e. isotropy in the horizontal plane. Three samples of kaolin were tested. The summary of testing results is shown in Table 4.1.

Table 4.1 Summary of results – Calibration tests using cross-anisotropic kaolin samples

Test Code	Vertical Stress (kPa)	Corrected Reactions (kPa)			Normalized Reactions (%)			Average K_0	Maximum (kPa)	Minimum (kPa)	Centre (kPa)	Radius (kPa)	Anisotropic Ratio	NAR (%)
		P0	P1	P2	P0	P1	P2							
		N-S	N60W-S60E	N60E-S60W	N-S	N60W-S60E	N60E-S60W							
	Insert	50	50	50										
	100	70	65	60	108	100	92	0.65	70.8	59.2	65.0	5.8	1.19	9
	199	112	110	98	105	103	92	0.54	115.4	97.9	106.7	8.7	1.18	8
	419	258	255	248	102	101	98	0.61	259.6	247.7	253.7	5.9	1.05	2
Kaolin_1	823	520	517	510	101	100	99	0.63	521.6	509.7	515.7	5.9	1.02	1
	1647	1032	1032	1057	99	99	102	0.63	1057.0	1023.7	1040.3	16.7	1.03	2
	2465	1525	1512	1530	100	99	101	0.62	1533.1	1511.6	1522.3	10.7	1.01	1
	3194	1935	1910	1907	101	100	99	0.60	1935.1	1899.6	1917.3	17.8	1.02	1
	1647	1469	1434	1450	101	99	100	0.88	1471.2	1430.8	1451.0	20.2	1.03	1
	823	885	854	875	102	98	100	1.06	889.6	853.1	871.3	18.3	1.04	2
	419	512	503	505	101	99	100	1.21	512.1	501.2	506.7	5.5	1.02	1
	199	275	290	265	99	105	96	1.39	291.2	262.1	276.7	14.5	1.11	5
	Insert	50	50	50										
	100	50	47	42	108	101	91	0.47	51.0	41.7	46.3	4.7	1.22	10
	199	107	95	97	107	95	97	0.50	107.1	92.2	99.7	7.4	1.16	7
	419	229	210	223	104	95	101	0.53	231.9	209.5	220.7	11.2	1.11	5
Kaolin_2	823	457	417	443	104	95	101	0.53	462.4	415.6	439.0	23.4	1.11	5
	1647	917	860	885	103	97	100	0.54	920.3	854.3	887.3	33.0	1.08	4
	3084	1735	1650	1673	103	98	99	0.55	1736.8	1635.2	1686.0	50.8	1.06	3
	823	805	765	765	103	98	98	0.95	805.0	751.7	778.3	26.7	1.07	3
	274	336	302	330	104	94	102	1.18	343.6	301.7	322.7	21.0	1.14	6
	110	175	153	163	107	93	100	1.49	176.4	150.9	163.7	12.7	1.17	8
	Insert	50	50	50										
	100	60	60	45	109	109	82	0.55	65.0	45.0	55.0	10.0	1.44	18
	199	102	107	92	102	107	92	0.50	109.2	91.5	100.3	8.8	1.19	9
	419	248	244	223	104	102	94	0.57	253.8	222.8	238.3	15.5	1.14	7
Kaolin_3	823	476	465	445	103	101	96	0.56	480.1	443.9	462.0	18.1	1.08	4
	1647	965	943	928	102	100	98	0.57	966.8	923.8	945.3	21.5	1.05	2
	2465	1445	1432	1396	101	101	98	0.58	1453.6	1395.0	1424.3	29.3	1.04	2
	3194	1852	1844	1805	101	101	98	0.57	1862.7	1804.6	1833.7	29.0	1.03	2
	1647	1430	1443	1465	99	100	101	0.88	1466.4	1425.6	1446.0	20.4	1.03	1
	823	825	846	872	97	100	103	1.03	874.9	820.5	847.7	27.2	1.07	3
	419	488	514	530	96	101	104	1.22	535.1	486.2	510.7	24.5	1.10	5
	199	247	280	297	90	102	108	1.38	304.0	245.3	274.7	29.4	1.24	11

Herein, a new parameter called Normalized Anisotropic Radius (NAR) is introduced. NAR for a given test can be obtained as follows:

(1) At any stage of the test, the three horizontal reactions are added and the sum is divided by 3 to obtain the average horizontal reaction.

(2) This average horizontal stress is taken as 100% and the three horizontal reactions are normalized with respect to the average horizontal reaction. For example, if during a particular stage of a test, the horizontal reactions were 70, 65 and 60 kPa, the average horizontal reaction would be 65 kPa (considered 100%). Therefore, the normalized values of the three horizontal reactions would be 108%, 100% and 92%, respectively.

(3) Since the normalized horizontal reactions are dimensionless, a dimensionless Mohr's circle is drawn using the procedure described in Appendix A. The center of this Mohr's circle is at 100% and its radius is defined as the Normalized Anisotropic Radius (NAR). For the above example, the maximum horizontal reaction (major principal stress) would be 70.8 kPa (or 109%) and the minimum horizontal reaction would be 59.2 kPa (or 91%), giving an NAR value of 9%.

The higher the value of NAR, the greater the extent of anisotropy exhibited by a soil sample. It can be seen from Table 4.1 that the NAR for the three cross-anisotropic kaolin samples was quite small, indicating isotropy of stresses in the horizontal plane as expected. These results demonstrate that the performance of the entire system is quite satisfactory. Slightly higher values of NAR at the initial loading stages of a test may be attributed to minor alignment problems during the installation of the soil sample inside the oedometer.

4.3.3 Corrections

The calibration test on the linked digital P-V controllers resulted in a correlation (P_0=0, P_1=3, P_2=6 kPa) that can be used to correct the experimental results. This means that the pressure values of P-V controllers #1 and #2 will be corrected based on the pressure data of P-V controller #0. In this way, the deviations of the output from different pumps can be eliminated and the horizontal reactions on different orientations can be directly compared to each other.

The second necessary correction is for the insert pressures. This can be achieved using a specific procedure during the initial stages of a test. When a soil sample is pushed into the oedometer ring, the applied pressures of all three pumps are set at a low pressure value (say, 15 kPa). Obviously, different contact conditions will lead to different contact pressures. In order to minimize this influence, the applied pressures are increased to a higher value (say, 50 kPa) that ensures complete contacts on all the diaphragms. The stabilized reading of each strain gauge will be set as the "null" position of the corresponding strain gauge. This initial (higher) pressure value will be subtracted from subsequent measured pressures.

4.4 Testing Procedure

4.4.1 Specimen preparation

The field sampling procedure has already been described in Section 3.4.3. In the laboratory, the specimen preparation procedure was slightly different from the standard oedometer test. A thin metal ring, approximately the same diameter as the testing ring, was used to prepare the specimens. Specimens were acquired by carefully hand-trimming the parent sample into this preparation ring. The initial specimen data (e.g., mass, size etc.) were determined following the general procedure. Eventually, the specimen was pushed into the testing ring (See "Corrections" in Section 4.3.3). The testing ring containing the specimen together with the porous stones was then placed into the consolidation cell. In order to reduce the side friction, both the preparation ring and the testing ring were greased using Dow Corning® silicone grease. The orientation of the specimen sitting in the testing ring was such that the natural top was always facing upwards and the lateral reactions were marked in clockwise manner.

4.4.2 Loading and Unloading

A WF24000 rear loading consolidometer (Wykeham Farrance Engineering Limited, UK) with a lever ratio equal to 11:1 was used to apply vertical load to the specimen. After the consolidation cell was installed onto the loading device, the pump pressures were adjusted to the "initial pressure" (typically 50 kPa) and the stabilized strain deflections were recorded. The "null" positions can then be set according to the corresponding deflection values (see "Corrections" in Section 4.3.3). An initial vertical pressure was applied on the specimen. The specimen was then flooded with distilled water and allowed to swell freely overnight.

During the loading stage, the sample was loaded in such a way that the vertical pressure doubled after each increment (typically 100, 200, 400, 800, 1600, 2400 and 3200 kPa). The loading duration for each load increment was around 12 hours. As mentioned above, the "zero" lateral strain is obtained by adjusting the pressure applied by the P-V controller to balance the change of the horizontal stress and the duration for an "update" of the pressure is about 8 seconds. Obviously, when the vertical pressure increased, the strain gauges temporarily deviated from the "zero" position. In order to

prevent damage to the diaphragms of the oedometer ring due to an extremely significant non-equilibrium condition, a special loading procedure was developed for relatively large loading increments (e.g. ≥ 400 kPa). Firstly, the post under the load beam (Fig 4.4) was adjusted to just touch the beam. Secondly, increased weights were placed onto the hanger and the post rather than the specimen itself carried most of the loading increment. Finally, the post was gradually lowered down and the loading increment was gradually transferred from the post to the specimen. It should be noted that this loading procedure does not affect the deflection value of each loading step.

Once the specimen had finished consolidating under the maximum loading, the specimen was unloaded by pressure decrements in the reverse order (typically 3200, 1600, 800, 400, 200, 100 and 0 kPa). Based on the same consideration of preventing excessive deformation of the diaphragms of the oedometer ring, a special unloading procedure was developed for relatively large unloading decrements (also ≥ 400 kPa). Firstly, the post was adjusted so that it just touched the load beam. The post was then gradually raised so that the post carried part of the unloading decrement. Finally, the weights were removed from the hanger. Obviously, if the pressure carried by the post does not exceed the unloading decrement, this unloading procedure would not affect the rebounding values as well. After the specimen was completely unloaded, the testing ring was taken away from the container and the specimen was extruded out quickly and the end-of-test specimen data (e.g. water content) was obtained.

4.4.3 Data recording

During the testing process, a computer program written by the author specifically for the new oedometer, automatically recorded the data into an ASCII text file that can be imported into a spreadsheet for processing and plotting.

4.5 Results and Discussion

The procedure outlined below was followed for the interpretation of results:

(1) Because of using special loading/unloading procedures, vertical deflection-time analysis is not considered. The *e-log p′* data is analyzed following the same procedure as for standard oedometer test.

(2) A variation of measured pump pressures with time is plotted for each test. Fig 4.9 shows a typical pump pressures vs. time variation (Test Birsay_8a). Every step in the graph represents either a loading or an unloading as defined in Fig 4.2.

(3) Following the procedure described in Appendix A, three stabilized horizontal normal stresses for every loading/unloading step are resolved using Mohr's circle to determine the magnitude and the orientation of maximum and minimum horizontal stresses. The results are presented using an anisotropy diagram where the magnitude of horizontal stress in a certain orientation is directly proportional to the distance from the origin of the diagram. This results in an oblong (noncircular) spatial distribution of horizontal stress. Fig 4.10 shows typical anisotropy diagrams (Test Birsay_8a) for both the loading and the unloading steps. The more oblong the anisotropic diagram, the greater the extent of K_0-anisotropy. The major axis of the stress distribution indicates the spatial direction of maximum horizontal stress. Table 4.2 gives a summary of results for all the eleven tests done using undisturbed Battleford till samples.

(4) Evolution of K_0-anisotropy within a soil sample is established on the basis of the values of NAR measured during the various stages of the test.

(5) After analyzing all the anisotropy diagrams for all the tests, spatial distribution of K_0-anisotropy for all the tests on Battleford till is plotted. Interpretation of this distribution is discussed in detail in Section 4.5.1.

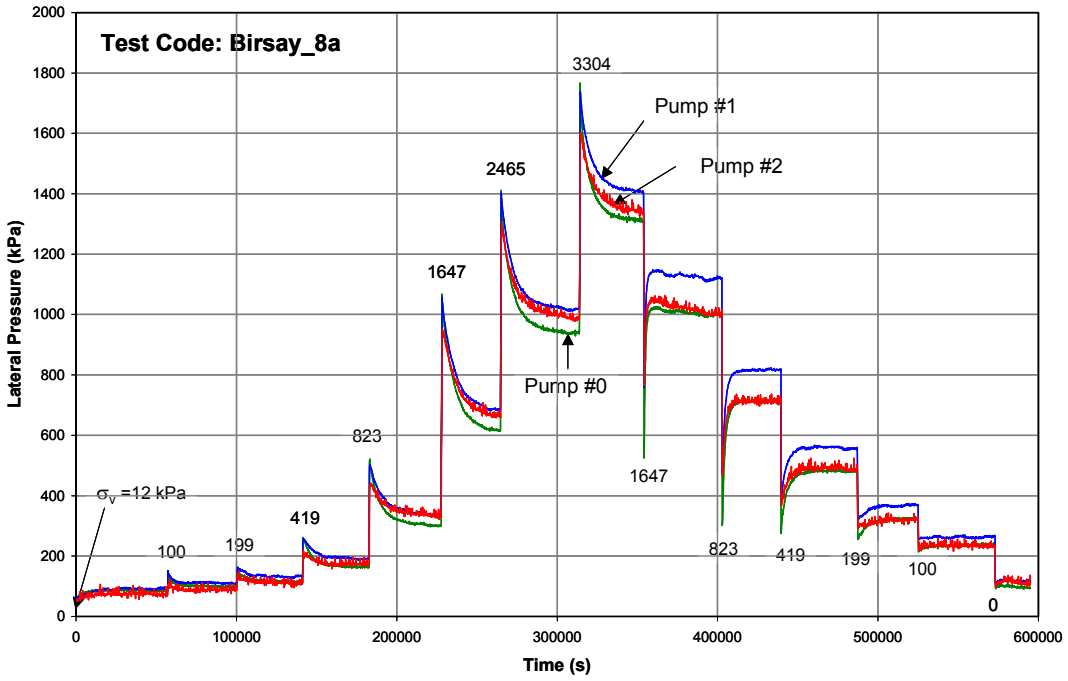

Fig 4.9 K_0 anisotropy – Typical results during various stages of loading and unloading

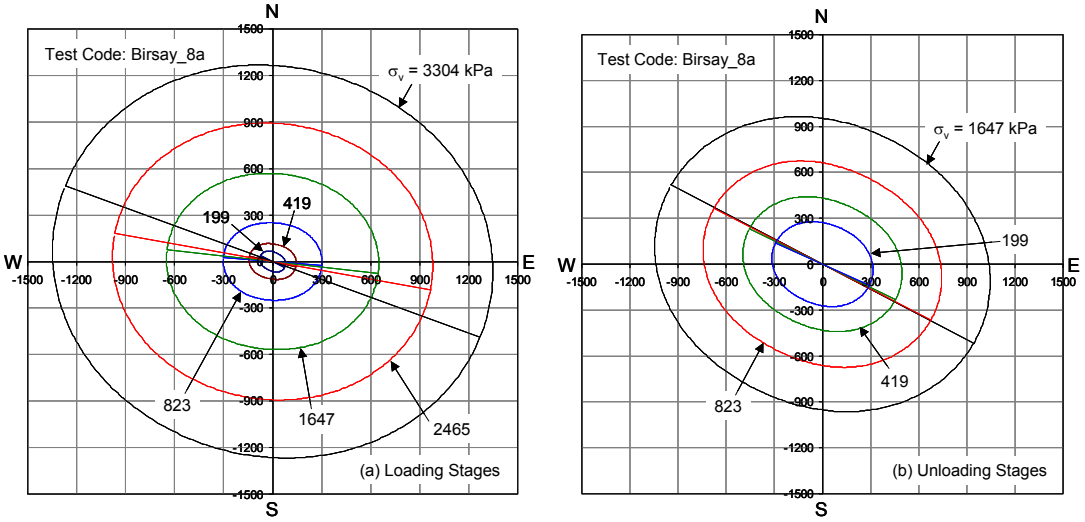

Fig 4.10 K_0 anisotropy – Distribution of horizontal stresses: (a) loading stages; (b) unloading stages

Table 4.2 K_0 anisotropy tests – Summary of results

Test Code	Depth (m)	Vertical Stress	Corrected Reactions (kPa) P0 (N-S)	P1 (N60W-S60E)	P2 (N60E-S60W)	Average K_0	Maximum (kPa)	Minimum (kPa)	Centre (kPa)	Radius (kPa)	Anisotropic Ratio	NAR (%)	Maximum Orientation
		12	35	46	31	3.01	46.3	28.4	37.3	9.0	1.63	24	142.5
		100	50	63	46	0.53	63.3	42.7	53.0	10.3	1.48	19	143.5
		199	65	83	66	0.36	83.0	59.7	71.3	11.7	1.39	16	151.4
		419	114	144	130	0.31	146.7	112.0	129.3	17.3	1.31	13	166.1
Birsay_8a	10	823	250	293	286	0.34	303.0	249.7	276.3	26.6	1.21	10	175.6
		1647	568	638	621	0.37	651.2	566.8	609.0	42.2	1.15	7	173.3
		2465	892	973	943	0.38	983.3	888.7	936.0	47.3	1.11	5	169.3
		3304	1265	1358	1294	0.40	1360.6	1250.7	1305.7	54.9	1.09	4	158.9
		1647	953	1075	959	0.60	1075.1	916.3	995.7	79.4	1.17	8	151.3
		823	662	768	668	0.85	768.1	630.6	699.3	68.7	1.22	10	151.4
		419	432	511	442	1.10	511.3	412.0	461.7	49.7	1.24	11	153.3
		199	272	323	281	1.47	323.4	260.6	292.0	31.4	1.24	11	154.8
		100	187	217	188	1.98	217.0	177.7	197.3	19.7	1.22	10	150.8
		Preconsolidation Pressure =			450 kPa								
		12	24	49	18	2.45	49.3	11.4	30.3	19.0	4.34	63	144.7
		100	47	62	51	0.54	62.3	44.4	53.3	9.0	1.40	17	157.5
		199	65	75	42	0.30	80.2	41.1	60.7	19.5	1.95	32	128.6
		419	124	133	103	0.29	137.8	102.2	120.0	17.8	1.35	15	128.5
Birsay_8b	10	823	270	277	262	0.33	278.3	261.0	269.7	8.7	1.07	3	133.9
		1647	609	615	616	0.37	617.7	609.0	613.3	4.4	1.01	1	3.8
		2465	944	924	958	0.38	961.7	922.3	942.0	19.7	1.04	2	47.9
		3304	1307	1263	1303	0.39	1319.1	1262.9	1291.0	28.1	1.04	2	62.4
		1647	970	988	996	0.60	1000.0	969.3	984.7	15.4	1.03	2	8.8
		823	680	700	716	0.85	719.5	677.8	698.7	20.8	1.06	3	13.2
		419	446	458	474	1.10	475.6	443.1	459.3	16.2	1.07	4	17.4
		199	280	288	304	1.46	304.8	276.6	290.7	14.1	1.10	5	20.5
		100	186	195	206	1.96	207.2	184.1	195.7	11.6	1.13	6	16.7
		Preconsolidation Pressure =			460 kPa								
		12	30	17	39	2.31	41.4	15.9	28.7	12.8	2.61	45	48.0
		100	50	35	61	0.49	63.7	33.6	48.7	15.1	1.90	31	47.6
		199	82	65	89	0.39	92.9	64.4	78.7	14.2	1.44	18	51.8
		419	165	148	201	0.41	202.6	140.1	171.3	31.2	1.45	18	39.2
		769	353	344	386	0.47	386.5	335.5	361.0	25.5	1.15	7	35.9
		1647	767	763	761	0.46	767.2	760.1	763.7	3.5	1.01	0	99.6
Birsay_11a	12	2465	1180	1173	1131	0.47	1191.9	1130.7	1161.3	30.6	1.05	3	116.2
		3304	1595	1571	1481	0.47	1618.4	1479.6	1549.0	69.4	1.09	4	114.2
		1647	1170	1194	1136	0.71	1200.3	1133.0	1166.7	33.7	1.06	3	132.2
		769	820	828	793	1.06	834.8	792.5	813.7	21.2	1.05	3	126.3
		419	510	518	526	1.24	527.2	508.8	518.0	9.2	1.04	2	15.0
		199	305	299	341	1.58	341.2	288.8	315.0	26.2	1.18	8	33.8
		100	196	196	231	2.09	231.0	184.3	207.7	23.3	1.25	11	30
		Preconsolidation Pressure =			450 kPa								
		12	18	55	36	2.93	57.7	15.0	36.3	21.4	3.85	59	164.6
		100	25	81	48	0.52	83.8	18.8	51.3	32.5	4.45	63	162.1
		199	35	103	59	0.33	105.5	25.9	65.7	39.8	4.08	61	160.2
		419	65	178	128	0.30	189.1	58.3	123.7	65.4	3.24	53	166.9
Birsay_11b	12	769	194	353	308	0.37	379.6	190.4	285.0	94.6	1.99	33	172.0
		1647	464	719	706	0.38	795.5	463.8	629.7	165.8	1.72	26	178.7
		2465	800	1108	1131	0.41	1226.4	799.6	1013.0	213.4	1.53	21	1.8
		3304	1130	1468	1506	0.41	1607.0	1129.0	1368.0	239.0	1.42	17	2.7
		1647	860	1163	1191	0.65	1283.3	859.4	1071.3	212.0	1.49	20	2.2
		769	595	823	836	0.98	907.9	594.8	751.3	156.5	1.53	21	1.4
		419	390	543	554	1.18	601.5	389.8	495.7	105.9	1.54	21	1.7
		199	260	348	341	1.59	372.8	259.9	316.3	56.5	1.43	19	177.9
		100	188	243	231	2.22	254.1	187.3	220.7	33.4	1.36	15	174
		Preconsolidation Pressure =			440 kPa								

Continued…

(continuation of Table 4.2)

Test Code	Depth (m)	Vertical Stress	Corrected Reactions (kPa) P0 N-S	P1 N60W-S60E	P2 N60E-S60W	Average K_0	Maximum (kPa)	Minimum (kPa)	Centre (kPa)	Radius (kPa)	Anisotropic Ratio	NAR (%)	Maximum Orientation
		12	20	25	12	1.53	26.6	11.4	19.0	7.6	2.32	40	131.2
		100	50	43	61	0.52	61.8	40.9	51.3	10.5	1.51	20	41.4
		199	75	78	95	0.42	95.1	70.2	82.7	12.5	1.35	15	26.0
		401	130	140	174	0.37	174.6	121.4	148.0	26.6	1.44	18	23.8
Birsay_25b	28	773	275	273	348	0.39	348.0	249.3	298.7	49.4	1.40	17	30.7
		1647	648	621	779	0.41	780.2	585.1	682.7	97.6	1.33	14	34.6
		2454	1009	924	1170	0.42	1178.6	890.1	1034.3	144.3	1.32	14	40.0
		3209	1301	1175	1486	0.41	1501.3	1140.0	1320.6	180.6	1.32	14	41.9
		1647	975	938	1126	0.62	1128.0	898.0	1013.0	115.0	1.26	11	35.4
		773	660	623	709	0.86	713.8	614.2	664.0	49.8	1.16	8	42.7
		401	432	399	446	1.06	453.5	397.8	425.7	27.9	1.14	7	51.6
		199	268	236	266	1.29	277.4	236.0	256.7	20.7	1.18	8	61.6
		100	165	148	164	1.60	170.0	148.0	159.0	11.0	1.15	7	61.5
		Preconsolidation Pressure =			480 kPa								
		12	32	39	31	2.74	39.0	29.0	34.0	5.0	1.35	15	146.7
		100	52	48	51	0.51	52.7	47.9	50.3	2.4	1.10	5	67.0
		199	83	63	73	0.37	84.5	61.5	73.0	11.5	1.38	16	75.0
		401	158	120	151	0.36	166.3	119.6	143.0	23.3	1.39	16	65.0
		773	300	233	304	0.36	325.0	232.9	279.0	46.1	1.40	17	58.6
		1647	670	533	676	0.38	719.7	532.9	626.3	93.4	1.35	15	58.9
Birsay_25c	28	2454	1030	803	1012	0.39	1094.0	802.6	948.3	145.7	1.36	15	62.1
		3209	1370	1081	1336	0.39	1444.7	1079.9	1262.3	182.4	1.34	14	63.1
		1647	1080	890	1066	0.61	1134.2	889.7	1012.0	122.2	1.27	12	61.9
		773	710	628	731	0.89	752.5	626.8	689.7	62.8	1.20	9	54.4
		401	458	428	504	1.16	507.5	419.1	463.3	44.2	1.21	10	41.5
		199	290	283	336	1.52	336.2	269.7	303.0	33.2	1.25	11	33.5
		100	183	198	232	2.05	233.3	175.3	204.3	29.0	1.33	14	21.3
		Preconsolidation Pressure =			480 kPa								
		12	22	38	34	2.53	40.9	21.7	31.3	9.6	1.89	31	173.1
		100	28	41	54	0.41	56.0	26.0	41.0	15.0	2.16	37	15.0
		199	48	53	84	0.31	84.2	39.1	61.7	22.5	2.15	37	26.3
		419	115	105	166	0.31	166.4	90.9	128.7	37.8	1.83	29	34.4
Birsay_25d	28	748	258	223	324	0.36	327.5	209.1	268.3	59.2	1.57	22	40.0
		1647	600	513	666	0.36	681.6	504.4	593.0	88.6	1.35	15	47.3
		3304	1326	1153	1324	0.38	1382.3	1153.0	1267.6	114.7	1.20	9	60.3
		1647	1048	933	1061	0.62	1095.3	932.7	1014.0	81.3	1.17	8	57.4
		748	714	652	700	0.92	726.2	651.1	688.7	37.5	1.12	5	66.2
		419	495	468	456	1.13	496.1	449.9	473.0	23.1	1.10	5	98.7
		199	338	338	286	1.61	355.3	286.0	320.7	34.7	1.24	11	120.0
		100	220	230	183	2.12	239.6	182.4	211.0	28.6	1.31	14	125.8
		Preconsolidation Pressure =			450 kPa								
		100	24	8	5	0.12	24.1	0.5	12.3	11.8	44.95	96	94.2
		200	75	32	32	0.23	75.0	17.7	46.3	28.7	4.25	62	90.0
		400	175	85	120	0.32	179.0	74.3	126.7	52.4	2.41	41	78.7
		800	400	240	295	0.39	405.5	217.8	311.7	93.9	1.86	30	80.1
Birsay_36a	36	1600	815	585	675	0.43	825.5	557.8	691.6	133.8	1.48	19	78.6
		2000	1010	750	870	0.44	1026.9	726.4	876.6	150.2	1.41	17	76.3
		1600	930	600	740	0.47	947.9	565.4	756.6	191.2	1.68	25	77.5
		1200	850	515	650	0.56	866.3	477.0	671.6	194.6	1.82	29	78.2
												Note: Tested at TUDelft	

Continued…

(continuation of Table 4.2)

Test Code	Depth (m)	Vertical Stress	Corrected Reactions (kPa) P0 N-S	P1 N60W-S60E	P2 N60E-S60W	Average K_0	Maximum (kPa)	Minimum (kPa)	Centre (kPa)	Radius (kPa)	Anisotropic Ratio	NAR (%)	Maximum Orientation
		100	16	11	15	0.14	17.5	10.6	14.0	3.5	1.65	25	67.0
		200	49	51	47	0.24	51.1	46.5	48.8	2.3	1.10	5	130.3
		400	137	153	120	0.34	155.5	117.3	136.4	19.1	1.33	14	134.6
		800	329	337	279	0.39	351.6	278.7	315.2	36.4	1.26	12	123.9
		1600	747	724	627	0.44	773.0	625.6	699.3	73.7	1.24	11	114.7
		2000	942	915	779	0.44	979.5	777.9	878.7	100.8	1.26	11	115.5
Birsay_36b	36	1600	814	790	695	0.48	838.8	694.2	766.5	72.3	1.21	9	114.6
		800	604	610	515	0.72	637.9	514.9	576.4	61.5	1.24	11	121.6
		400	399	419	361	0.98	427.2	358.9	393.1	34.2	1.19	9	130.0
		100	169	155	156	1.60	169.5	150.4	159.9	9.6	1.13	6	87.8
												Note: Tested at TUDelft	
		12	17	20	34	1.91	34.1	13.2	23.7	10.5	2.59	44	25.3
		100	23	33	38	0.31	40.2	22.5	31.3	8.8	1.78	28	9.6
		199	48	62	64	0.29	68.1	47.9	58.0	10.1	1.42	17	3.3
		419	124	157	141	0.34	159.7	121.6	140.7	19.1	1.31	14	165.5
Birsay_40a	40	769	273	321	289	0.38	322.6	266.1	294.3	28.2	1.21	10	159.6
		1647	652	720	672	0.41	721.7	641.0	681.3	40.3	1.13	6	158.3
		2465	994	1073	1016	0.42	1074.7	980.6	1027.7	47.1	1.10	5	157.9
		3249	1342	1430	1371	0.43	1432.8	1329.2	1381.0	51.8	1.08	4	159.4
		1647	1035	1083	1076	0.65	1094.6	1034.7	1064.7	29.9	1.06	3	176.1
		769	718	708	736	0.94	737.0	704.3	720.7	16.4	1.05	2	40.3
		419	505	463	511	1.18	523.2	462.8	493.0	30.2	1.13	6	56.7
		199	330	273	316	1.54	340.6	272.0	306.3	34.3	1.25	11	66.8
		100	226	176	206	2.04	231.7	173.6	202.7	29.1	1.33	14	71.7
		Preconsolidation Pressure =			450 kPa								
		12	15	38	31	2.26	41.6	14.4	28.0	13.6	2.89	49	171.4
		100	18	41	44	0.34	50.8	17.9	34.3	16.4	2.83	48	3.0
		199	30	63	56	0.25	69.7	29.6	49.7	20.1	2.36	40	174.2
		419	95	138	139	0.30	153.0	95.0	124.0	29.0	1.61	23	0.6
Birsay_40b	40	823	245	293	306	0.34	318.4	244.2	281.3	37.1	1.30	13	5.9
		1647	570	598	639	0.37	642.4	562.3	602.3	40.1	1.14	7	18.1
		2465	905	937	981	0.38	985.1	896.9	941.0	44.1	1.10	5	17.6
		3304	1265	1285	1342	0.39	1343.5	1251.2	1297.3	46.1	1.07	4	22.8
		1647	962	1009	1064	0.61	1070.6	952.7	1011.7	59.0	1.12	6	16.3
		823	715	738	738	0.89	745.7	715.0	730.3	15.3	1.04	2	0.0
		419	505	503	496	1.20	506.8	495.9	501.3	5.5	1.02	1	113.9
		199	330	323	326	1.64	330.4	322.3	326.3	4.1	1.03	1	77.4
		100	230	221	230	2.28	233.0	221.0	227.0	6.0	1.05	3	60
		Preconsolidation Pressure =			470 kPa								

4.5.1 K_0 - (horizontal "stiffness") Anisotropy and its Analysis

An analysis illustrated by spatial distribution plots will be used for the interpretation of K_0-anisotropy because of the following reasons:

(i) Idealized isotropy, or even cross-anisotropy does not exist for natural soils. Natural soils, more or less, exhibit characteristics of anisotropy.

(ii) Influence of localization extensively occurs during the formation of natural soils, especially for glaciated soils. Even for the samples from the same borehole, this may take place at different depths.

(iii) Compared with other properties, "stiffness" anisotropy is much more sensitive and easily disturbed during the field-sampling and specimen-preparing process.

(iv) The "disturbance" emanating from the intrinsic heterogeneity of the sample itself can hardly be avoided. Tomographic scanning of Battleford till

samples using a medical CT scanner showed that pebbles and gravels are fairly common in these samples. This may influence the test results considerably.

(v) A limitation of the testing system is that only three horizontal reactions can be measured on the wall of the oedometer ring. On the basis of the general analytical procedure described in Appendix A, it is possible to detect "apparent" anisotropy if one of the three load cells gives erroneous reading, e.g. due to the presence of a pebble in its close vicinity.

Therefore, it is likely that the results of individual tests will exhibit a tendency of divergence and should be assessed on the basis of results obtained using a large number of samples. A spatial distribution plot is designed for this purpose. The origin of this plot represents an anisotropy ratio of 1. Concentric circles labeled 10%, 20% and 30% represent anisotropic ratios of 1.1, 1.2 and 1.3, respectively. According to the magnitude of the anisotropic ratio and the orientation of the maximum horizontal stress, each load step becomes a pair of mirror-points on the spatial distribution plot. Fig 4.11 shows such spatial distribution plots for all the samples of Battleford till tested under the present study. Anisotropic ratios during the loading as well as the unloading are considered. It can be seen from Fig 4.11 that there is a fair degree of scatter in the spatial distribution of anisotropic ratio. However, a significant number of points plot in the N-E and S-W quadrants, indicating that axis representing maximum horizontal stiffness (shown by bold arrows in Fig 4.11) is along the NE-SW direction. This axis appears to coincide with the known glacial advance and retreat direction (Schreiner, 1990). However, more tests are needed on other glaciated soils representing other formations (e.g. Warman, Inter-till Clays) in order to establish a definite correlation between K_0-anisotropy and known glacial advance and retreat directions.

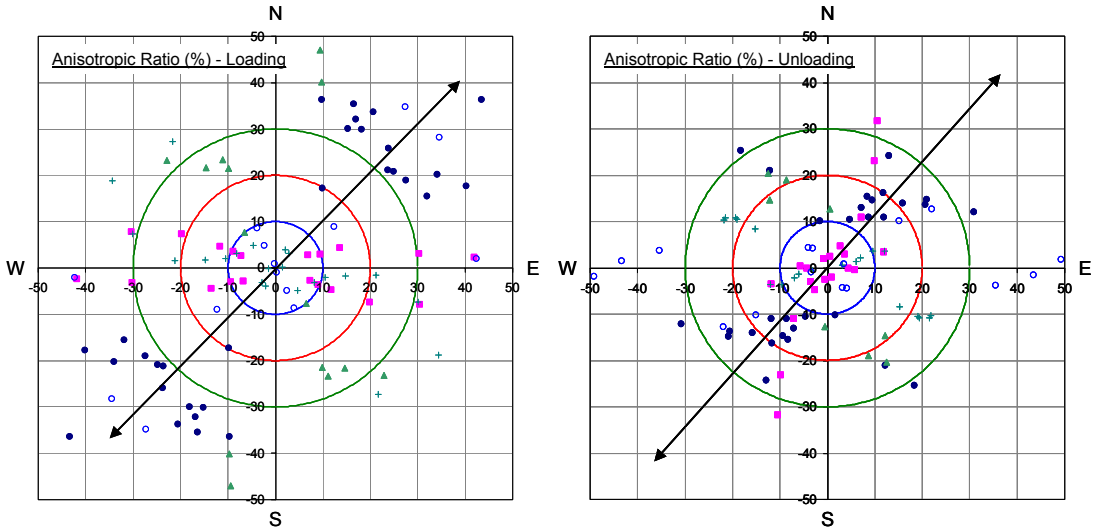

Fig 4.11 K_0 anisotropy – Distribution of anisotropic ratio in the horizontal plane

4.5.2 Evolution of K_0-anisotropy during an Oedometer Test

In order to investigate the evolution of the anisotropic horizontal stresses, the source and its relation with the past glaciation are excluded and only the anisotropic response itself is considered. From the data of Normalized Anisotropic Radius (NAR) shown in Table 4.2, it is observed that:

(i) During the first few loading steps (before reaching the preconsolidation pressure), NAR tends to be fairly large. This stage corresponds to the recompression line in a typical *e-log p'* curve.

(ii) After reaching the preconsolidation pressure, NAR approaches towards zero as the vertical pressure increases. This stage corresponds to the virgin compression line in a typical *e-log p'* curve.

(iii) During unloading, NAR tends to increase as the vertical pressure reduces. This stage corresponds the rebound line in a typical *e-log p'* curve.

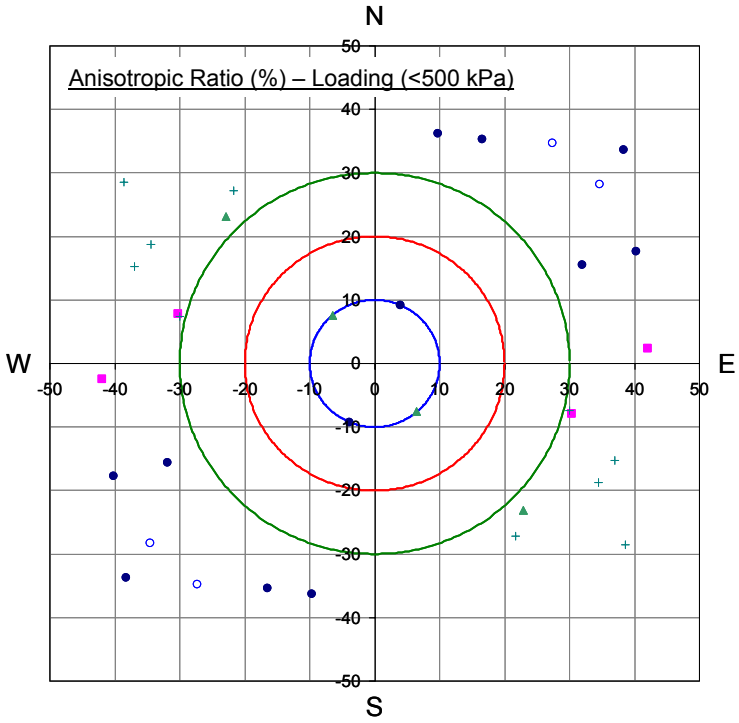

Fig 4.12 Distribution of anisotropic ratio in the horizontal plane for vertical stresses less than 500 kPa

Fig 4.12 showing spatial distribution of anisotropic ratios for vertical stresses less than 500 kPa confirms this observation. It can be seen from Fig 4.12 that for almost all the tests done on Battleford till, anisotropic ratios greater than 1.3 were recorded at vertical stresses less than the preconsolidation pressure (approximately 500 kPa). This observation can be explained on the basis of the so-called "force chains" theory. Experiments with particles in static and slowly shearing packs indicate that stresses are concentrated along "force chains" which coalesce and form complex networks that include many particles (e.g. Drescher and de Jong, 1972; Liu et al., 1995; Howell et al., 1999). Iverson and Iverson (2000) demonstrated the existence of these chains in simulated and natural tills by ring shear experiments. Therefore, the lateral reactions in oedometer tests can be treated as part of the resistance communicated through the force chains. When subjected to external actions, these chains reorganize continuously. Under an increasing overburden pressure, these internal networks are compacted with the skeleton, the lateral reactions tend to converge and the intrinsic properties of soil are dominant; as the overburden pressure decreases, these internal networks are rebounded

with the skeleton, the lateral reactions tend to diverge and random reorganization of the force chains is the dominant factor. In fact, this explanation is consistent with the concept of Intrinsic Consolidation Line (ICL) proposed by Burland (1990). Based on the assessment above, it can be expected that the lateral anisotropic properties would tend to fade under an increasing overburden pressure. Therefore, K_0-anisotropy must be measured before reaching the preconsolidation pressure. Unfortunately, the measurement of horizontal stresses during the initial stages of an oedometer test suffers from unwanted effects due to imperfect insertion of the sample into the oedometer ring. Clearly, there is a need to improve and optimize the sample insertion procedure before further testing on other glaciated soils is undertaken.

4.6 Summary

Although the constitutive relations for a truly anisotropic soil have not been well understood, a straightforward approach for the determination of anisotropy is to measure the horizontal reactions in at least three different directions during an oedometer test. Such an anisotropy can be simply interpreted as K_0-anisotropy. A specially designed oedometer ring has been developed for this research. Three horizontal normal stresses can be measured through three independent diaphragms machined into the ring wall at 120 degrees radial spacing. Its performance has been demonstrated by the test results on remolded and natural samples. The relationship between the applied vertical stress and the measured average lateral normal stress obtained by this ring shows good agreement with the published experimental results. Statistical analysis of results from tests done on Battleford till samples indicates that there may exist a correlation between the direction of maximum horizontal stiffness and the known direction of glacial advance and retreat. However, the results show some scatter and more tests are needed on other glaciated soils in order to confirm this correlation. A new parameter called normalized anisotropic radius (NAR) has been introduced in this thesis. Based on the analyses of NAR during the various stages of an oedometer test, it can be concluded that the measurement of K_0-anisotropy should be done at vertical stresses less than the preconsolidation pressure for a given soil. At vertical stresses higher than the preconsolidation pressure, the inherent anisotropy of a soil sample is generally destroyed.

Chapter 5 Measurement of In situ Stress Anisotropy

5.1 Introduction

This chapter describes the procedure and the results of in situ stress measurements carried out in Pot clay from Marum in the Netherlands using the self-boring Load Cell Pressuremeter (LCPM). As a part of the on-going collaborative research program between Technical University Delft and the University of Saskatchewan, the author spent three months (March to May 2004) at Technical University Delft. During his stay, he was involved with the planning, execution and data analysis of these LCPM tests. It would have been ideal to conduct such in situ stress measurements in Battleford till at Birsay, Saskatchewan. However, the unsuitability of the LCPM to tills and the high cost of renting the LCPM for use in Canada ruled out this possibility. Hence, it was decided to try and measure in situ stresses in Pot clay.

5.2 Pot Clay

During the Quaternary period, the continental ice sheet reached the Netherlands at least twice: during the Elsterian and the Saalian glaciations. The Peelo Clay (locally called Pot clay), on which the LCPM tests were performed, was deposited in the valleys during the retreat of the Elsterian ice sheet. The Saalian glaciers, characterized by two different directions of ice movements, subsequently overran the Pot clay. During the first ice advance the direction of the movement was from the NE to the SW and later the ice sheet moved towards the SE (Schokking, 1998).

When comparing Battleford till with Pot clay, it should be noted that these two soils belong to two different categories based on a general classification system for the subglacially-deformed materials. In terms of the latest glaciation, the former is classified as “till” that has never been overrun by ice sheets; the latter is classified as “glacetectonite” and has been overrun by ice sheets (see Chapter 2). However, both have been subglacially sheared during the glacial advance. This has been well accepted and broadly demonstrated in glaciological studies.

5.3 The Load Cell Pressuremeter (LCPM)

Generally there are two different Cambridge Self-Boring Pressuremeters (SBP) or Camkometers: the Expansion Pressuremeter and the Load Cell Pressuremeter (LCPM). The expansion pressuremeter is an active device, expanding a cavity out into the soil surrounding the instrument and measuring the pressures required to produce a given change in radius. The LCPM is a passive device, sitting at the correct location and measuring the pressures on the outside of the instrument through the so-called pressure balance principle. Fig 5.1 shows the Load Cell Pressuremeter probe along with its control box. The horizontal in situ stresses, both total and effective, can be simultaneously measured at six points (i.e. arms & clusters) equally spaced around the circumference of the probe. It does not impose expansion or loading on the soil.

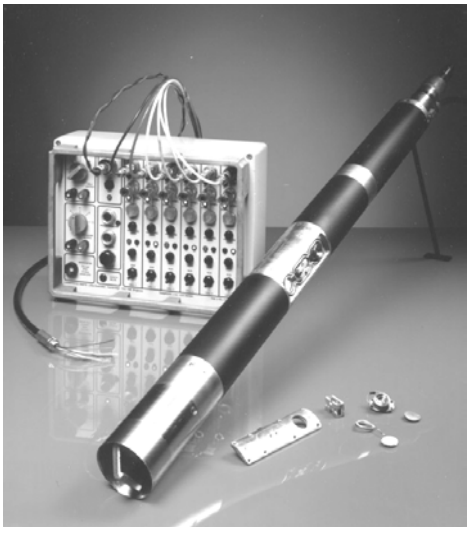

Fig 5.1 Load Cell Pressuremeter (photo courtesy of Cambridge Insitu)

The SBP test is quite unlike any other test. A specially designed and patented self-boring head allows the instrument to enter into the ground with an exceptionally small amount of disturbance to the soil. Apart from a very thin layer of sheared soil in direct contact with the instrument (estimated to be, in clays, not thicker than thirty microns), the original state of all the soil outside the instrument is maintained both as to position and to the state of in situ stress. The self-boring process works as follows (Fig 5.2). A cutter at the foot of the instrument rotates inside an internally tapered shoe. As the instrument is pressed steadily against the bottom of the hole, a plug of soil is extruded into the taper

as if it were a conical extrusion die. The top of this plug of soil is sliced off by the cutter positioned inside the shoe such that the pressure needed to drive the soil up the taper is made equal to the in situ vertical stress. The soil cuttings are carried away up the inside of the instrument by a flow of flushing fluid (usually water) supplied from the surface. This fluid flows, in all but the most permeable soils, in a closed circuit and does not affect the properties of the soil outside the instrument.

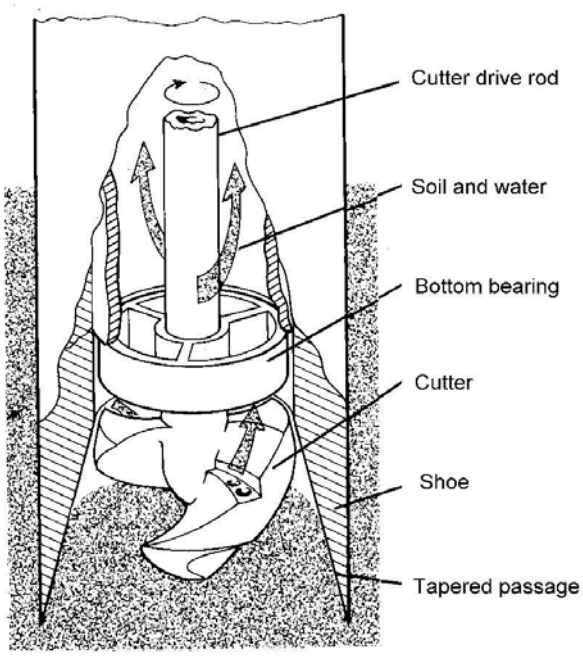

Fig 5.2 The Low Disturbance Drilling System used on a self-boring pressuremeter (figure courtesy of Cambridge Insitu)

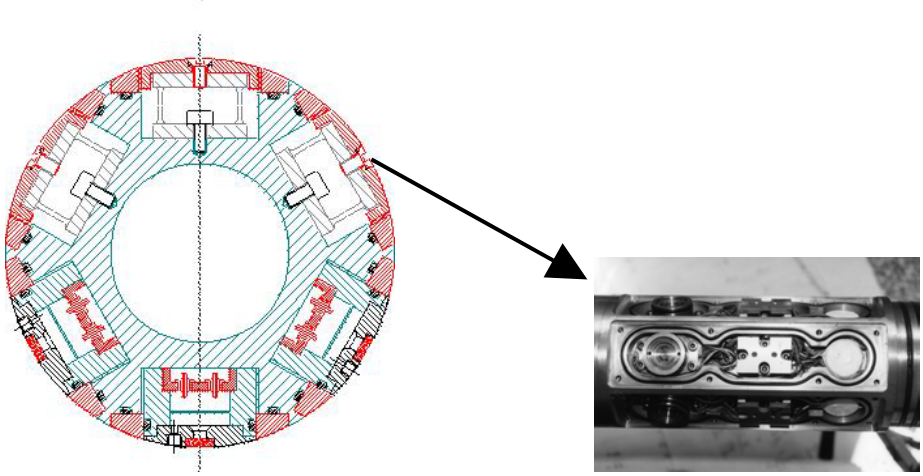

Fig 5.3 Cross-section of the LCPM (drawing and photo courtesy of Cambridge Insitu)

The general testing process is as follows. Spaced equally around the circumference of the probe are six compartments sealed with a flush mounted cap (Fig 5.3). Each compartment contains a load cell fixed to the cap, an internal pressure transducer and a pore water pressure transducer. Each compartment is separately linked to a gas source on the surface. Ideally, throughout the drilling and settling, deflections of a load cell trigger the gas control system in order to maintain the load cell at a null stress position. The gas pressure required to do this is measured by the internal pressure transducer giving a direct reading of the external stress acting on the cell cap. In practice, the system reaches equilibrium with the load cell in a mildly stressed state. The earth pressure at which this occurs is obtained by combining the output of the internal pressure transducer with that of the load cell (see Section 5.4.2). All the measurements are transmitted to the surface by a protected cable passing up inside the gas supply line.

The main advantages and disadvantages of an LCPM test can be respectively summarized as follows. The advantages are: (i) Complex interpretation of the stress results is unnecessary as the instrument gives direct readings of in situ stresses. The lateral stresses are simply obtained from the cell outputs and obviate the complexity of interpreting the strain arm data, as is the case with the expansion type pressuremeter. (ii) The use of six cell clusters also gives a more reliable lateral stress measurement and provides greater redundancy in the event of a transducer failure. (iii) The readings can be repeated as often and for as long as required, even for days or weeks, if necessary. The disadvantages are: (i) Installation of LCPM in gravels, claystones or soils containing significant proportion of gravel-sized particles is quite difficult. Therefore, it may be unsuitable for the measurement of in situ stresses in tills. (ii) Results obtained are sometimes surprising and, in several cases, these results have challenged conventional assumptions of soil mechanics.

5.4 LCPM Testing Modes and Output Parameters

5.4.1 Active and passive modes

The two working modes for the LCPM test are respectively the active mode and the passive mode (Fig 5.4). The former refers to the mode in which the load cells will measure soil lateral stress directly with no balancing internal gas pressure. The latter

refers to the mode in which the instrument will normally be used in the null sensing condition. If used in direct mode the instrument would be subjected to error owing to the small movements of the top plate developed under load. Although this movement is small, it will still cause significantly low readings in the measured soil stress. In ideal null sensing mode, the load and total stress cell control systems are zeroed on the ground surface. Throughout the drilling and when testing at each depth, the internal gas pressure is in balance with the external soil stress.

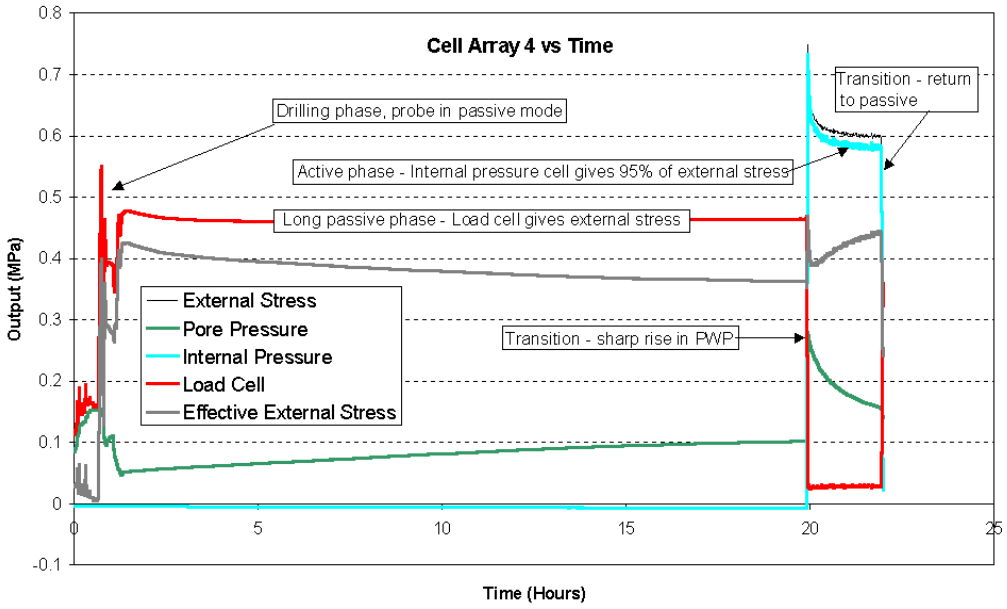

Fig 5.4 A typical output of one of the six arrays

5.4.2 Output parameters

There are two types of output parameters for the LCPM test provided by the accompanying Cambridge Insitu data logging program, namely, the directly measured parameters and the calculated parameters (Fig 5.4). The former group includes: (i) Pore water pressure (PPC); (ii) Load cell pressure (LCP); (iii) Internal gas pressure cell (IP). The latter group includes: (i) External stress (TPC) that is the sum of the load cell pressure and the internal gas pressure; (ii) Effective external stress (EPC) that is derived by subtracting the measured pore water pressure from the total pressure.

5.5 Genuine Anisotropy and Apparent Anisotropy

In most LCPM tests, variation in the six output values is seen. This variation could be due to anisotropy of the lateral stresses (genuine anisotropy), or drilling disturbance (apparent anisotropy). An intrinsic criterion to separate these two effects is that anisotropy has the same effect on opposing arms but drilling disturbance has the opposite. If a genuine anisotropy exists, the variation of stresses in the horizontal plane is governed by:

$$\sigma = \frac{(\sigma_1 + \sigma_2)}{2} + \frac{(\sigma_1 - \sigma_2)}{2}\cos 2\theta \qquad (5.1)$$

where σ_1 is the major principal stress and σ_2 is the minor principal stress in the horizontal plane and 2θ is the angle subtended at the center of the Mohr's stress circle by the radii representing σ and σ_1. Apparent anisotropy caused by drilling disturbance, such as non-vertical drilling with the probe deviating off to one side along a curved path, would show an increase in stress on the outside of the curve and a reduction on the inside. This can be approximately represented by another formula (Whittle, 2004):

$$\sigma = \frac{(\sigma_1 + \sigma_2)}{2} + \frac{(\sigma_1 - \sigma_2)}{2}\cos \theta \qquad (5.2)$$

The six-load cell LCPM offers a means of assessing the data for consistency, because the Mohr's circle can be resolved with any three of the output stress values following the generalized procedure proposed by the author (Appendix A). In practice, there are many reasons why the soil may appear to have anisotropic properties:

(i) The probe may not have been inserted perfectly vertical.
(ii) The instrument may have a defect, such as being bent.
(iii) The self-boring process may have caused irrecoverable disturbance to the ground.
(iv) Other localized disturbances, like a stone adjacent to an arm.

Anisotropy is apparent in most tests carried out with self-boring probes. Cambridge Insitu suggests that instrument factors are a major influence and the results of the anisotropy analyses should be considered with a degree of skepticism. For the

convenience and consistency of the data interpretation in the subsequent section, the following criteria will be considered:

(1) The lateral stress distribution at a depth will be plotted as Mohr's circles using the even-cell data, odd-cell data and paired-cell data, respectively. This plot together with the plot of the measured points would be helpful for drawing a conclusion correctly.
(2) The lateral stress distribution with anisotropic ratio less than 1.3 will be considered as essentially isotropic.
(3) If the distribution of lateral stress was found to have deviated to one side, it would be considered as drilling disturbance.
(4) For the case that the maximum and the minimum values appear as a pair, it would be attributed to drilling disturbance.
(5) For the genuine anisotropy, all six values should be completely matched.
(6) The fact that the difference between the major and minor stress has to be supported by the shear strength of the soil gives a means of identifying implausible values. As shown later, this criterion was violated due to the surprising low values of the effective stress in these tests.

5.6 Results and Discussions

As mentioned above, one of the advantages of the LCPM test is the direct usage of the output readings. Thus, the data interpretation mainly focuses on inspecting the reasonability of the output data and distinguishing between the genuine anisotropy and the apparent anisotropy of the horizontal stress distribution. Again, the calculation associated with the anisotropic distribution uses the generalized procedure for anisotropy analysis described in Appendix A.

5.6.1 Borehole9

Borehole9 was initially 9 m deep. The first testing started while drilling to a depth of 9.5 m. The last testing was performed at a maximum depth of 14.4 m. A total of seven depths (9.5 m, 10 m, 10.3 m, 11.3 m, 12.3 m, 13.3 m and 14.4 m respectively) were

tested in this borehole. The calibrated data during the stable states are summarized in Table 5.1. The distribution of horizontal effective stress with depth is shown in Fig 5.5 and the distribution of K_0 with depth is shown in Fig 5.6. From the summary of results shown in Table 5.1, it can be seen that at depths of 9.5 m, 10 m and 10.3 m all readings from the pore pressure cells (PPC) exhibit irregular states. From the depth of 11.3 m on, most of the pore water pressure readings except those from clusters 2 and 4 approximately followed the assumed hydrostatic line that was determined based on the in situ observation of a stable ground water table at a depth of about 0.5 m below the ground surface during the whole testing period. Thus, all effective horizontal stress values were corrected with this ideal hydrostatic pressure. Unsurprisingly, the corrected effective horizontal stress data (Table 5.1) at the depths of 9.5 m, 10 m and 10.3 m are anomalous, because the actual insertion depths were small (less than 1.5 m) and the disturbance could be significant. Therefore, these three groups of data will be discarded in the subsequent discussions. The individual effective lateral stress ranges from 27 kPa to 126 kPa, corresponding to K_0 values from 0.18 to 0.86 (assuming a saturated density of 2 Mg/m^3); the paired effective lateral stress ranges from 34 kPa to 101 kPa, corresponding to K_0 values from 0.23 to 0.75 and an average of 0.46.

Table 5.1 Borehole9 – Summary of calibrated test results

Depth of Sensor (m)		9.5	10	10.3	11.3	12.3	13.3	14.4	14.4
Mode		Active	Active	Active	Active	Active	Active	Active	Active
IP (kPa)	1	291.5	145.0	183.0	153.0	152.0	154.0	151.0	148.0
	2	317.0	138.0	191.0	156.0	160.0	189.0	161.0	152.0
	3	310.0	100.0	177.0	147.0	136.0	172.0	145.0	133.0
	4	290.0	88.0	174.0	126.0	160.0	150.0	157.0	153.0
	5	278.0	130.0	210.0	165.0	188.0	210.0	237.0	230.0
	6	328.0	99.0	199.0	152.0	125.0	144.0	143.0	153.0
	1---4	290.8	116.5	178.5	139.5	156.0	152.0	154.0	150.5
	2---5	297.5	134.0	200.5	160.5	174.0	199.5	199.0	191.0
	3---6	319.0	99.5	188.0	149.5	130.5	158.0	144.0	143.0
LC (kPa)	1	22.5	30.0	25.0	26.0	30.0	30.0	30.0	30.0
	2	25.0	28.0	28.0	30.0	30.0	30.0	30.0	30.0
	3	30.0	30.0	30.0	30.0	30.0	30.0	30.0	30.0
	4	20.0	30.0	25.0	30.0	25.0	25.0	25.0	25.0
	5	25.0	25.0	25.0	26.0	26.0	25.0	25.0	25.0
	6	20.0	25.0	25.0	26.0	27.0	25.0	25.0	25.0
	1---4	21.3	30.0	25.0	28.0	27.5	27.5	27.5	27.5
	2---5	25.0	26.5	26.5	28.0	28.0	27.5	27.5	27.5
	3---6	25.0	27.5	27.5	28.0	28.5	27.5	27.5	27.5
PPC (kPa)	1	94	102	118	111	118	126	138	137
	2	48	46	48	37	27	20	37	33
	3	107	102	170	119	123	130	143	139
	4	143	89	124	89	75	60	60	58
	5	172	106	122	121	130	136	146	143
	6	205	107	129	120	127	129	139	138
	1---4	118.5	95.5	121	100	96.5	93	99	97.5
	2---5	110	76	85	79	78.5	78	91.5	88
	3---6	156	104.5	149.5	119.5	125	129.5	141	138.5
TS (kPa)	1	314	175	208	179	182	184	181	178
	2	342	166	219	186	190	219	191	182
	3	340	130	207	177	166	202	175	163
	4	310	118	199	156	185	175	182	178
	5	303	155	235	191	214	235	262	255
	6	348	124	224	178	152	169	168	178
	1---4	312.0	146.5	203.5	167.5	183.5	179.5	181.5	178.0
	2---5	322.5	160.5	227.0	188.5	202.0	227.0	226.5	218.5
	3---6	344.0	127.0	215.5	177.5	159.0	185.5	171.5	170.5
ES (kPa)	1	225.7	81.8	111.9	73.1	66.2	58.4	44.6	41.6
	2	253.7	72.8	122.9	80.1	74.2	93.4	54.6	45.6
	3	251.7	36.8	110.9	71.1	50.2	76.4	38.6	26.6
	4	221.7	24.8	102.9	50.1	69.2	49.4	45.6	41.6
	5	214.7	61.8	138.9	85.1	98.2	109.4	125.6	118.6
	6	259.7	30.8	127.9	72.1	36.2	43.4	31.6	41.6
	1---4	223.7	53.3	107.4	61.6	67.7	53.9	45.1	41.6
	2---5	234.2	67.3	130.9	82.6	86.2	101.4	90.1	82.1
	3---6	255.7	33.8	119.4	71.6	43.2	59.9	35.1	34.1
K0	1	2.3	0.8	1.1	0.6	0.5	0.4	0.3	0.3
	2	2.6	0.7	1.2	0.7	0.6	0.7	0.4	0.3
	3	2.6	0.4	1.0	0.6	0.4	0.6	0.3	0.2
	4	2.3	0.2	1.0	0.4	0.6	0.4	0.3	0.3
	5	2.2	0.6	1.3	0.7	0.8	0.8	0.9	0.8
	6	2.6	0.3	1.2	0.6	0.3	0.3	0.2	0.3
	1---4	2.3	0.5	1.0	0.5	0.5	0.4	0.3	0.3
	2---5	2.4	0.7	1.2	0.7	0.7	0.7	0.6	0.6
	3---6	2.6	0.3	1.1	0.6	0.3	0.4	0.2	0.2

Note: The W.T. lies at 0.5m below the ground. This observation is used for subsequent calculation.

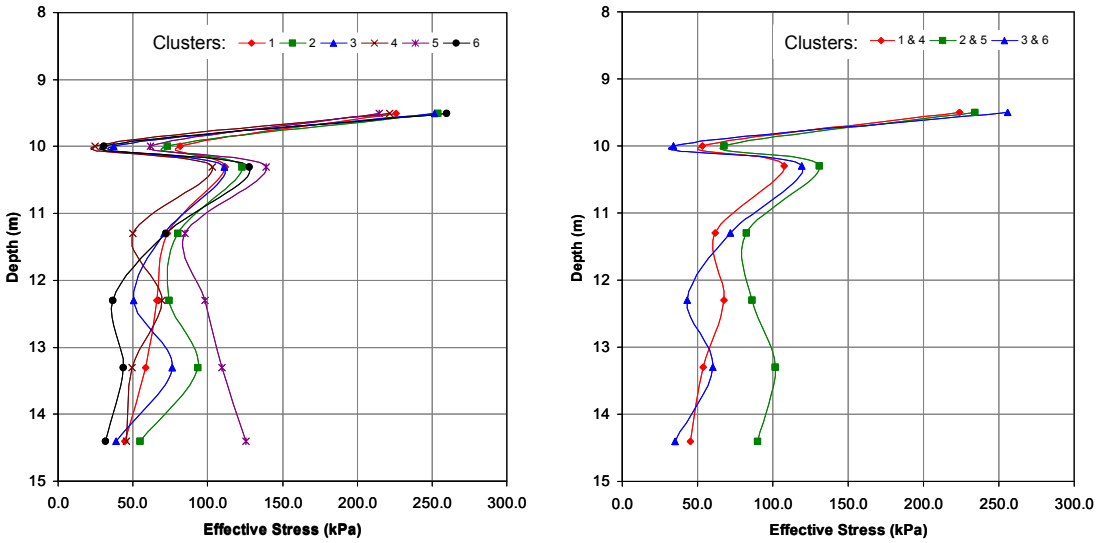

Fig 5.5 Borehole9 - Distribution of horizontal effective stress with depth

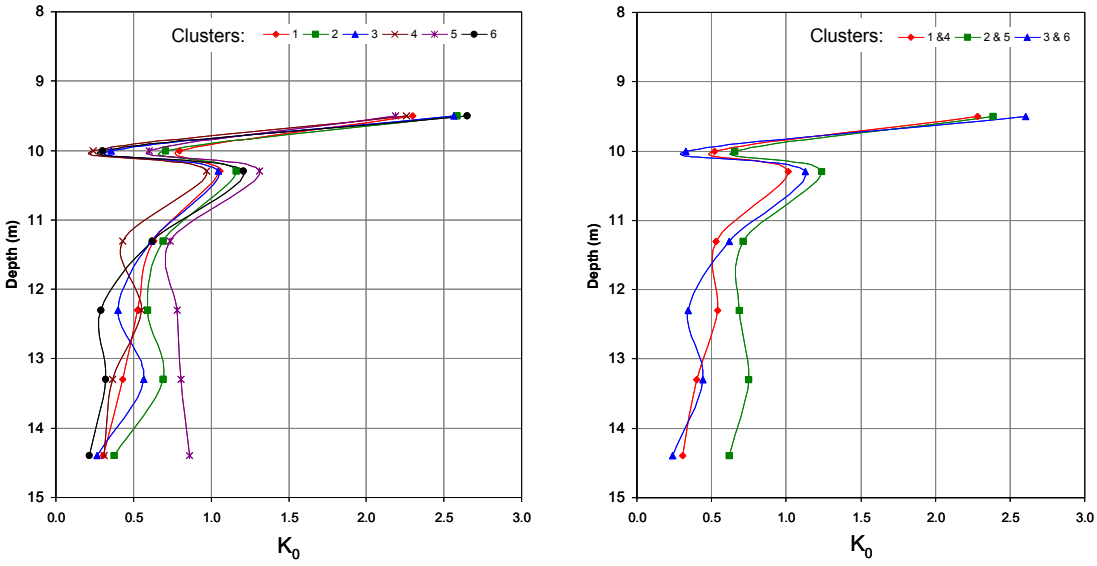

Fig 5.6 Borehole9 – Distribution of K_0 with depth

The distributions of in situ horizontal effective stress in a horizontal plane at four different depths (11.3 m, 12.3 m, 13.3 m and 14.4 m) are shown in Fig 5.7, Fig 5.8, Fig 5.9 and Fig 5.10, respectively. At the depth of 11.3 m, the paired anisotropy ratio is equal to 1.15. The only reason for this slight anisotropy is due to the lower reading at cluster 4. This distribution can be considered as isotropic with a mean stress of 178 kPa

and disturbance of ±22 kPa. At the depth of 12.3 m, the paired anisotropy ratio is equal to 1.32. All cross-arm readings are close to a balance. This distribution can be considered as anisotropic with a major stress of 206 kPa and a minor stress of 157 kPa. The orientation of the major stress lies at 42º to Cluster 1. At the depth of 13.3 m, the paired anisotropy ratio is equal to 1.36. However, a pair of slightly unbalanced readings occurred at Cluster 3-6. This distribution can be considered skeptically anisotropic. The major and minor principal stresses are 227 kPa and 167 kPa, respectively. The maximum stress axis orients 63º with respect to Cluster 1. At the depth of 14.4 m, the distribution might be considered isotropic rather than anisotropic although it shows an anisotropy ratio of 1.44. Both the active and passive distributions indicate that the apparent anisotropy is simply due to the abnormally high value on Cluster 5. The mean stress is about 180±20 kPa.

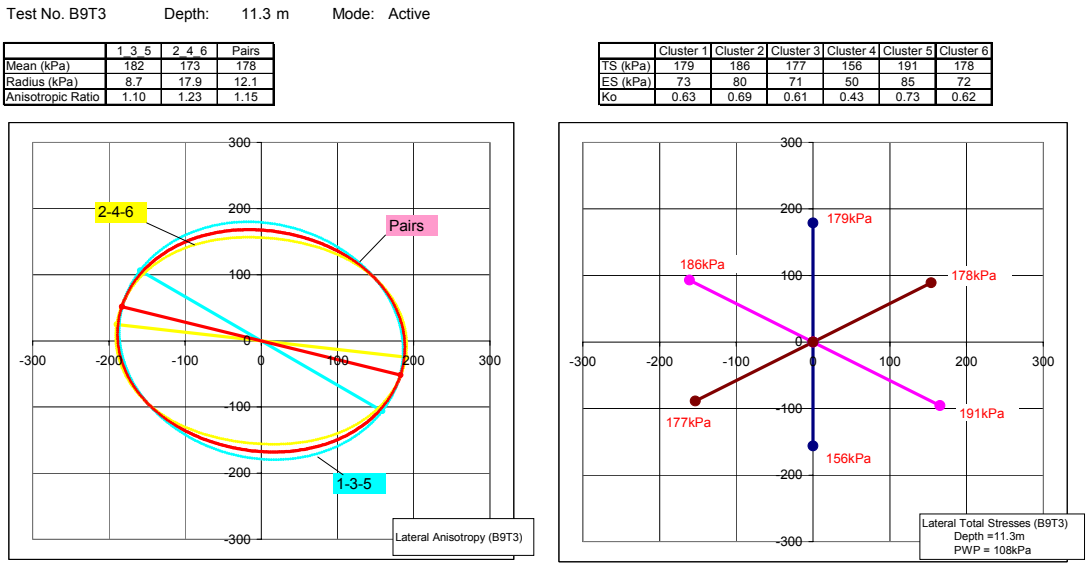

Fig 5.7 Borehole9 – Spatial distribution of in situ lateral stress at 11.3 m depth

Test No. B9T4 Depth: 12.3 m Mode: Active

	1_3_5	2_4_6	Pairs
Mean (kPa)	187	176	182
Radius (kPa)	28.2	23.8	24.9
Anisotropic Ratio	1.35	1.31	1.32

	Cluster 1	Cluster 2	Cluster 3	Cluster 4	Cluster 5	Cluster 6
TS (kPa)	182	190	166	185	214	152
ES (kPa)	66	74	50	69	98	36
Ko	0.53	0.59	0.40	0.55	0.78	0.29

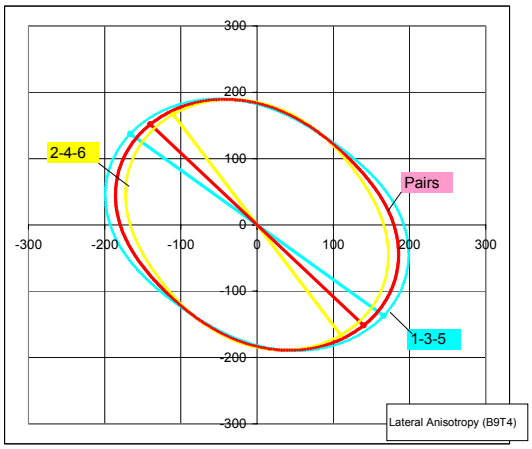

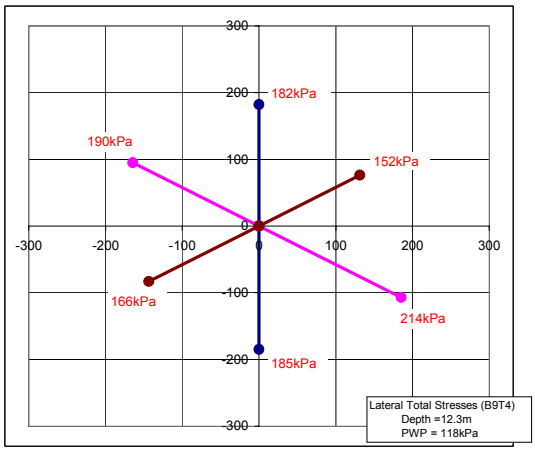

Fig 5.8 Borehole9 – Spatial distribution of in situ lateral stress at 12.3 m depth

Test No. B9T5 Depth: 13.3 m Mode: Active

	1_3_5	2_4_6	Pairs
Mean (kPa)	207	188	197
Radius (kPa)	29.9	31.5	29.9
Anisotropic Ratio	1.34	1.40	1.36

	Cluster 1	Cluster 2	Cluster 3	Cluster 4	Cluster 5	Cluster 6
TS (kPa)	184	219	202	175	235	169
ES (kPa)	58	93	76	49	109	43
Ko	0.43	0.69	0.56	0.37	0.81	0.32

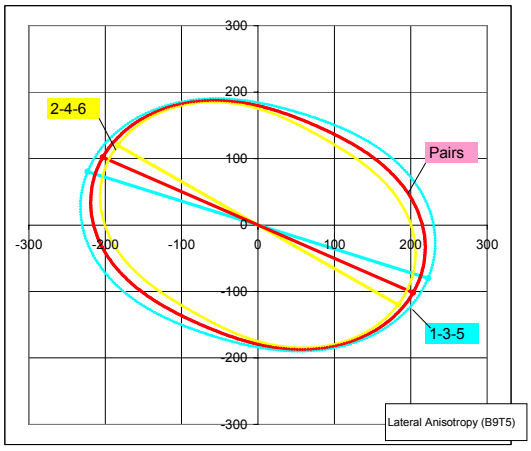

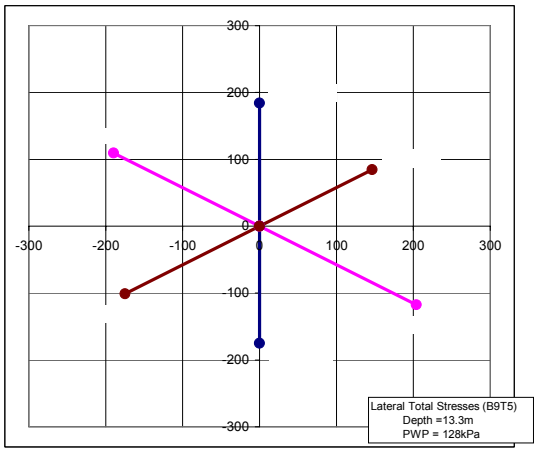

Fig 5.9 Borehole9 – Spatial distribution of in situ lateral stress at 13.3 m depth

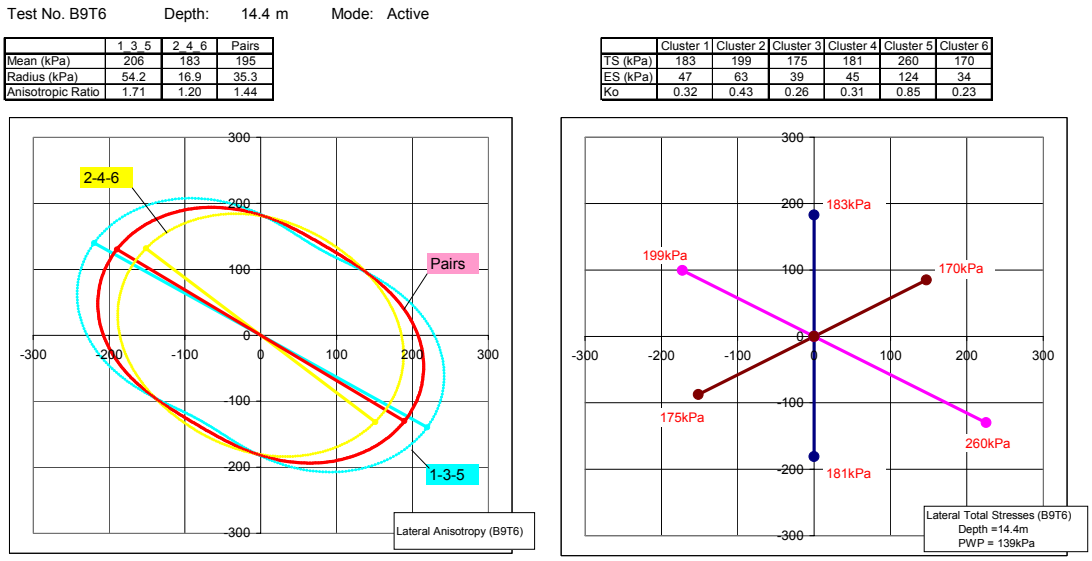

Fig 5.10 Borehole9 – Spatial distribution of in situ lateral stress at 14.4 m depth

Based on the above discussion, the test results obtained from Borehole9 may be summarized as follows:

(1) Some of the pore water pressure readings are abnormal. This might be attributed to the effects of suction or air on the ceramic plate of the pore pressure cells. However, most of pore pressure readings support the assumed hydrostatic profile that will be continuously used in the subsequent data interpretation.

(2) Four groups of horizontal stress distributions are valid and used on the anisotropy analyses. Two of them are considered as genuine anisotropy, while two of them are not. Meanwhile, all the anisotropic distributions are originated from one pair of readings, Clusters2-5. This probably indicates that this anisotropy results from some disturbance. On the other hand, the orientations of the maximum axes are not consistent with the known advance direction of the Saalian glacier.

Therefore, the test data of Borehole9 cannot sufficiently confirm the relationship between the orientation of maximum in situ horizontal effective stress and the known direction of glacial movement.

5.6.2 Borehole20

Borehole20 was the second borehole to be tested in the field. Its initial depth was 20 m. Both active mode testing and passive mode testing were performed at a total of six depths: 21.5 m, 22.5 m, 23.5 m, 24.5 m, and 25.5 m. Table 5.2 summarizes the calibrated data during the stable states. The distribution of horizontal effective stress with depth is shown in Fig 5.11 and the distribution of K_0 with depth is shown in Fig 5.12. It is clear from results shown in Table 5.2 that all the measured pore water pressures should not be considered in this borehole. Therefore, the effective stress values were calculated based on the foregoing assumed hydrostatic profile. Due to the same reasons as Borehole9, the data group at 21.5 m depth was discarded. The individual effective lateral stress exhibits a surprising negative value (Cluster 2, at 23.5 m depth), and a maximum value of 262 kPa corresponding to a K_0 value of 1; the paired effective lateral stress values range from 61 kPa to 242 kPa corresponding to K_0 values from 0.3 to 0.92 with an average value of 0.54.

The distributions of in situ horizontal effective stress in a horizontal plane at four different depths (22.5 m, 23.5 m, 24.5 m and 25.5 m) are shown in Fig 5.13, Fig 5.14, Fig 5.15 and Fig 5.16, respectively. At the depth of 22.5 m, both active mode and passive mode indicate a paired anisotropy ratio of about 1.1. But a typical disturbance due to the probe inclination occurred. Based on the compensated paired readings, this distribution can be considered as isotropic with a mean stress of 300 kPa and disturbance of ±20 kPa. At the depth of 23.5 m, the paired anisotropy ratio of 1.1 was seen. A typical disturbance of inclined drilling continued. Hence, this is an isotropic distribution with a compensated mean horizontal stress of 300 kPa and disturbance of ±15 kPa. At the depth of 24.5 m, similar isotropic distribution to those at the depths of 22.5 m and 23.5 m was observed. A low anisotropy ratio and typical drilling disturbance continued. The compensated mean horizontal stress and disturbance are 330 kPa and ±30 kPa respectively. At the depth of 25.5 m, slight inconsistency occurred on the active and the passive test modes. For the active mode, abrupt increase in the reading on Cluster3-6 was observed. The lateral stress distribution is anisotropic although a relatively low value occurred on Cluster1. The major and minor stresses are 479 kPa and 326 kPa respectively, corresponding to an anisotropy ratio of 1.47. The maximum stress axis

orients 103º to Cluster 1. For the passive mode, compared to the active mode, the effective horizontal stresses on Cluster3-6 significantly decreased. The difference is about 100 kPa. This distribution is still considered anisotropic with a relatively high value on Cluster5. The anisotropy ratio is equal to 1.22 and the orientation of the maximum stress axis is 83º to Cluster1.

Based on the descriptions above, the test results on Borehole20 may be summarized as follows:

(1) The pore water pressure readings are completely discarded. An assumed hydrostatic profile was used in the data interpretation associated with the effective stresses.
(2) Four groups of horizontal stress distributions where both the active mode and passive mode were imposed were inspected on the anisotropy analysis. Only one of them might be considered as genuine anisotropy.

Therefore, the test data of Borehole20 cannot sufficiently demonstrate the existence of anisotropic in situ horizontal stresses.

Table 5.2 Borehole20 – Summary of calibrated test results

Depth of Sensor (m)		21.5	21.5	22.5	22.5	23.5	23.5	24.5	24.5	25.5	25.5	25.5
Mode		Active	Passive	Active	Passive	Active	Passive	Active	Passive	Active	Passive	Active
	1	299	15	236	15	226	10	253	24	288	18	276
	2	428	10	258	10	207	9	280	16	384	-4	383
	3	439	6	281	6	304	6	353	7	443	6	453
	4	476	9	306	10	317	9	372	11	359	11	390
IP (kPa)	5	465	7	306	8	345	6	336	8	415	7	450
	6	554	6	318	16	299	12	349	19	475	19	507
	1---4	387.5	12	271	12.5	271.5	9.5	312.5	17.5	323.5	14.5	333
	2---5	446.5	8.5	282	9	276	7.5	308	12	399.5	1.5	416.5
	3---6	496.5	6	299.5	11	301.5	9	351	13	459	12.5	480
	1	20	331	22	265	24	275	19	277	16	300	18
	2	14	438	18	236	22	204	15	251	12	357	13
	3	19	418	22	276	22	280	19	306	17	365	16
	4	7	430	13	298	14	303	10	325	8	326	8
LC (kPa)	5	3	464	6	300	7	359	4	344	2	416	1
	6	0	485	4	277	6	293	2	305	0	356	0
	1---4	13.5	380.5	17.5	281.5	19	289	14.5	301	12	313	13
	2---5	8.5	451	12	268	14.5	281.5	9.5	297.5	7	386.5	7
	3---6	9.5	451.5	13	276.5	14	286.5	10.5	305.5	8.5	360.5	8
	1	252	264	242	234	239	232	250	246	260	257	260
	2	56	172	39	51	48	56	67	69	75	65	65
	3	264	240	263	245	250	242	265	246	268	255	270
	4	172	197	108	149	75	142	69	122	100	134	138
PPC (kPa)	5	261	270	260	251	254	251	224	259	276	270	274
	6	255	276	180	225	246	241	255	247	268	258	268
	1---4	212	230.5	175	191.5	157	187	159.5	184	180	195.5	199
	2---5	158.5	221	149.5	151	151	153.5	145.5	164	175.5	167.5	169.5
	3---6	259.5	258	221.5	235	248	241.5	260	246.5	268	256.5	269
	1	319	346	258	280	250	285	272	301	304	318	294
	2	442	448	276	246	229	213	295	267	396	353	396
	3	458	424	303	282	326	286	372	313	460	371	469
	4	483	439	319	308	331	312	382	336	367	337	398
TS (kPa)	5	468	471	312	308	352	365	340	352	417	423	451
	6	554	491	322	293	305	305	351	324	475	375	507
	1---4	401.0	392.5	288.5	294.0	290.5	298.5	327.0	318.5	335.5	327.5	346.0
	2---5	455.0	459.5	294.0	277.0	290.5	289.0	317.5	309.5	406.5	388.0	423.5
	3---6	506.0	457.5	312.5	287.5	315.5	295.5	361.5	318.5	467.5	373.0	488.0
	1	113.0	140.0	42.2	64.2	24.4	59.4	36.6	65.6	58.8	72.8	48.8
	2	236.0	242.0	60.2	30.2	3.4	-12.6	59.6	31.6	150.8	107.8	150.8
	3	252.0	218.0	87.2	66.2	100.4	60.4	136.6	77.6	214.8	125.8	223.8
	4	277.0	233.0	103.2	92.2	105.4	86.4	146.6	100.6	121.8	91.8	152.8
ES (kPa)	5	262.0	265.0	96.2	92.2	126.4	139.4	104.6	116.6	171.8	177.8	205.8
	6	348.0	285.0	106.2	77.2	79.4	79.4	115.6	88.6	229.8	129.8	261.8
	1---4	195.0	186.5	72.7	78.2	64.9	72.9	91.6	83.1	90.3	82.3	100.8
	2---5	249.0	253.5	78.2	61.2	64.9	63.4	82.1	74.1	161.3	142.8	178.3
	3---6	300.0	251.5	96.7	71.7	89.9	69.9	126.1	83.1	222.3	127.8	242.8
	1	0.5	0.6	0.2	0.3	0.1	0.3	0.1	0.3	0.2	0.3	0.2
	2	1.1	1.1	0.3	0.1	0.0	-0.1	0.2	0.1	0.6	0.4	0.6
	3	1.2	1.0	0.4	0.3	0.4	0.3	0.6	0.3	0.8	0.5	0.9
	4	1.3	1.1	0.5	0.4	0.4	0.4	0.6	0.4	0.5	0.4	0.6
K_0	5	1.2	1.2	0.4	0.4	0.5	0.6	0.4	0.5	0.7	0.7	0.8
	6	1.6	1.3	0.5	0.3	0.3	0.3	0.5	0.4	0.9	0.5	1.0
	1---4	0.9	0.9	0.3	0.3	0.3	0.3	0.4	0.3	0.4	0.3	0.4
	2---5	1.2	1.2	0.3	0.3	0.3	0.3	0.3	0.3	0.6	0.6	0.7
	3---6	1.4	1.2	0.4	0.3	0.4	0.3	0.5	0.3	0.9	0.5	1.0

Note: The W.T. lies at 0.5m below the ground. This observation is used for subsequent calculation.

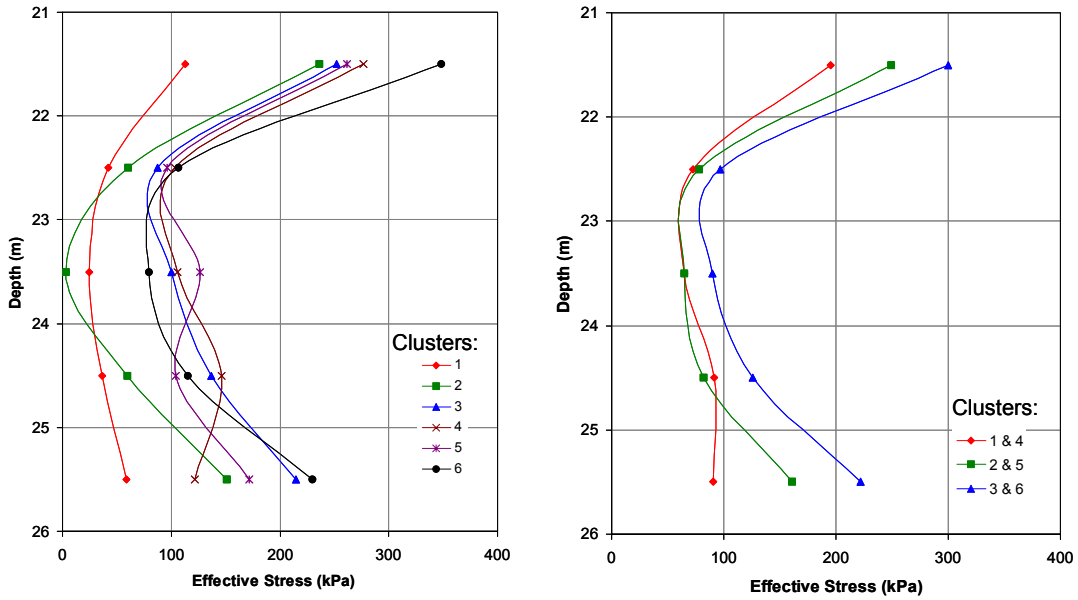

Fig 5.11 Borehole20 - Distribution of horizontal effective stress with depth

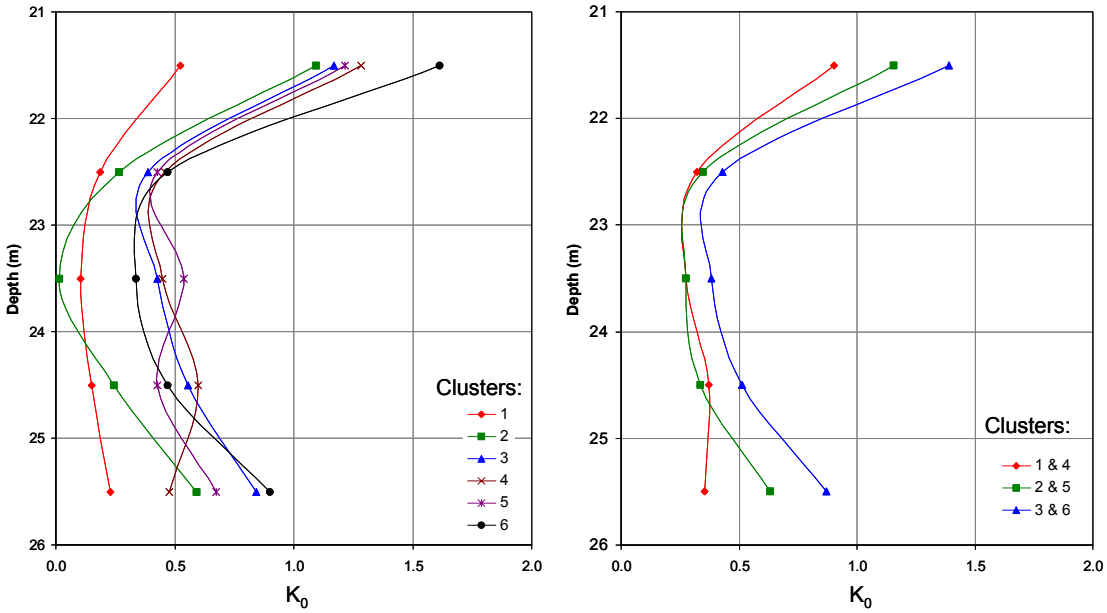

Fig 5.12 Borehole20 - Distribution of K_0 with depth

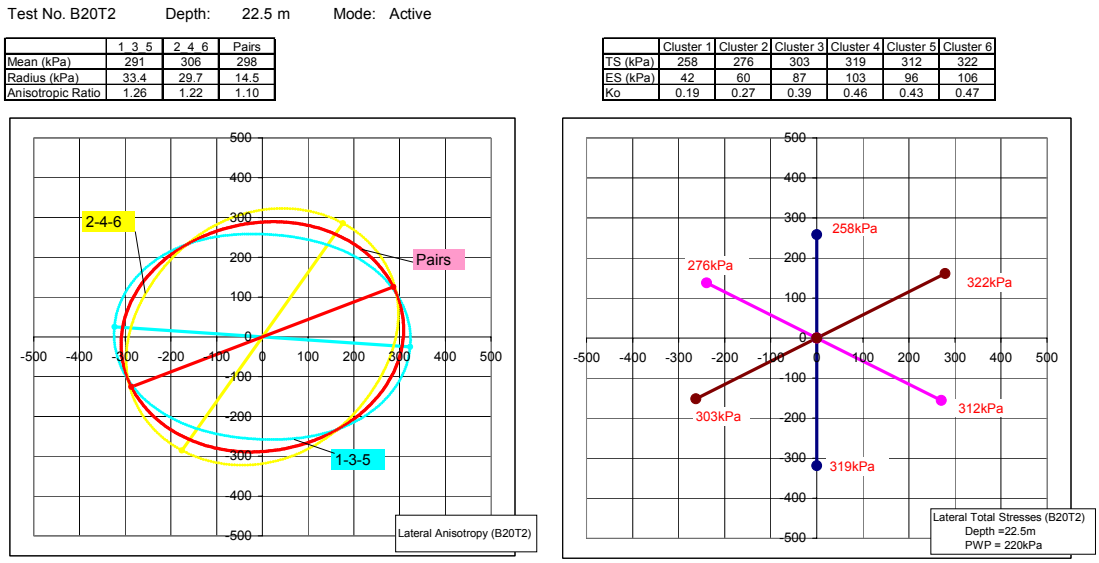

Fig 5.13 Borehole20 – Spatial distribution of in situ lateral stress at 22.5 m depth

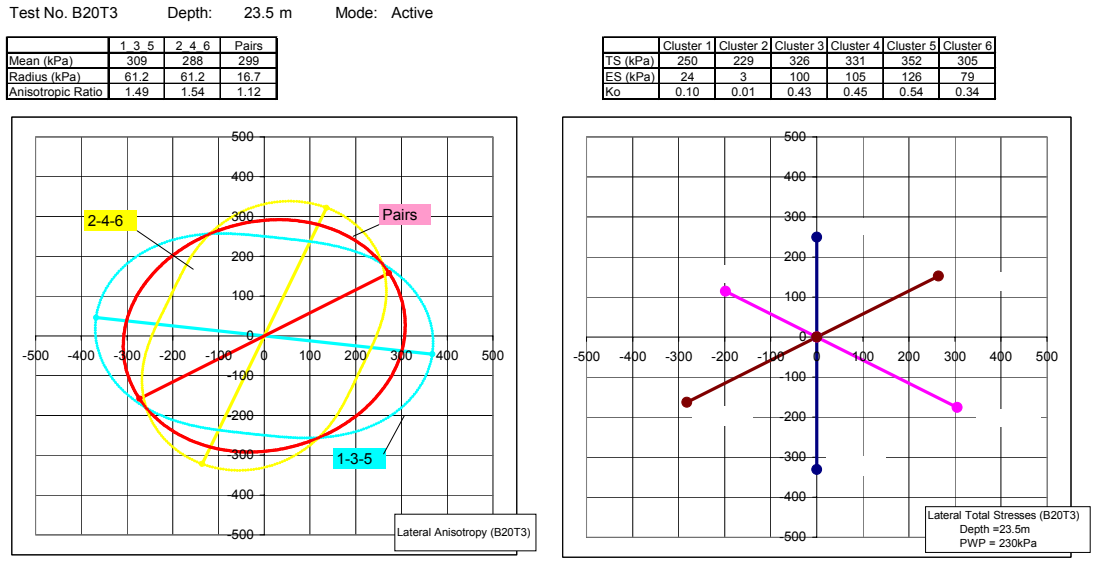

Fig 5.14 Borehole20 – Spatial distribution of in situ lateral stress at 23.5 m depth

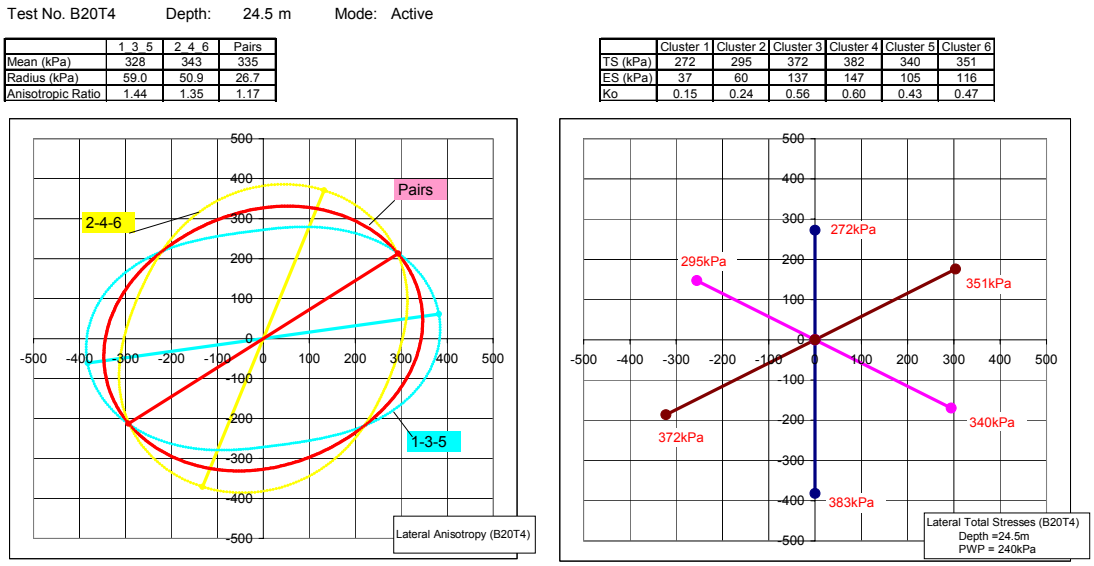

Fig 5.15 Borehole20 – Spatial distribution of in situ lateral stress at 24.5 m depth

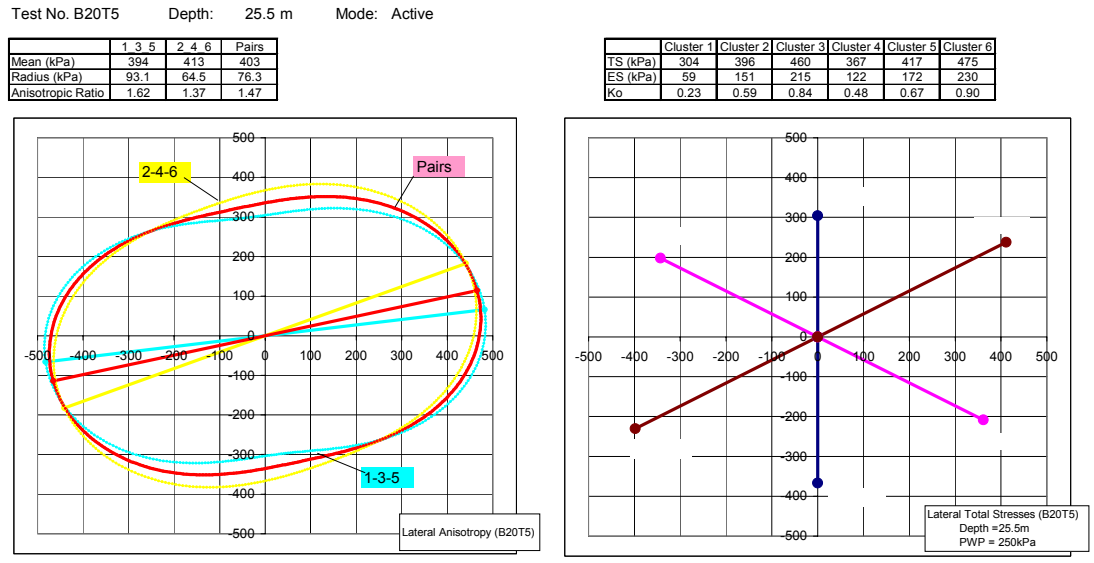

Fig 5.16 Borehole20 – Spatial distribution of in situ lateral stress at 25.5 m depth

5.6.3 Borehole14

Borehole14 was the last borehole to be tested. The data exhibited extremely abnormal states which indicated significant disturbances occurred during the testing process. All the test data on this borehole were discarded.

5.6.4 Discussion

When the generalized anisotropy analysis procedure (Appendix A) is used for the interpretation of LCPM test results, there is some redundancy available that can help in distinguishing genuine anisotropy from the apparent anisotropy. This is because stress measurements are carried out using 6 load cells and all these six stress measurements must plot on the Mohr's stress circle. The generalized anisotropy analysis procedure requires a minimum of three stress measurements along three different radial directions. We can plot the Mohr's stress circle using any three of the six stress measurements and then confirm the validity of the Mohr's stress circle using the remaining three stress measurements. Therefore, the limitation in the analyses of K_0-anisotropy that all of the three readings must be used to develop a single Mohr's circle has been eliminated due to the usage of six arms in the LCPM test.

As shown above, the LCPM test results cannot sufficiently confirm the existence of genuine anisotropy of in situ lateral stresses. This conclusion should not be surprising. If the ground is assumed to be in stress equilibrium, the existence of anisotropic lateral in situ stresses requires the existence of shear stresses on the vertical planes. The likelihood of the existence of shear stresses on the vertical planes is quite small unless the ground surface is sloping. Anisotropic in situ lateral stresses occur in certain specific cases where the stress state in soil is changed temporarily during a construction activity such as the excavation of a tunnel. Such an anisotropic in situ stress state lasts for a limited period. In nature, all systems tend to evolve towards a stable state. As pointed out by Feeser (1988), anisotropic in situ stresses exist during the glaciodynamic stage of the glaciation cycle. Such anisotropic stresses can be considered as an unstable state in the gravitational field. This unstable state will evolve towards a stable state (isotropic lateral stresses) through certain means, for instance, creep. Although the ground may continue to creep for a very long time, the possibility of it still continuing to creep in response to shear stresses applied during the last glaciation is fairly remote.

Finally, it must be emphasized that the possible non-existence of in situ lateral anisotropic stresses does not exclude the existence of other anisotropic geomechanical properties resulting from the Quaternary ice sheets, for example, lateral "stiffness"

anisotropy (K_0-anisotropy). In this regard, encouraging results have been obtained for Pot clay by the researchers of TU Delft, Netherlands (Gareau et al., 2004).

5.7 Summary

LCPM tests were performed to explore in situ lateral stress anisotropy. Two significant advantages of this sort of test are: (i) the self-boring technique reduces the disturbance to an exceptionally small amount; (ii) the usage of six cell clusters provides a possibility to distinguish the genuine anisotropy and the apparent anisotropy. Based on conservative criteria, the results of LCPM tests on Pot clay cannot sufficiently correlate the in situ lateral stress anisotropy with the known direction of Saalian glacier. Moreover, some surprising data (e.g. extremely low K_0 value) need to be further probed. In the author's opinion, in situ lateral stress anisotropy is an unstable state in the gravitational field and can only exist in a limited period. This unstable state always tends to evolve towards a stable state (i.e. isotropic lateral stresses) just as any system in the Great Nature. The results obtained from LCPM testing do not exclude the existence of other properties, for instance, K_0- or "stiffness" anisotropy, which involves the evolution of the lateral stresses during the loading process.

Chapter 6 Consolidation Coupled Shearing Model

6.1 Introduction

Glaciated soils, such as tills that have been formed by moving ice or "glaciotectonite" that have been overrun by glaciers, underlie large areas of the populated earth. In general, one-dimensional consolidation is one of the fundamental mechanisms for the formation of soils and glaciated soils should not be an exception. However, traditional one-dimensional consolidation theory cannot completely explain the consolidation behaviour of glaciated soils. The influence of subglacial shearing, which has been broadly demonstrated in recent glaciological and geophysical studies, may have been considered but never quantified.

The experimental data presented in this thesis suggests that the preconsolidation pressure profile within the Battleford till is nearly vertical. In fact, this is not a surprising discovery for glaciated soils. Numerous researchers (e.g. Sauer et al., 1993; Boulton and Dobbie, 1993; Schokking, 1996) developed theories to explain the preconsolidation pressure patterns observed in practice. All of these are one-dimensional consolidation models and depend significantly on the boundary conditions imposed. These theories can be retraced back to Casagrande's hypothesis (1936). One of the reasons that the preconsolidation pressure profile deviates from the gravitational gradient can be due to the effect of the potential water pressure gradient relying significantly on the boundary conditions. Additionally, Sauer et al. (1993) argued that during the period of glaciation, the degree of consolidation might also affect the preconsolidation pressure pattern measured today. Although these models can elaborately explain the observed phenomena at specific sites, none of them are generally applicable. In reality, tills exhibit surprisingly homogeneous consolidation behaviour. Sauer et al. (1993) studied consolidation properties of tills and intertill clays over a 1300 km north-south transect in Canada and found that the preconsolidation pressures of all the pre-Battleford Formation tills were generally in the range of 1800 ± 200 kPa, independent of known past ice sheet profile. Fountain (1994) measured the pore pressures at the base of the South Cascade

Glacier in Washington State, USA. He found that the effective stresses are uniformly between 100 and 150 kPa, for ice thickness between 40 and 200 m. This is in the same order of magnitude as the measurement at the base of an Antarctic ice stream of 1000 m thickness (Engelhardt et al., 1990). Obviously, these are unlikely explained by the traditional one-dimensional consolidation theory. It appears that there exists a certain common formation mechanism beneath the past continental ice sheets.

There are two main conceptual paradigms available to understand the dynamic behaviour of ice sheets. These are the sliding over a rigid surface (e.g. Weertman, 1979) and the subglacial shear deformation at high pore pressure (e.g. Boulton and Jones, 1979). Since large areas of the Pleistocene ice sheets in North America and northwest Europe were underlain by thick, unlithified sediment sequences, subglacial shearing would be a general characteristic related to the ice sheet movement. In other words, the effects of shear action may have influenced the present engineering properties of glaciated soils. In fact, recent studies in the Netherlands (Schokking, 1996; Gareau et al., 2004) suggest anisotropic horizontal stresses and stiffness as a result of glacial shearing. As a general rule, normally consolidated and lightly overconsolidated soils when subjected to shearing tend to harden whereas heavily overconsolidated soils tend to soften. Therefore, taking shearing into account would provide an alternative explanation for the formation of the present properties of glaciated soils.

In this chapter, a new glacial process model, consolidation coupled shearing, is presented. The proposed model is based on the framework of traditional soil mechanics (one-dimensional consolidation theory, the critical state theory and the modified Cam-clay constitutive model) combined with the general theories of glaciology and geophysics. Since the main objective herein is to depict the general effects of subglacial shearing on the present properties of glaciated soils, quantitative analysis will be based on classical triaxial conditions. It is worth noting that the accuracy that could be achieved by consideration of details (e.g. anisotropic constitutive relationship, plane strain condition) will never exceed the uncertainties of the geological process itself. Essential features of the effect of subglacial shear can be better revealed by this simplified arrangement.

6.2 Subglacially-deformed Materials

In this thesis, an idealized twofold structure that forms the foundation of structures at present will be considered:

(i) a homogeneous zone, which is the youngest part of the sequence and has been highly remolded by subglacial shear, and

(ii) a sheared zone, which is the parent material but has been subjected to penetrative deformation.

6.2.1 Mechanical Characteristics

Till is a granular material, and as such can be expected to have the characteristics of an elastic-plastic material, with a yield stress determined by a Mohr-Coulomb failure criterion due to internal frictional slip (Fowler, 2003). Indeed, much recent field and laboratory studies demonstrated that the behaviour of till is consistent with other experimental evidence regarding the mechanical behaviour of granular materials (e.g. Kamb, 1991; Iverson et al., 1997; Tulaczyk et al., 2000). Data from laboratory geotechnical tests on till (UpB till) recovered beneath Ice Stream B, West Antarctica (Tulaczyk et al., 2000) show that:

(1) The UpB till follows closely Coulomb's equation in which shear strength is a linear function of normal effective stress with apparent cohesion near zero and internal friction angle equal to 24°. It is also noted that the relatively constant value of till failure strength with strain is in agreement with the prediction of critical state soil mechanics.

(2) Confined compressibility of till is best described by a logarithmic function that relates void ratio to normal effective stress. The slopes of the Normal Compression Line (NCL) and Unloading-Reloading Line (URL) correspond to the values of compression indices in the virgin and the overconsolidated states, $C_c \approx 0.12$ to 0.15 versus $C_s \approx 0.02$, respectively. These indices fall within the lower part of the range of values measured on tills and other soils (Sauer et al., 1993).

(3) Till, as other granular materials, has state-dependent yield stresses and exhibits strain-hardening or strain-softening behaviour. Ring-shear tests show that tills

have a tendency to reduce their strength at large strains. On the other hand, similar tests that allow pore pressure to vary show that both hardening and softening can occur, depending on the initial porosity (Iverson et al., 2000; Moore and Iverson, 2002).

Based on these facts, deformable tills that formed under the ice sheets in the past can then be analyzed in the framework of critical state soil mechanics.

6.3 Relevant Review from Soil Mechanics

6.3.1 1-D consolidation theory

As a fully saturated soil of low permeability is subjected to a change in total stress, excess pore water pressure will develop. If drainage is allowed, water begins to flow until the excess pore water pressure has completely dissipated. This process is always accompanied by volume change. If the excess pore pressure is positive so that the soil tends to decrease in volume, it is called consolidation. If the excess pore pressure is negative so that the soil tends to increase in volume, it is called swelling.

The process of consolidation (or swelling) is governed by the equations of equilibrium for an element of soil, the stress-strain relationship for the mineral skeleton and the continuity equation for the pore fluid. For the simple one-dimensional case, the governing equations are as follows:

Equilibrium:

$$\sigma_v = \gamma_t z + \sigma_{surf} \tag{6.1}$$

where σ_v is the vertical stress at a given depth z, γ_t is the unit weight of the soil and σ_{surf} is the normal (vertical) stress at the ground surface.

Stress-strain:

$$\frac{\partial e}{\partial \sigma_v'} = -m_v(1+e) \tag{6.2}$$

where e is the void ratio, σ_v' is the vertical effective stress and m_v is the coefficient of volume compressibility.

Continuity:

$$k\frac{\partial^2 h}{\partial z^2} = \frac{1}{(1+e)}\frac{\partial e}{\partial t} \tag{6.3}$$

where h is the total head and t is the time.

These equations can be combined as:

$$C_v\frac{\partial^2 u_e}{\partial z^2} = \frac{\partial u_e}{\partial t} - \frac{\partial \sigma_v}{\partial t} \tag{6.4}$$

where the coefficient of consolidation (or swelling), C_v, is defined as:

$$C_v = \frac{k}{\gamma_w m_v} \tag{6.5}$$

Equation (6.4) is known as Terzaghi's consolidation equation.

6.4 The Modified Cam Clay (MCC) Model

The mechanical behaviour of soils is basically elastic-plastic, i.e. under a loading-unloading cycle, only a small part of the strains are recovered (elastic or reversible) whereas the other part remains as permanent (plastic or irreversible). For an elastoplastic constitutive model of soil behaviour, the total incremental strain would be subdivided into elastic and plastic components, treated within the framework of elasticity and plasticity theories, respectively. In general, the ingredients of an elastoplastic model are: (i) Elastic properties; (ii) Yield surface; (iii) Plastic potential (i.e. flow rule); (iv) Hardening rule (Wood, 1992).

The MCC model (Roscoe and Burland, 1968) was proposed based on the modification of the Cam Clay model (Roscoe, Schofield and Wroth, 1958). The MCC model is an isotropic model developed using the conventional triaxial condition ($\sigma_2 = \sigma_3$ and $\varepsilon_2 = \varepsilon_3$). Therefore, it can be studied in a principal effective stress space.

Since complex mathematical skills provide little help in revealing the essentials of subglacial shearing during the glacial process, the model will be described in terms of deviatoric stress q and mean effective pressure p'. In triaxial condition, q and p' can be defined as $q = \sigma_1' - \sigma_3'$ and $p' = (\sigma_1' + 2\sigma_3')/3$ (See Wood, 1992, equations 1.20 and 1.29).

6.4.1 Elastic Properties

Based on a simple extension of the isotropic generalized Hooke's law, the elastic stress-strain relationship follows:

$$\begin{bmatrix} \delta\varepsilon_p^e \\ \delta\varepsilon_q^e \end{bmatrix} = \begin{bmatrix} 1/K' & 0 \\ 0 & 1/3G' \end{bmatrix} \begin{bmatrix} \delta p' \\ \delta q \end{bmatrix} \tag{6.6}$$

where $\delta\varepsilon$ is incremental strain; superscript e denotes elastic strain and subscripts p and q denote volumetric and deviatoric strains, respectively. In triaxial condition, volumetric and deviatoric strain increments can be defined as $\delta\varepsilon_q = 2(\delta\varepsilon_1 - \delta\varepsilon_3)/3$ and $\delta\varepsilon_p = \delta\varepsilon_1 + 2\delta\varepsilon_3$ (See Wood, 1992, equations 1.31 and 1.27).

The bulk modulus K' increases with mean stress p' as per

$$K' = \frac{\nu}{\kappa} p' \tag{6.7}$$

where v = specific volume and κ = slope of the unloading-reloading line in v-lnp'space; κ is related to the swelling index C_S ($\kappa = 0.434 \times C_S$).

6.4.2 Yield Surface

Elastoplastic theory of soils generally assumes that there exits a zone (termed elastic states) in the stress space such that pure elastic strains occur for any stress path, and beyond this zone both elastic and plastic strains can be produced (termed elastoplastic states) as shown in Fig 6.1.

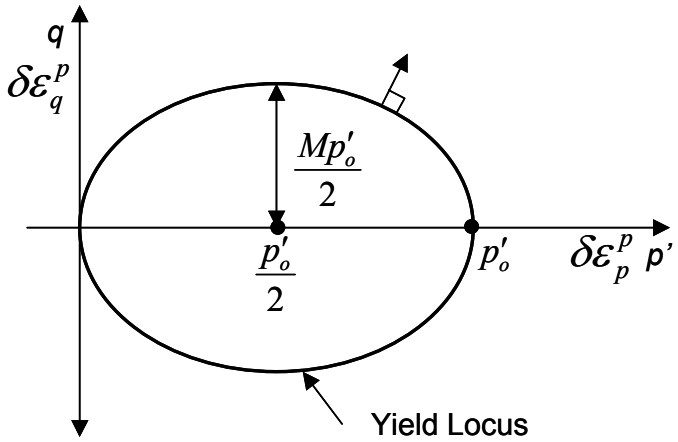

Fig 6.1 Elliptical yield locus for Modified Cam-clay (after Wood, 1992)

In order to distinguish elastic states from elastoplastic states, a scalar function of the state of a soil element is introduced in plasticity theory. This function is called yield function. The yield function is defined such that its value is negative for elastic states and zero for elastoplastic states. Positive values cannot occur for any state.

$f(state) = 0$ [elastoplastic state] (6.8a)

$f(state) < 0$ [elastic state] (6.8b)

In general soil mechanics, the elastic state can be termed as overconsolidated state. An elliptical yield locus in p': q plane is adopted in MCC model as shown in Fig 6.1:

$$\frac{p'}{p'_0} = \frac{M^2}{M^2 + \eta^2} \tag{6.9}$$

where

$\eta = q / p'$

M = slope of the critical state line in q-p' plane

p'_0 = mean effective pressure controlling the size of the yield locus.

Equation (6.9) can be conveniently rewritten as

$$f = q^2 - M^2\left[p'\left(p'_0 - p'\right)\right] = 0 \tag{6.10}$$

6.4.3 Plastic Potential (Flow Rule)

A distinguishing feature of plastic as opposed to elastic response is that the directions of the plastic strain increment vectors are governed, not by the route through stress space that was followed to reach the yield surface, but by the particular combination of stresses at the particular point at which the yield surface was reached. Therefore, a vector of plastic strains can be drawn at each point on the yield surface, and then a plastic potential to which the plastic strain increment vectors are orthogonal can be formed and expressed as a state function $g\left(state\right)$. If the yield surface and the plastic potential for a material are identical, the material is said to follow an "associated" flow rule. In contrast to this case, when the plastic potential surface is not identical to the yield surface (e.g. Lade and Duncan, 1973), the flow rule is said "non-associated". The MCC model adopts the "associated" flow rule that can be expressed as

$$g(state) = f(state) = q^2 - M^2\left[p'\left(p'_0 - p'\right)\right] = 0 \tag{6.11}$$

Then the vector of plastic strain increments $\delta\varepsilon_p^p : \delta\varepsilon_q^p$ is in the direction of the outward normal to the yield locus. That is

$$\frac{\delta\varepsilon_p^p}{\delta\varepsilon_q^p} = \frac{\partial g / \partial p'}{\partial g / \partial q} = \frac{M^2(2p' - p'_0)}{2q} = \frac{M^2 - \eta^2}{2\eta} \tag{6.12}$$

6.4.4 Hardening Rule

The hardening rule of a model describes the relationship between the parameters specifying the size, shape and orientation of the yield surface and the magnitudes of the plastic deformation. When a plastic loading occurs, the yield surface may expand and translate. The uniform expansion of a yield surface is called isotropic hardening. The translation of the yield surface as a rigid body in the *q-p'* stress space is called kinematic hardening.

The MCC model adopts an isotropic hardening rule, which allows the yield surface to expand in the stress space at constant shape (i.e. elliptical), the size being controlled by the tip stress p_0' (the only hardening parameter of the MCC model; see Fig 6.1). The hardening rule can then be expressed as

$$\delta p_0' = \frac{\partial p_0'}{\partial \varepsilon_p^p}\delta \varepsilon_p^p + \frac{\partial p_0'}{\partial \varepsilon_q^p}\delta \varepsilon_q^p \tag{6.13}$$

where superscript *p* denotes plastic incremental strain.

It is assumed that the hardening of the soil is linked with the normal compression of the soil through a linear relationship between the specific volume (v) and logarithm of maximum mean effective stress or preconsolidation pressure (p_0'). This leads to a hardening rule of

$$\delta \varepsilon_p^p = \left[(\lambda - \kappa)/v\right]\frac{\delta p_0'}{p_0'} \tag{6.14a}$$

that can be rewritten as

$$\delta p_0' = \frac{v p_0'}{\lambda - \kappa}\delta \varepsilon_p^p \tag{6.14b}$$

where λ is the slope of the normal compression line in v-lnp' space; it is related to the compression index C_c by $\lambda = (0.434)\cdot C_c$.

6.4.5 The Critical State Concept

An ultimate condition in which deformation (plastic shearing) could continue indefinitely without changes in the shearing resistance or volume has been termed the critical state (Roscoe et al., 1958). At critical state, the soil is being continuously churned up or remolded. However, different patterns of behaviour will exist for different stress systems.

In undrained or drained tests on normally consolidated or lightly overconsolidated soils (AC and AB respectively, Fig 6.2 (a) and (b)), yielding first occurs with stress ratio $\eta < M$. Continued loading, whether undrained or drained, is associated with plastic hardening, expansion of yield loci, and an increase of the stress ratio until ultimately the effective stress state reaches B and C respectively, these points lying on a straight line OS' with stress ratio $\eta = M$. In the compression plane (Fig 6.2(b)), the undrained test will be represented by a horizontal line AB, with the end point B on the left of the start point A; whilst the drained test will be represented by a path AC, with the end point C below the start point A: volumetric compression is expected. Both B and C will lie on a curve S'S' of similar shape of the isotropic consolidation curve. In a three-dimensional q-p'-v plane (Fig 6.2(c)), the line OS' and S'S' combine as a single curve SS, which is known as the critical state line. The stress path AB (Fig 6.2(c)) for an undrained test lies on a plane parallel to the q-p' plane, the value of v being constant throughout the test. The stress path AC (Fig 6.2(c)) for a drained test lies on a plane normal to the q-p' plane.

In undrained or drained tests on heavily overconsolidated soils (DE and DF respectively, Fig 6.2(a) and (b)), yielding first occurs with stress ratio $\eta > M$. Continued deformation is associated with plastic softening, contraction of yield loci, and decrease of stress ratio until ultimately the effective stress state reaches E and F respectively, again these points lying on the straight line OS' with stress ratio $\eta = M$. In the compression plane (Fig 6.2(b)), the undrained test will be represented by a horizontal line DE, with the end point E on the right of the start point D; whilst the drained test will be represented by a curve DF, with the end point F on the top of the start point D: volumetric expansion is expected. Both end points lie on the critical state line again. In a three-dimensional q-p'-v plane (Fig 6.2(c)), the stress path for an undrained test lies on a plane parallel to the q-p' plane, and the stress path for a drained test lies on a plane normal to the q-p' plane. It should be noted that, for heavily overconsolidated soils, critical states will be approached but may not actually be attained because there is a tendency for non-uniformities to develop in these tests.

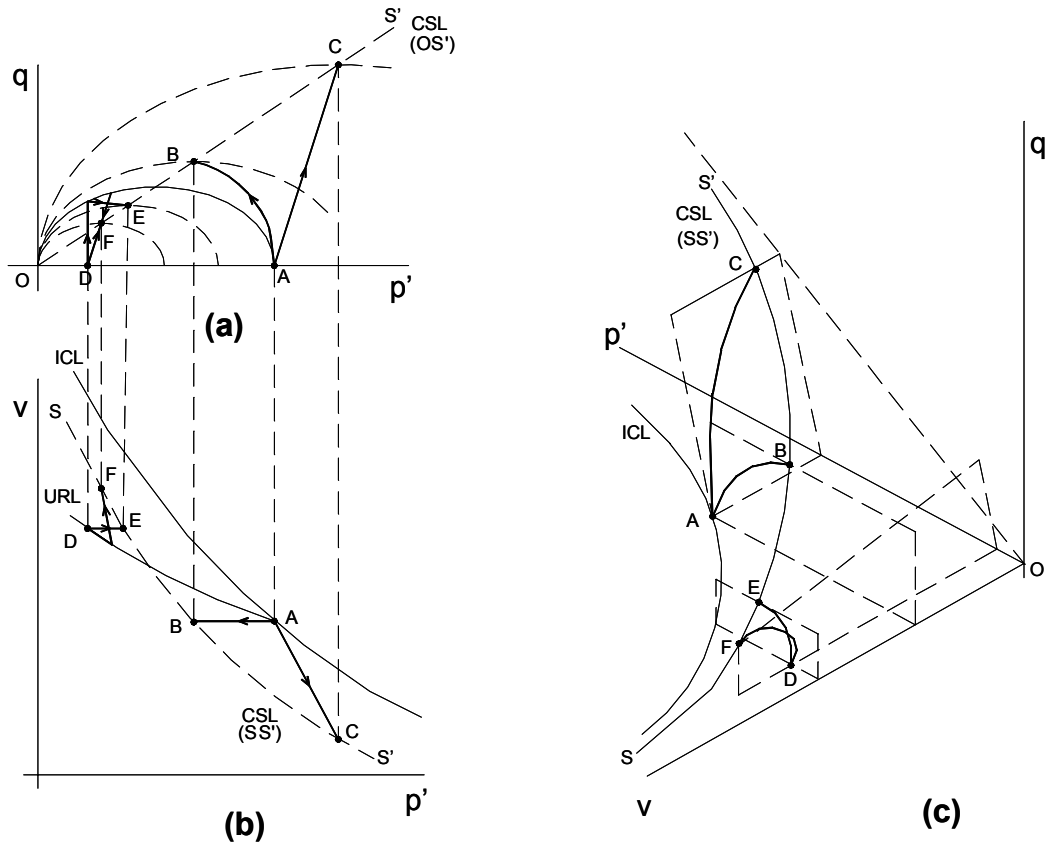

Fig 6.2: (a) Stress paths and yield loci in *q*-p' stress space; (b) Isotropic Compression Line and Critical State Line in *v*-p' space; (c) Critical state line in *q*-*p'*-v space

6.5 Consolidation Coupled Shearing Model

6.5.1 Conceptual Description - Discrete Plate Model

A thick till bed, subjected to pervasive shearing, is idealized as a discrete-plate structure (Fig 6.3). Experimental evidence (e.g. Mandl et al., 1977; Logan et al., 1992; Morgan and Boettcher, 1999) indicates that at sufficiently large strains slip surfaces tend to align with the shearing direction. Thus, shearing can be assumed to occur along a deck of bed-parallel slip planes separated by a uniform distance, δ, much smaller than the bed thickness. Actually, a similar model has been used previously to simulate subglacial dynamic behaviour (Iverson and Iverson, 2000).

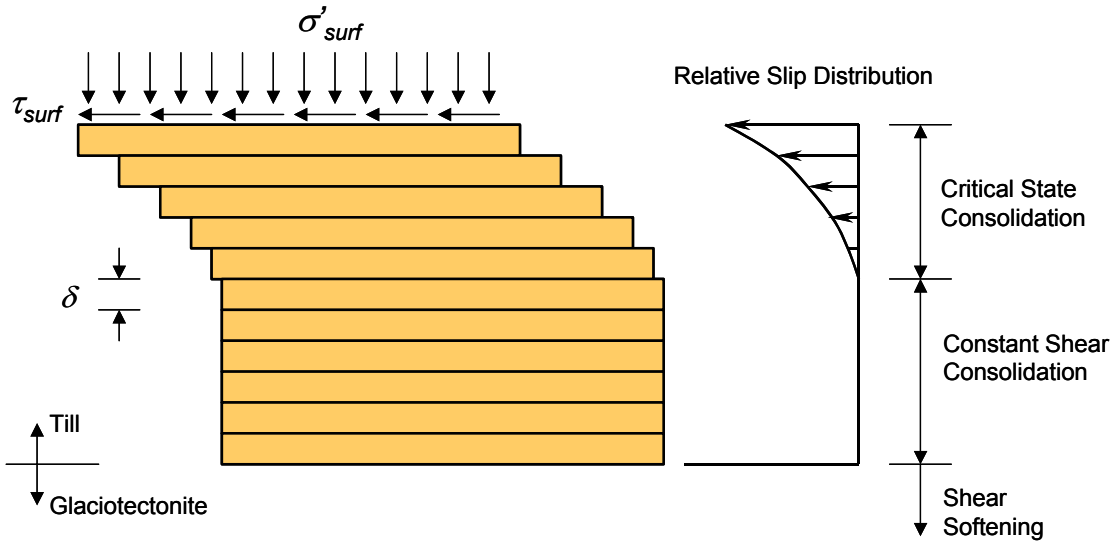

Fig 6.3: Discrete plate model

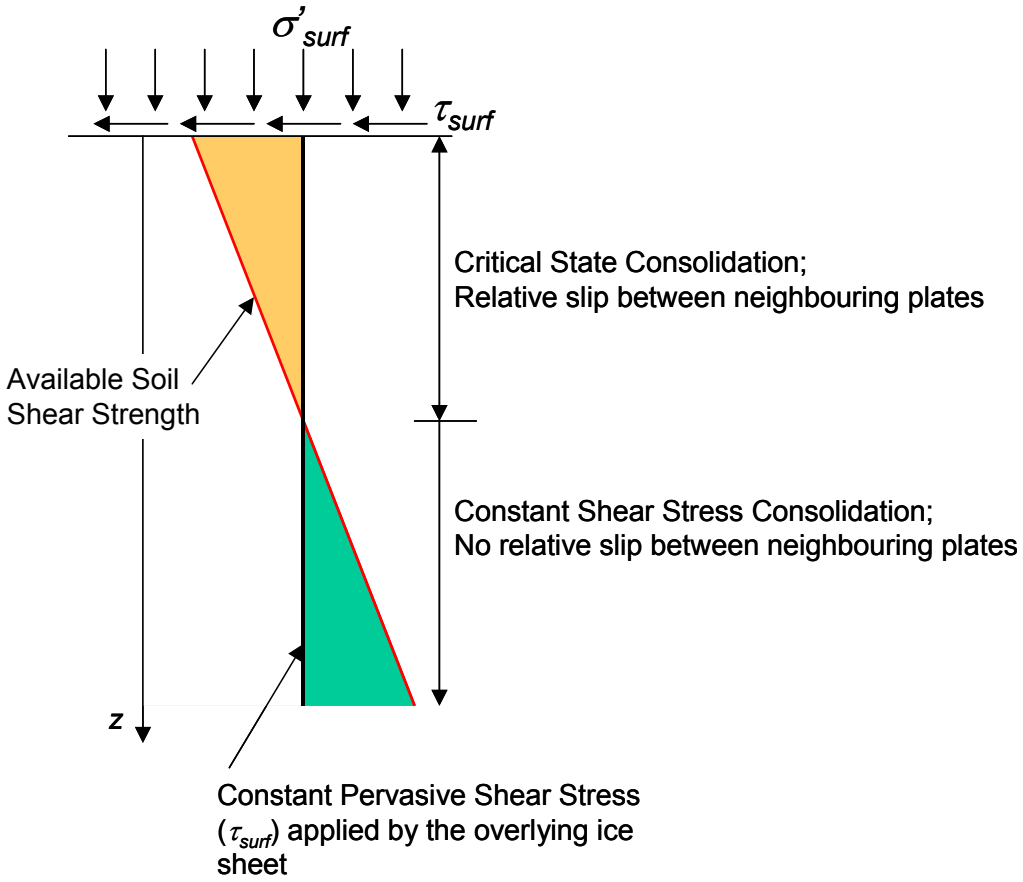

Fig 6.4 Extent of critical state consolidation zone underneath a moving ice sheet

As in distinct-element models of granular shearing, the relative slip along the neighboring plates is assumed to follow Newton's second law (Force = mass × acceleration). The shear stress applied by the overlying ice sheet can be further divided into two portions – a portion that is directly dissipated within the soil (frictional dissipation) determined by the available shear strength of the soil and a portion in excess of the soil shear strength that leads to the relative movement between the neighboring plates. Since the shear strength of soil depends on the effective confining stress, the following scenario is likely for the subglacial structure (see Fig 6.4):

The overlying ice sheet applies a constant pervasive shear stress (τ_{surf}) on the till (Boulton, 1996). This is the threshold (maximum) shear stress soil has to bear. Since the effective confining stress within the till increases linearly with depth, the shear strength of the till (τ_f) must also increase linearly with depth. If $\tau_f < \tau_{surf}$, relative slips between the neighboring plates can occur in response to excess shear stress ($\tau_{surf} - \tau_f$), representing a condition where the soil is being continuously churned up or remolded, which is related to the critical state. During this stage, critical state consolidation takes place (discussed subsequently). If $\tau_f \geq \tau_{surf}$, the glacial shearing will be completely sustained by the soil, and relative slip cannot take place. During this stage, shear consolidation takes place (discussed subsequently). This model is consistent with the known subglacial deformation models (e.g. Banham, 1977; Hart and Boulton, 1991; Boulton, 1996). Additionally, subglacial shear may lead to softening within the glacetectonite sediments (e.g. Sauer et al, 1990; discussed subsequently).

6.5.2 Quantitative analysis

Soils are complex multi-phase materials. It is important to tailor the modelling of material behaviour to the particular problem of interest and the required accuracy of solution (Whittle and Kavvadas, 1994). Since the main objective of this model is to evaluate the shearing effects on preconsolidation pressure and volumetric parameters, the property anisotropy will be temporarily excluded. The MCC model can be used for this purpose. This model is an isotropic model and can be studied in principal stress space (see Kavvadas, 1982). Since complex mathematical procedures provide little help in revealing the essentials of the proposed model, the quantitative analysis will be

performed in the common *q-p'-v* plane. The general tension cut-off and Hvorslev failure criteria will not be considered although they can be easily included. Meanwhile, the realistic K_0-consolidation will be replaced by the isotropic consolidation. Tulaczyk et al. (2000) have reported that there is only a slight difference between isotropic and K_0-consolidation for tills.

6.5.3 Isotropic Preconsolidation Pressure - p'_0

Critical State Consolidation

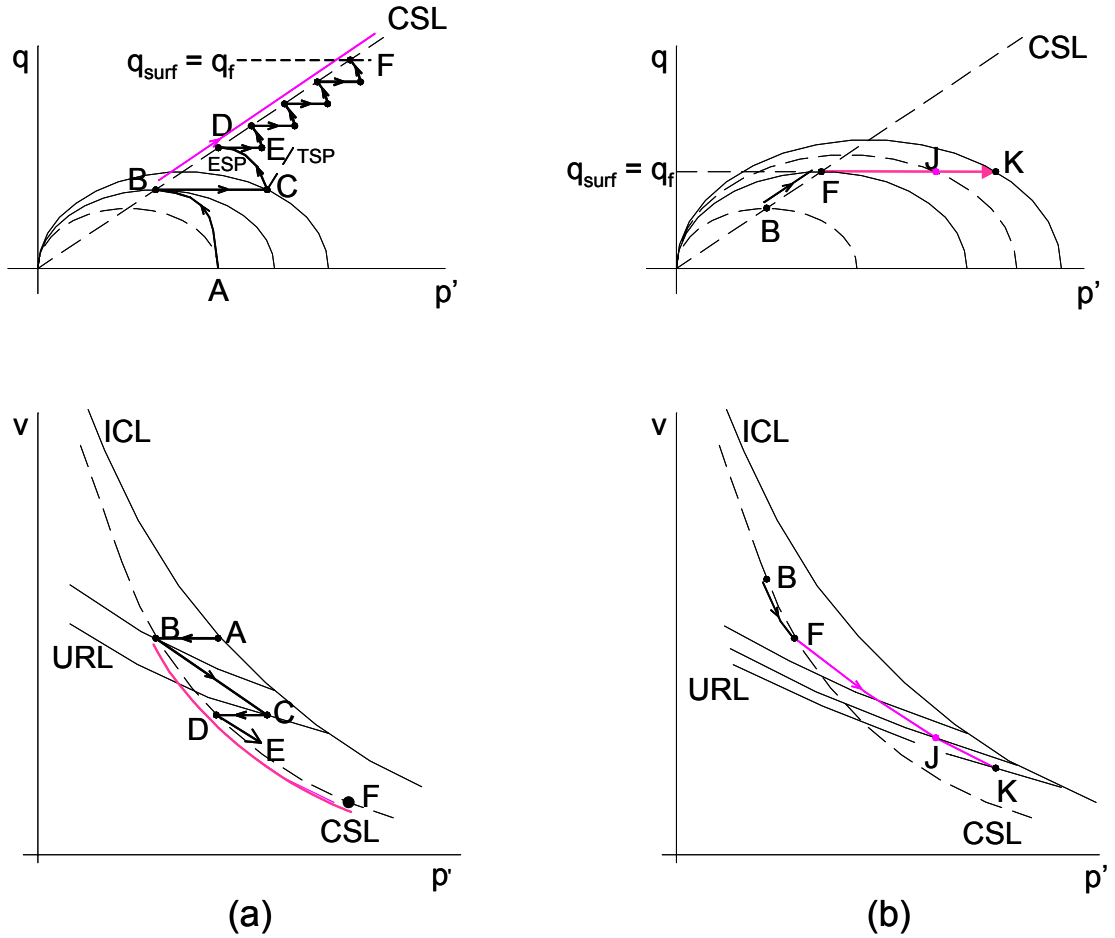

Fig 6.5: (a) Critical state consolidation; (b) Consolidation with constant shearing.

Let's consider a triaxial test being performed on a saturated till sample. The sample is first isotropically consolidated to an effective stress state indicated by point A in Fig 6.5. The sample is then subjected to conventional undrained triaxial shear stress (i.e. increasing deviatoric stress while holding the cell pressure constant). The drainage of

pore water in and out of the sample is computer-controlled. The sample is brought very close to critical state (failure) represented by point B in Fig 6.5. At this stage, the drainage valve is opened momentarily, thus allowing a fraction of the excess pore-water pressure generated in the sample to dissipate. The stress state of the sample moves away from the critical state line to a point C in Fig 6.5 and the sample gains a little bit of shear strength in the process. The drainage valve is closed again and the sample is once again brought close to failure (point D in Fig 6.5). Once again the drainage valve is opened momentarily and a fraction of excess pore-water pressure is allowed to dissipate. If this process is repeated in very small steps, the sample will appear to be undergoing consolidation while its stress state is close to critical state. In other words, it will consolidate along the critical state line in *q-p'-v* space. Such a consolidation is termed as critical state consolidation. It is envisaged that the zone of till where the available shear strength is less than the constant pervasive shear stress imposed by the overlying ice sheet, undergoes critical state consolidation. The profile of preconsolidation pressure (p'_o) for this zone can be obtained as follows:

Consider an infinitesimal square element of soil located at a depth z below the ground surface (Fig 6.6(a)). It is assumed that the state of normal stress within this element is isotropic and the magnitude of normal stress (σ') is given by the normal stress at the surface (σ'_{surf}) plus the overburden stress at depth z ($\gamma'.z$) where γ' is the effective (buoyant) unit weight of the till. It is plausible that the state of normal stress within this element could be anisotropic. However, the consideration of anisotropy of normal stresses will introduce another unknown variable in the model, resulting in an increase in the complexity of the model at the expense of revealing essential behaviour. Since the objective is to provide a qualitative assessment of the effect of subglacial shear on preconsolidation pressure profile, the assumption of isotropic normal stresses is justified.

In addition to the normal stress σ', a shear stress τ also acts on the four sides of the element (Fig 6.6(b)). Since the zone in which this element is located is at critical state, τ is equal to the shear strength of the soil at depth z (τ_f) that can be obtained by drawing a Mohr's stress circle for the element that is tangential to the Coulomb failure envelope (Fig 6.6(c)). From Fig 6.6(c), it can be seen that the major principal stress (σ'_1)

acting on the element is ($\sigma'+\tau$) and the minor principal stress (σ'_3) is (σ' - τ). Therefore, the mean effective pressure p' and the deviatoric stress q at a depth z are given by

$$p' = \sigma' - \frac{\tau}{3} \text{ and } q = 2\tau$$

For an incremental increase in depth δz, there will be an incremental increase in the normal stress $\delta\sigma'$ and a corresponding increase in the available shear strength $\delta\tau$. It can be shown that the corresponding increase in mean effective pressure ($\delta p'$) and deviatoric stress (δq) are given by

$$\delta p' = \delta\sigma' - \frac{\delta\tau}{3} \text{ and } \delta q = 2\delta\tau$$

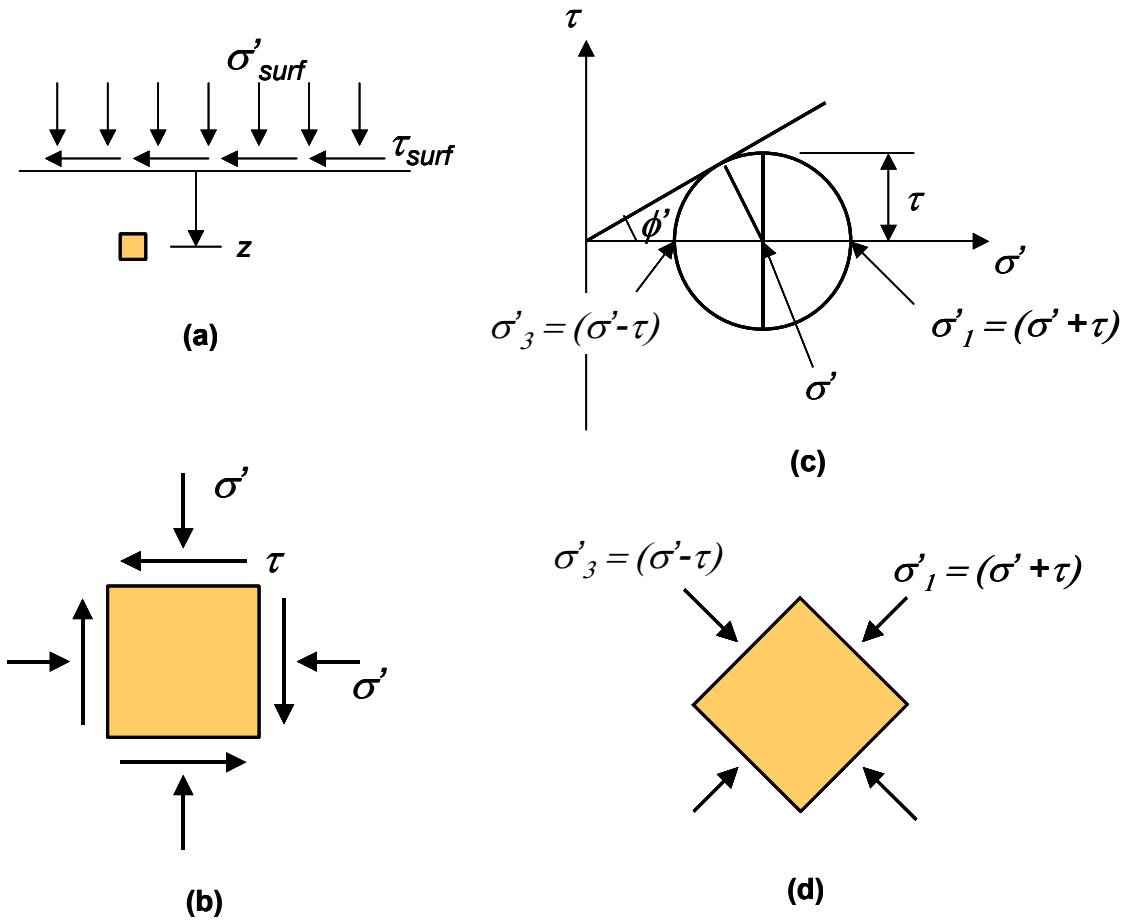

Fig 6.6 Stress state for an element of soil underneath the ice-sheet: (a) location of the element; (b) Stresses acting on the element; (c) Mohr's stress circle for the element; (d) orientation of principal stresses for the element.

Since $\delta q = M\delta p'$,

$$\delta\tau = (\frac{3M}{6+M})\delta\sigma'$$

and, therefore,

$$\delta p' = (\frac{6}{6+M})\delta\sigma' \tag{6.15a}$$

$$\delta q = (\frac{6M}{6+M})\delta\sigma' \tag{6.15b}$$

The increment of the preconsolidation pressure ($\delta p_0'$) can be expressed as

$$\delta p_0' = (\frac{12}{6+M})\delta\sigma' \tag{6.15c}$$

Compared to isotropic consolidation, it can be seen that

$$(\delta p_0')_{CSC} > (\delta p_0')_{IC}$$

where subscripts CSC and IC denote critical state consolidation and isotropic consolidation, respectively.

Consolidation with Constant Shearing

At a certain depth below the top surface of the till, the available shear strength (τ_f) equals the constant pervasive shear stress (τ_{surf}) imposed by the overlying ice sheet. Beyond this depth, the effective stress path moves away from the critical state line at a constant deviatoric stress q_{surf} corresponding to τ_{surf}. As consolidation progresses, the mean effective stress p' within the till increases but the deviatoric stress q_{surf} remains constant (path F-J-K in Fig 6.5(b)). Therefore, at the stress state denoted by point F, p' and q are given by

$$p_F' = \sigma_F' - \frac{\tau_{surf}}{3} = (\frac{6}{6+M})\sigma_F'$$

$$q_F = 2\tau_{surf} = (\frac{6M}{6+M})\sigma_F'$$

$$(p_0')_F = (\frac{12}{6+M})\sigma_F'$$

where subscript F denotes stress state parameters at point F.

At any stress state between points F and K, say at point J, *p'* and *q* are given by

$$p'_J = \sigma'_J - \frac{\tau_{surf}}{3} = (\sigma'_F + \delta\sigma') - \frac{\tau_{surf}}{3} = p'_F + \delta\sigma' = (\frac{6}{6+M})\sigma'_F + \delta\sigma'$$

$$q_J = 2\tau_{surf} = (\frac{6M}{6+M})\sigma'_F$$

$$(p'_0)_J = (1 + \frac{\eta_J^2}{M^2})p'_J$$

where η_J is the stress ratio (*q/p'*) at point J.

Therefore,

$$\delta p' = p'_J - p'_F = \delta\sigma' \tag{6.16a}$$

$$\delta q = 0 \tag{6.16b}$$

$$\delta p'_0 = (p'_0)_J - (p'_0)_F = \left[1 - \frac{6\sigma'_F}{6\sigma'_F + (6+M)\delta\sigma'}\right]\delta\sigma' \tag{6.16c}$$

Compared to isotropic consolidation, it can be expected that

$$(\delta p'_0)_{CQC} < (\delta p'_0)_{IC}$$

where subscript CQC represents constant shear consolidation. As $\delta\sigma'$ increases, $(\delta p'_0)_{CQC}$ approaches towards $(\delta p'_0)_{IC}$.

Softening due to subglacial shearing

Soil ("glaciotectonite"), near the tongue of an advancing glacier, may be subjected to intense shear. This is usually associated with the proglacial deformation process (Eybergen, 1987; Hart and Boulton, 1991). This process exhibits much shorter duration and much greater shear action when compared to the subglacial deformation process. In soil mechanics, it is well known that shear causes softening in heavily overconsolidated soils. Sauer et al. (1990) observed the softening of overconsolidated Cretaceous clays by glacial erosion. Fig 6.7 shows the effective stress path (ESP) of a heavily overconsolidated sample in undrained triaxial compression test. Before the ESP touches the current yield locus, no elastic/plastic volumetric strains are generated. When the ESP reaches the current yield locus, yielding and plastic volumetric strains occur and the

yield locus contracts until the ESP ultimately reaches the critical state line. After yielding, the shape of the ESP, determined by the material properties, is expressed as:

$$\frac{p'_i}{p'} = \left(\frac{M^2 + \eta^2}{M^2 + \eta_i^2} \right)^{\Lambda} \tag{6.17a}$$

where

$$\Lambda = \frac{\lambda - \kappa}{\lambda} \tag{6.17b}$$

and p'_i and η_i define an initial effective stress state. The "updated" preconsolidation pressure can then be given by:

$$p'_0 = p'_i \Big/ \left(\frac{2M^2}{M^2 + \eta_i^2} \right)^{\Lambda} \tag{6.17c}$$

It should be noted that softening occurs when shear is strong enough so that the ESP is able to reach the yield locus. As "old" soil (assumed heavily overconsolidated) is subjected to intensive shearing, the threshold value (τ_T) that results in yielding can be expressed as the positive root of the following equation:

$$\left(\frac{M^2 + 36}{9M^2} \right) \tau_T^2 + \left(\frac{p'_0 - 2\sigma'}{3} \right) \tau_T + \left(\sigma'^2 - p'_0 \sigma' \right) = 0 \tag{6.18}$$

The derivation of Equation 6.18 is given in Appendix B.

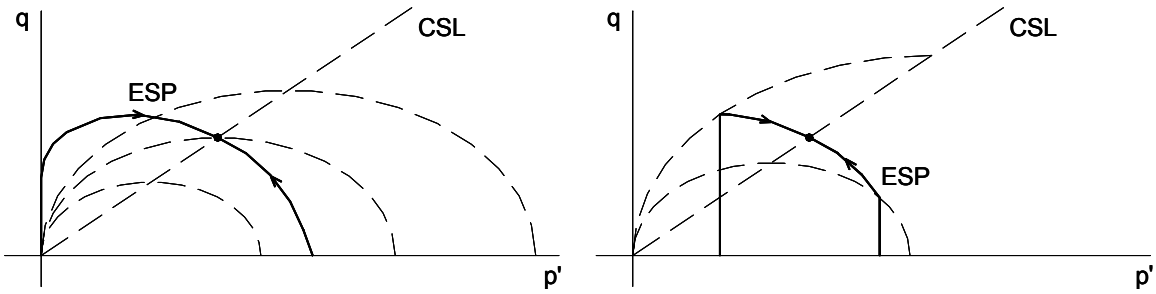

Fig 6.7: Subglacial shear softening.

6.5.4 U_e – t relationships

As mentioned above, the realistic K_0-consolidation has been replaced by the idealized isotropic consolidation, i.e. the compressibility is related to p' rather than σ'. This is generally adopted in soil mechanics modelling. Therefore, referring to Fig 6.8, a_v *and* a_s – the coefficients of compressibility for virgin compression and unloading-reloading, respectively – can be expressed as:

For Normal Compression Line (NCL): $$-\frac{\delta e}{\delta p'} = \frac{\lambda}{p'} = a_v \tag{6.19a}$$

For Unloading-Reloading Line (URL): $$-\frac{\delta e}{\delta p'} = \frac{\kappa}{p'} = a_s \tag{6.19b}$$

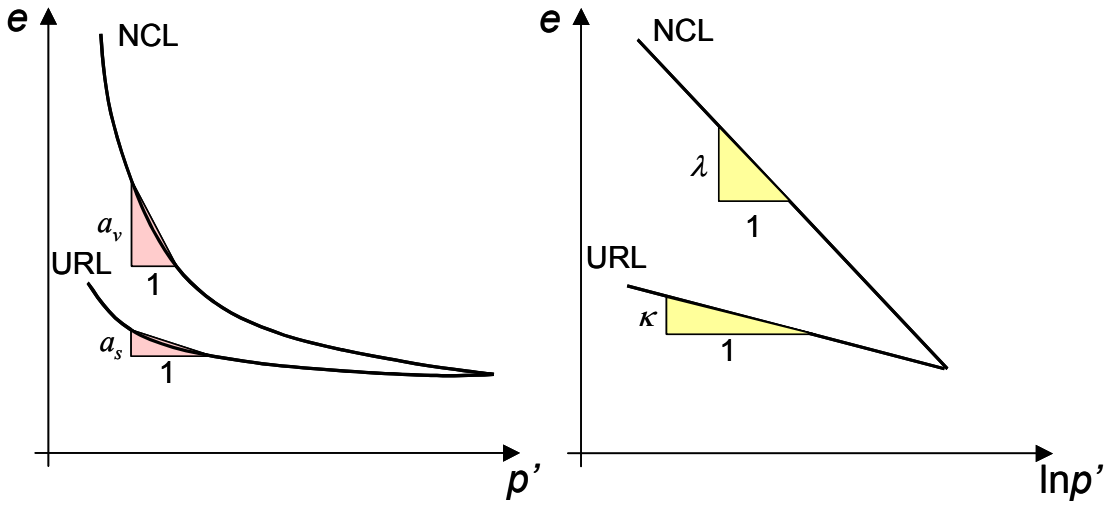

Fig 6.8 Normal Compression Line (NCL) and Unload-Reload Line (URL) in *e-p' and e*-ln*p'* space

It should be noted that consolidation is a process where the shear strength of soil gradually increases as the excess pore pressure dissipates. Therefore, it is possible that a soil element consolidates along the CSL at the beginning and subsequently leaves the CSL, consolidating with a constant shear stress. These correspond to the following two cases:

Critical state consolidation:

As mentioned previously, for the critical state consolidation to occur, $\tau_f \leq \tau_{surf}$. The CSL is parallel to the NCL (e.g. Wood, 1992) and is expressed as:

$$v_{cs} = \Gamma - \lambda \ln p'_{cs}$$

where subscript *cs* denotes critical state. Thus,

$$\frac{\partial v}{\partial \sigma'} = -(\frac{\lambda}{p'})\frac{\partial p'}{\partial \sigma'} \tag{6.20}$$

Combined with equations (6.19) and (6.20) and $v = 1+e$, the stress-strain relation is given by:

$$\frac{\partial e}{\partial \sigma'} = -a_v(\frac{6}{6+M}) \tag{6.21}$$

Substituting equation (6.21) into the continuity equation (6.3) gives:

$$\frac{k(1+e)}{\gamma_w}\frac{\partial^2 u_e}{\partial z^2} = -a_v(\frac{6}{6+M})\frac{\partial \sigma'}{\partial t} \tag{6.22a}$$

Equation (6.22a) can be further modified as:

$$c_v \frac{\partial^2 u_e}{\partial z^2} = (\frac{6}{6+M})(\frac{\partial u_e}{\partial t} - \frac{\partial \sigma}{\partial t}) \tag{6.22b}$$

where c_v is the coefficient of consolidation. Equation (6.22b) is the governing equation for critical state consolidation.

Consolidation with constant shearing:

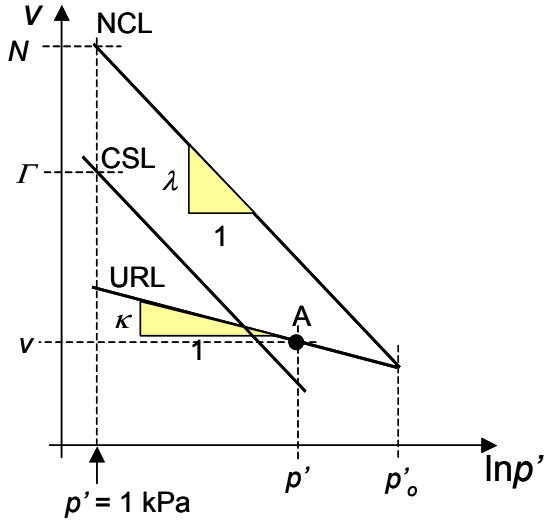

Fig 6.9 Relative locations of normal compression line, critical state line and unloading-reloading line in *v*-ln*p'* space

Referring to Fig 6.9, the specific volume of a point A on unloading-reloading line is given by

$$v = N + (\kappa - \lambda)\ln p'_0 - \kappa \ln p'$$

where N is the specific volume of a point on normal compression line corresponding to p' = 1 kPa. Thus,

$$\frac{\partial v}{\partial \sigma'} = (\frac{\kappa - \lambda}{p'_0})\frac{\partial p'_0}{\partial \sigma'} - (\frac{\kappa}{p'})\frac{\partial p'}{\partial \sigma'} \tag{6.23}$$

This equation can be transformed and reorganized as:

$$\frac{\partial e}{\partial \sigma'} = a_s(\frac{-2\eta^2}{M^2 + \eta^2}) - a_v(\frac{M^2 - \eta^2}{M^2 + \eta^2}) \tag{6.24}$$

The derivations of Equations 6.23 and 6.24 are given in Appendix C. Combining Equation (6.24) with Equation (6.3) (continuity equation) gives:

$$\frac{k(1+e)}{\gamma_w}\frac{\partial^2 u_e}{\partial z^2} = \left[a_s(\frac{-2\eta}{M^2 + \eta^2}) - a_v(\frac{M^2 - \eta^2}{M^2 + \eta^2}) \right]\frac{\partial \sigma'}{\partial t} \tag{6.25a}$$

Equation (6.25(a)) can be further modified as:

$$\frac{\partial^2 u_e}{\partial z^2} = \left[(\frac{1}{c_s})(\frac{-2\eta}{M^2 + \eta^2}) + (\frac{1}{c_v})(\frac{M^2 - \eta^2}{M^2 + \eta^2}) \right](\frac{\partial u_e}{\partial t} - \frac{\partial \sigma}{\partial t}) \tag{6.25b}$$

This nonlinear Laplace equation is the governing equation for consolidation with constant shearing. As η approaches zero, it reduces to Equation (6.4).

6.6 Model predictions

6.6.1 p'_0 profile

It is clear that there is a strong coupling between the dynamics of an ice sheet and sediment deformation beneath it. The main objective of the proposed model is to predict the p'_0 patterns formed within the subglacial environment. For this purpose, reasonable values of the basal shear stress and effective pressure must be chosen. It has been sufficiently demonstrated that the effective pressure in the soil at the base of the glacier is unlikely to be equal to the weight of the overriding ice because of the presence of a

phreatic surface within the glacier (Sauer et al., 1993). Boulton (1996) has shown that the effective vertical pressure beneath more than 1000 m thick ice-sheet ranged from 100 to 250 kPa which is the same order of magnitude as reported by other researchers (Fountain, 1994; Engelhardt et al., 1990). Therefore, for subsequent analysis, the value of effective pressure will be kept between 100 and 250 kPa. The basal shear stress is determined by the ice-sheet profile, which is generally assumed to have a parabolic form. The basal shear stress between 50 and 120 kPa can extend more than 500 km horizontally behind the toe of the glacier beneath a 1000 to 2000 m thick ice-sheet profile (Hart, 1995). Estimation between 80 to 120 kPa can be considered reasonable regarding the relative location of Saskatchewan during the Ice Age. The values of M and ρ (bulk) are assumed to be equal to 0.9 and 1990 kg/m^3, respectively.

Fig 6.10 shows the p_0' profile obtained using isotropic consolidation and coupled shearing model. Compared with the isotropic consolidation process, the p_0' value at the top of the sediment produced by the coupled shearing model is significantly higher (almost approaching two times). This is due to the effect of shear action and can be straightforwardly represented in the $p' - q$ plane (Fig 6.11; Note that $p' \approx \sigma'$).

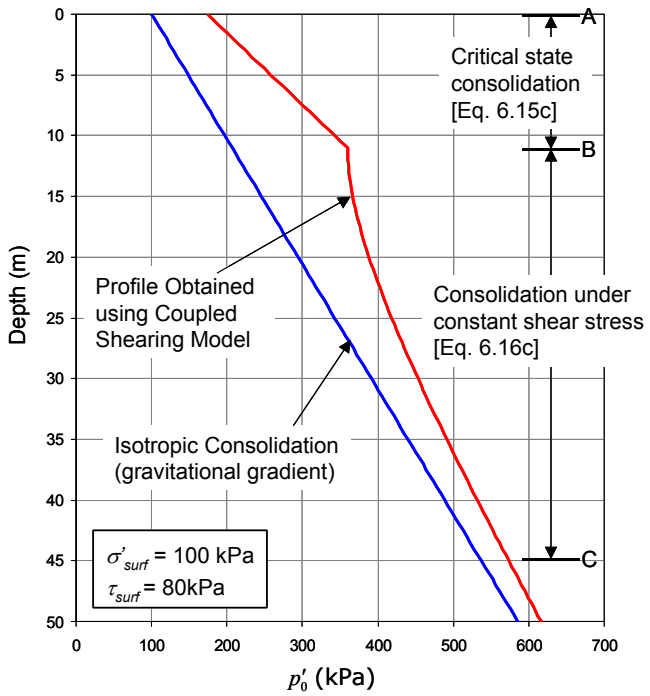

Fig 6.10 p'$_0$ profiles for isotropic, constant shear and critical state consolidation

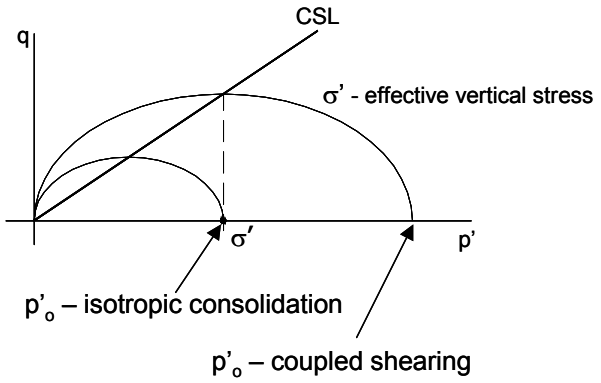

Fig 6.11 Starting points of the p'_0 profiles of the two models

Obviously, the p'_0 profile for isotropic consolidation arising purely from the weight of the overlying sediment follows the gravitational line as shown in Fig 6.10. Compared with the gravitational gradient, the p'_0 gradient (zone AB in Fig 6.10) that is related to critical state consolidation is much greater, i.e. the p'_0 value increases much more rapidly with depth. As a result, under the condition of 100 kPa effective surface pressure and 80 kPa basal shear stress (Fig 6.10), the p'_0 value due to critical state consolidation ranges from 170 to 360 kPa compared with 100 to 210 kPa for isotropic consolidation. The p'_0 gradient for critical state consolidation can be obtained by introducing $\delta\sigma'/\delta z = \rho' \cdot g = \gamma'$ where ρ' is the effective (buoyant) density and g is the Earth's gravitational acceleration (9.81 m/s^2). Rewriting Equation 6.15c as:

$$\delta p'_0 = (\frac{12}{6+M})\delta\sigma' = (\frac{12}{6+M})\gamma'\delta z$$

or

$$(\delta p'_0/\delta z) = (\frac{12}{6+M})\gamma' \qquad (6.26)$$

As mentioned above, the basal shear stress applied by the ice-sheet provides an upper limit (threshold) for the depth up to where critical state consolidation can occur. Eventually the sediment begins to consolidate under a constant shear force (zone BC in Fig 6.10). The p'_0 gradient which is related to constant shear action is much milder compared with the gravitational gradient. In fact it is almost close to vertical near the top

of zone BC. Beyond zone BC, the influence of subglacial shearing tends to disappear and the p_0' gradient approaches the gravitational gradient. This is predicted by Equation 6.16c (as $\delta\sigma' \uparrow, \delta p_0' \rightarrow \delta\sigma'$). Similar to Equation (6.26) above, the p_0' gradient profile can also be quantified by rewriting Equation 6.16c as:

$$= \left[1 \quad \frac{}{M)\gamma'\delta z}\right]\gamma'\delta z$$

or,

$$\left(\quad /\delta z\right) \qquad \frac{6\sigma'}{(6+M)\gamma'\delta z}\Bigg]\gamma' \qquad (6.27)$$

However, the above equation cannot be used directly to draw the p_0' gradient profile since it is related to the chosen increment of the depth. The p_0' gradient profile was then formed by dividing the p_0' increment by the depth increment.

Because of the characteristic of rapid increase of the p_0' value due to critical state consolidation, the zone where critical state consolidation occurs is usually very thin or it even completely disappears (see subsequent discussion). If we consider effects of the post-glaciation processes, for instance, erosion and one-dimensional consolidation, this zone is likely to be completely wiped off. Therefore, within the zone BC with thickness of 25 m under the condition of 100 kPa effective surface pressure and 80 kPa basal shear stress (Fig 6.10), the proposed model predicts that the p_0' value we measured today is between 360 and 480 kPa, compared with 200 to 425 kPa using traditional 1-D consolidation theory.

Effect of Basal Shear Stress

The effect of basal shear force is examined by assuming a constant effective surface pressure of 150 kPa while changing the basal shear stress from 80 to 120 kPa. As shown in Fig 6.12, as the basal shear stress increases from 80 to 120 kPa, the depth where critical state consolidation takes place significantly increases from 6 m to 16.5 m whilst

the p_0' value at the bottom of the critical state consolidation zone increases from 360 kPa to 540 kPa. These results predicted by the proposed model can be explained as follows.

The point separating the critical state consolidation zone from the constant shear consolidation zone in the p_0' profile represents a threshold where the shear strength of the soil element is just enough to bear the basal shear stress applied by the ice-sheet. The shear strength is obviously determined by the effective stress that increases with depth, that is, the weight of the overlying sediment. Therefore, at higher basal shear stress, the "failure" zone extends to greater depths (see also Fig 6.4).

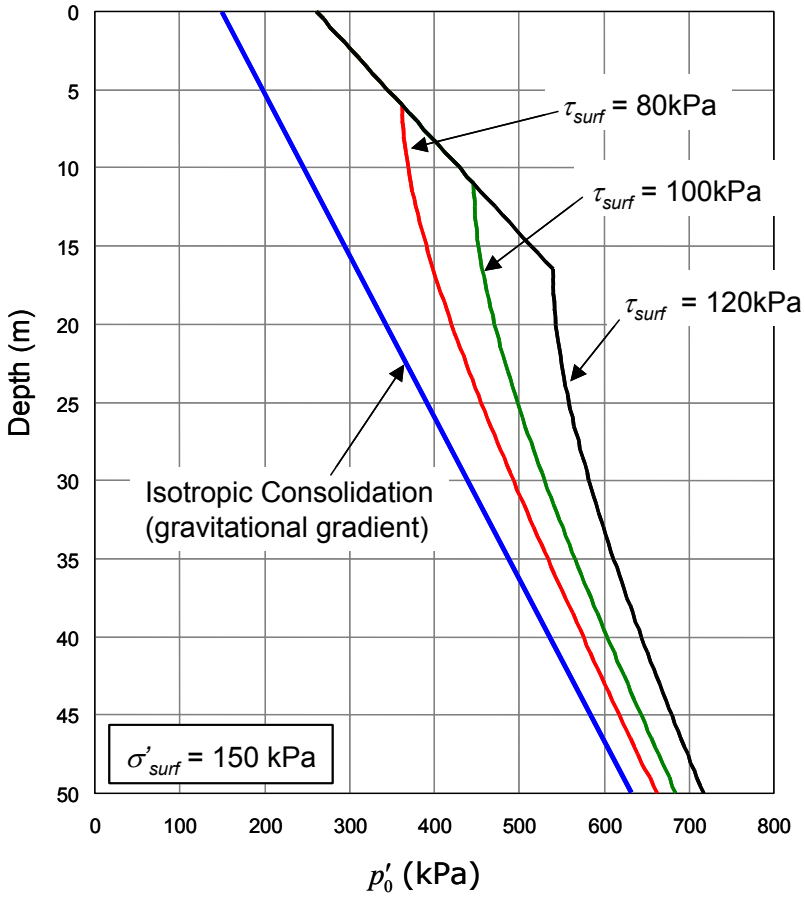

Fig 6.12 Effect of basal shear stress

Effect of Basal Normal Effective Pressure

The effect of basal normal effective pressure is examined by assuming a constant basal shear stress of 80 kPa while changing the effective surface pressure from 100 to 200 kPa. As shown in Fig 6.13, as the basal normal effective pressure increases from 100 kPa to

200 kPa, the depth where critical state consolidation takes place significantly decreases from 11 to 0.5 m whilst the p_0' value at the bottom of the critical state consolidation zone shows a small increase from 350 kPa to 370 kPa. At higher basal normal effective pressures, constant shear stress consolidation occurs for almost the entire depth of the soil layer.

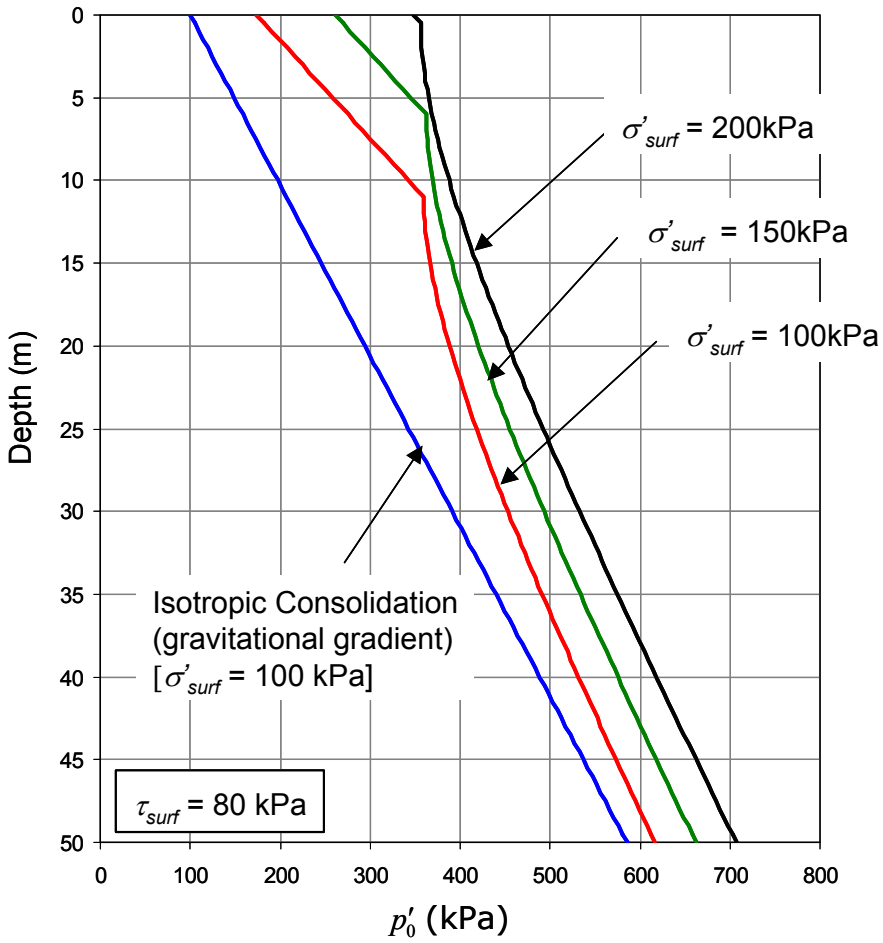

Fig 6.13 Effect of basal normal effective stress

6.6.2 U_e - t relationship

Consolidation is always accompanied with the drainage of pore water in the soil skeleton. This process is usually presented as the U_e - t relationship. Mainly, there are two objectives for conducting this part of numerical analysis: Firstly, studying the theoretical difference of the U_e - t relation predicted by the proposed model and the traditional one-dimensional consolidation theory; secondly (and more importantly), examining the

continuity condition. In the proposed model, there are two partial differential equations (Equations 6.22 and 6.25) governing the U_e - t relationship. A consolidation process may proceed in such way: the soil element consolidates along the CSL at the beginning; its shear strength grows as the normal effective stress increases; eventually the strength exceeds the maximum shear stress applied so that the soil element consolidates under constant shear stress condition. Obviously, during the earlier stage, the consolidation is governed by Equation (6.22) whereas, during the latter stage, it is governed by Equation (6.25). However, it should be noted that for a homogeneous soil with a constant permeability and compressibility, the gradient of total head within the soil mass must satisfy the continuity condition during the whole consolidation process (Lambe and Whitman, 1979). This provides a means for validating the theoretical reasonability of the proposed model. For the convenience of comparison, the output of the proposed model will be evaluated based on an example shown in Fig 6.14. A student version of FlexPDE software (PDE Solutions Inc, 2005) was used for this purpose. The results of the modelling are described below.

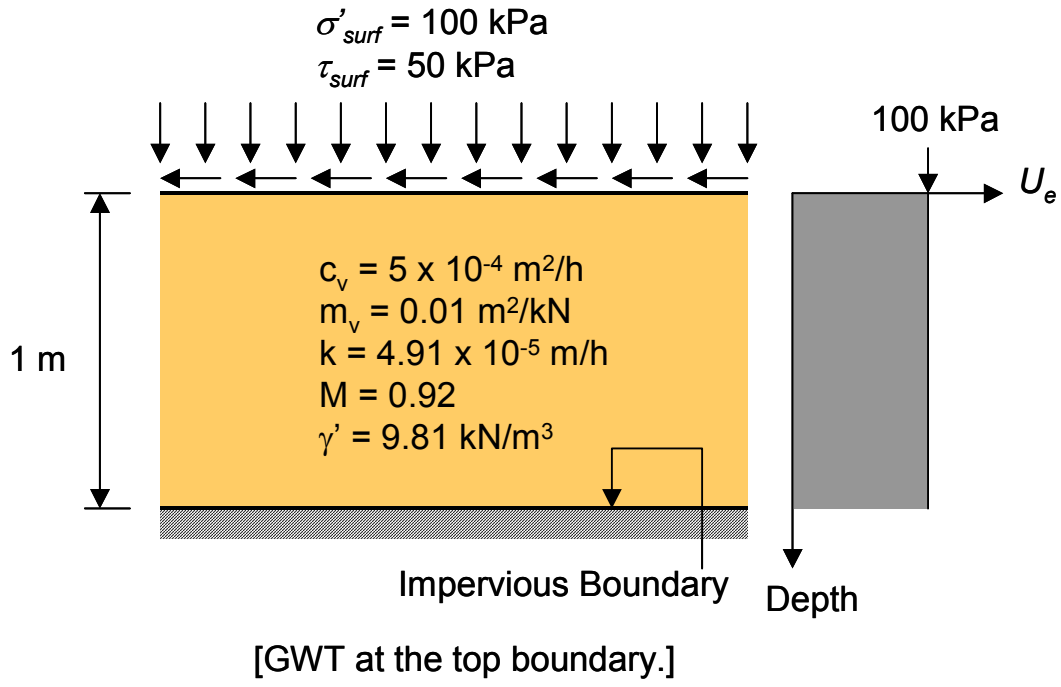

Fig 6.14 Example chosen to confirm U_e – t relationship

Critical state consolidation or consolidation with constant shearing individually has little effect on the dissipation of excess pore water pressure (Fig 6.15 and Fig 6.17) although the magnitudes of p_0' are quite different due to the consideration of shear action (Fig 6.16 and Fig 6.18). Real coupling of consolidation and shear (Fig 6.19) shows that consolidation along CSL and constant shearing can take place related to temporal and spatial variations. Referring to Fig 6.19, the lower 0.4 m of the soil layer undergoes critical state consolidation because the applied shear stress is greater than the shear strength of the material. The upper 0.6 m of the soil layer undergoes consolidation under constant shear stress as it has experienced a gain in shear strength due to dissipation of excess pore-water pressure. It can also be seen from Fig 6.19 that the excess pore pressure gradient satisfies the continuity condition.

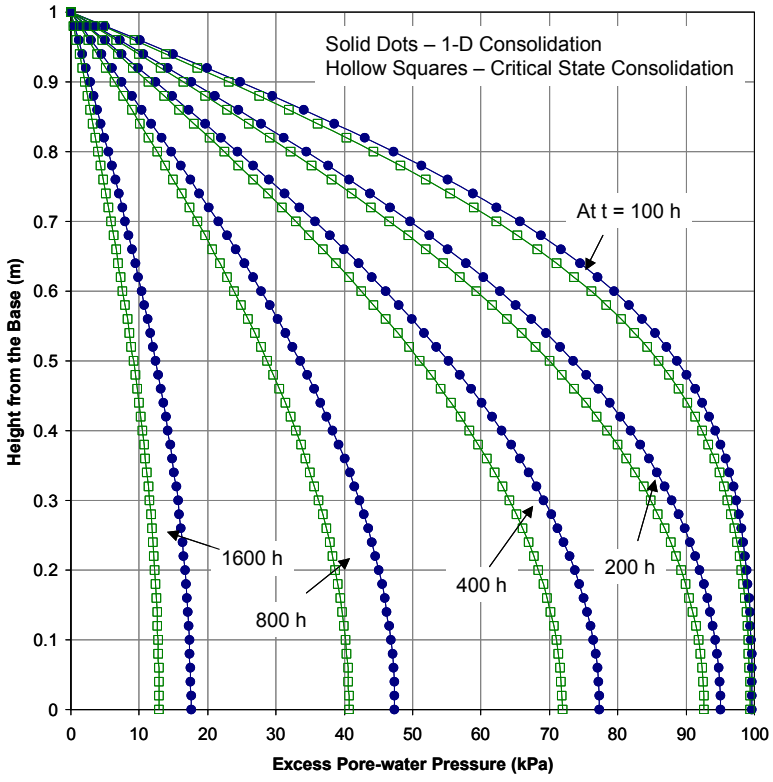

Fig 6.15 1-D vs. critical state consolidation – Dissipation of excess pore-water pressure

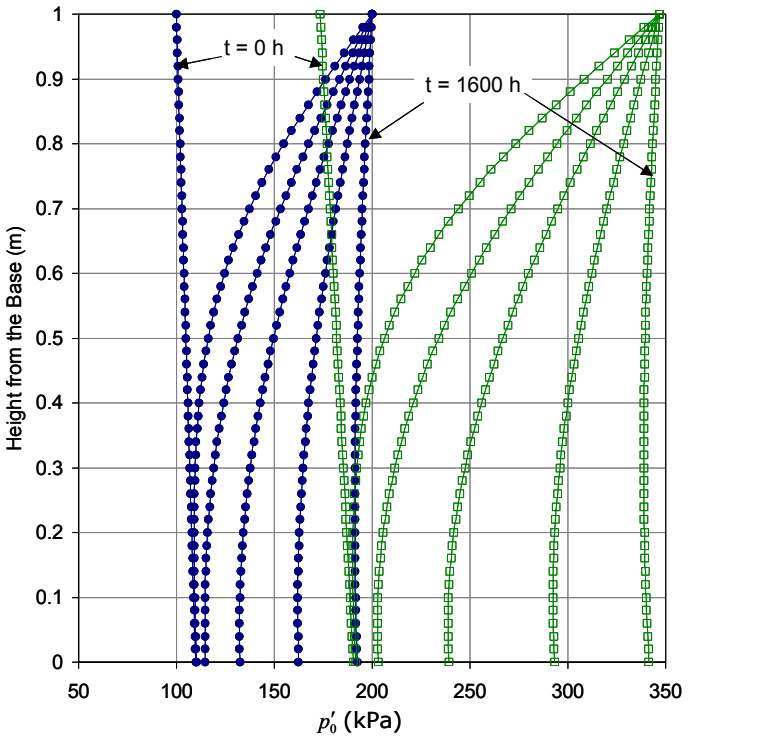

Fig 6.16 1-D vs. critical state consolidation – p'_0 distribution

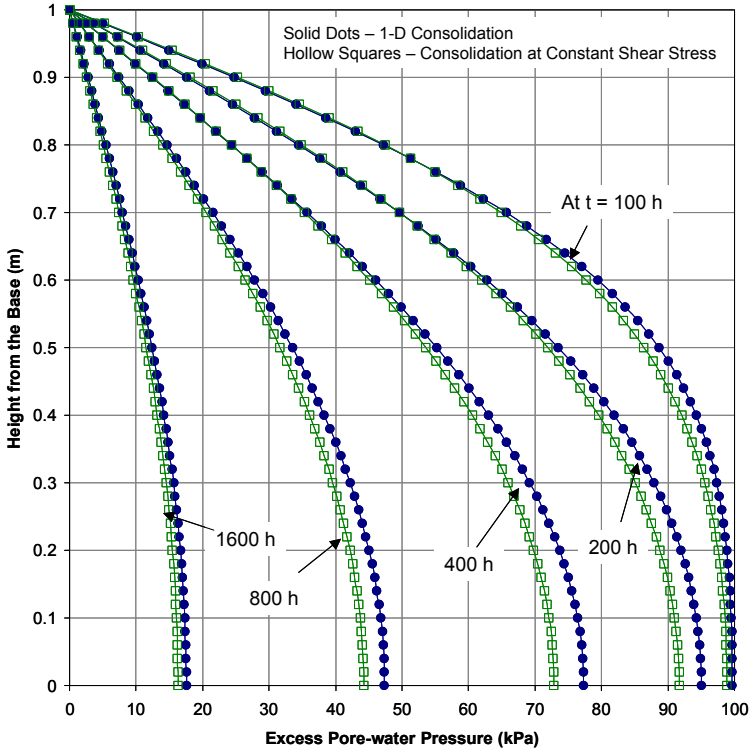

Fig 6.17 1-D vs. constant shear stress consolidation – Dissipation of excess pore-water pressure

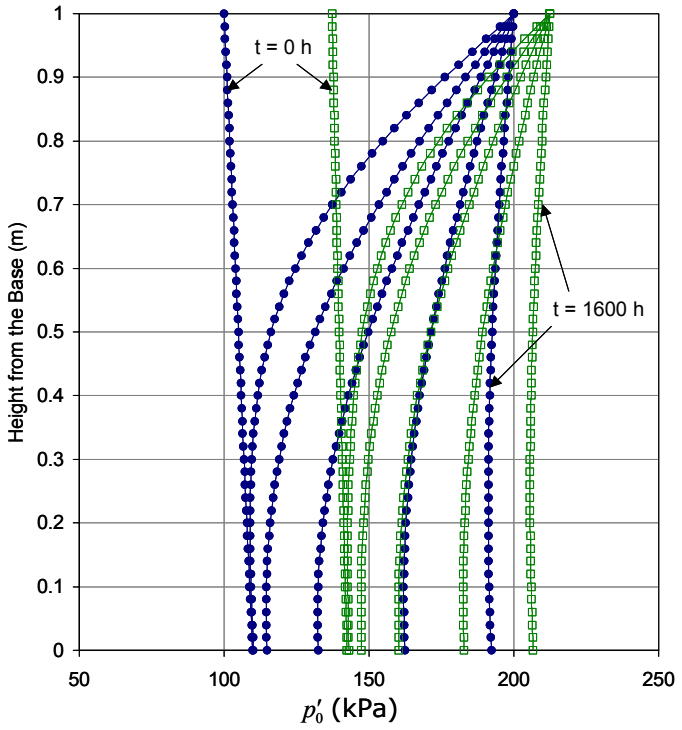

[Solid Dots – 1-D Consolidation; Hollow Squares – Consolidation at Constant Shear Stress]

Fig 6.18 1-D vs. constant shear stress consolidation – p'_o distribution

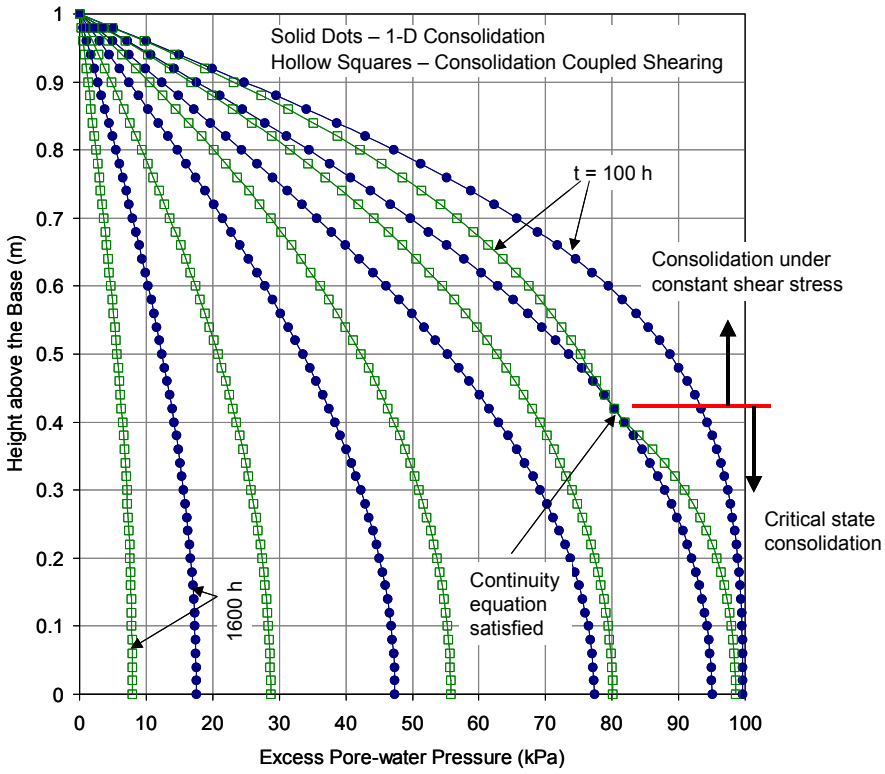

Fig 6.19 Consolidation coupled with shearing – confirmation of continuity condition

6.6.3 Subglacial shear softening

Pro-glacial shearing during glacial advance can result in significantly lowered p_0' values within heavily overconsolidated sediments. These phenomena are not rare in engineering practice (e.g. Sauer et al., 1990). Since little research has been done on the pro-glacial environment, only a "quick" simulation is presented here.

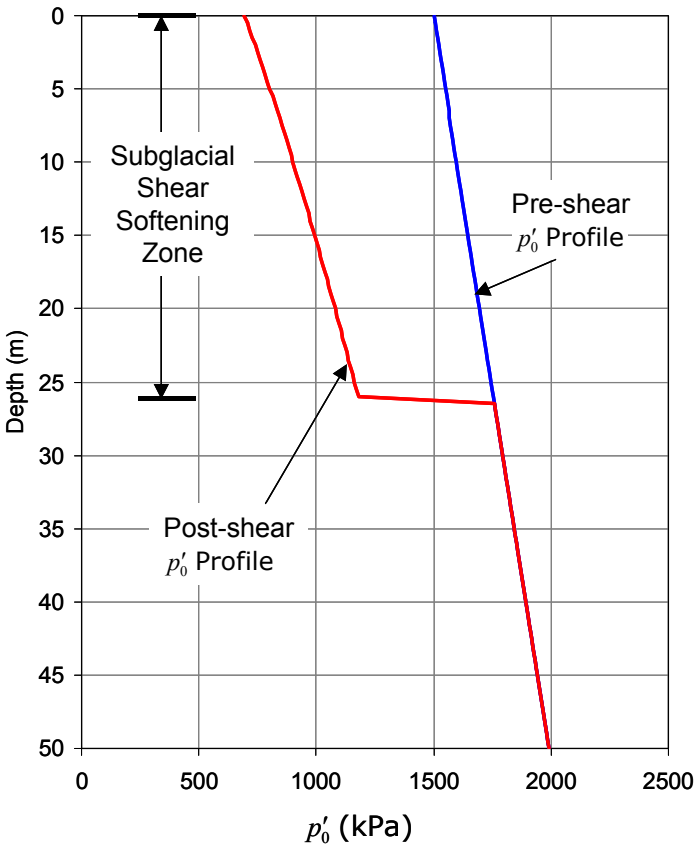

Fig 6.20 Subglacial shear softening zone predicted by coupled consolidation-shear model

As mentioned in Section 6.5.3, pro-glacial deformation is usually characterized as much shorter duration and intensive shear action compared to the subglacial deformation. Therefore, it could be modeled as an undrained shearing process. The basal shear stress and effective surface pressure were assumed to be equal to 300 kPa and 150 kPa respectively. Sauer et al. (1993) found that the p_0' values in pre-Battleford tills along a transect 1300 km across Saskatchewan range from 1200 to 2300 kPa, with an average of 1800 ± 200 kPa. Therefore, it was assumed that the pre-glacial p_0' value at the pre-glaciated ground surface was equal to 1500 kPa and followed a gravitational gradient

along the depth. The following values were assumed for the model: $\lambda = 0.091$; $\kappa = 0.034$; $M = 0.92$ and bulk density $\rho = 1990$ kg/m^3. The coupled consolidation-shear model predicts that the p_0' value could be significantly reduced from 1500-1800 kPa to 750-1250 kPa due to the effect of shearing applied by the glacier (Fig 6.20).

6.7 Case study – Battleford Till at Birsay, Saskatchewan

The objectives for conducting this case study using the proposed model are:

(1) to demonstrate that the p_0' value observed in practice can be produced by a much lower effective pressure, and therefore, is compatible to the measurement of effective pressures and deformation forms reported by other authors, and
(2) to confirm that the p_0' profile along the depth can deviate from the gravitational profile and may plot very close to a vertical line.

The first model was constructed by simply assuming that the basal effective pressure is equal to 200 kPa, basal shear stress is equal to 110 kPa, M is equal to 0.9 and bulk density ρ is equal to 2020 kg/m^3. Based on the consideration of erosion, the top 7.5 m zone was removed. The p_0' profile formed by traditional one-dimensional consolidation arises from the weight of the overlying sediment. Therefore, it is represented as a gravitational line. As shown in Fig 6.21, the p_0' profile predicted by the proposed model is closer to the actual observation than that predicted by one-dimensional consolidation theory. Moreover, it must be noted that an implicit assumption has been introduced for the one-dimensional consolidation theories that the effective pressure at the bed of the ice-sheet was as high as 400 kPa. Glaciological and geological research suggested that this would unlikely take place. According to the prevailing subglacial shear deformation theory, the shear strength due to such a high subglacial effective pressure would be high enough to prevent the subglacial sediment from deformation. Therefore, subglacial erosion, transport and deposition processes that are essential to the formation of tills could not occur.

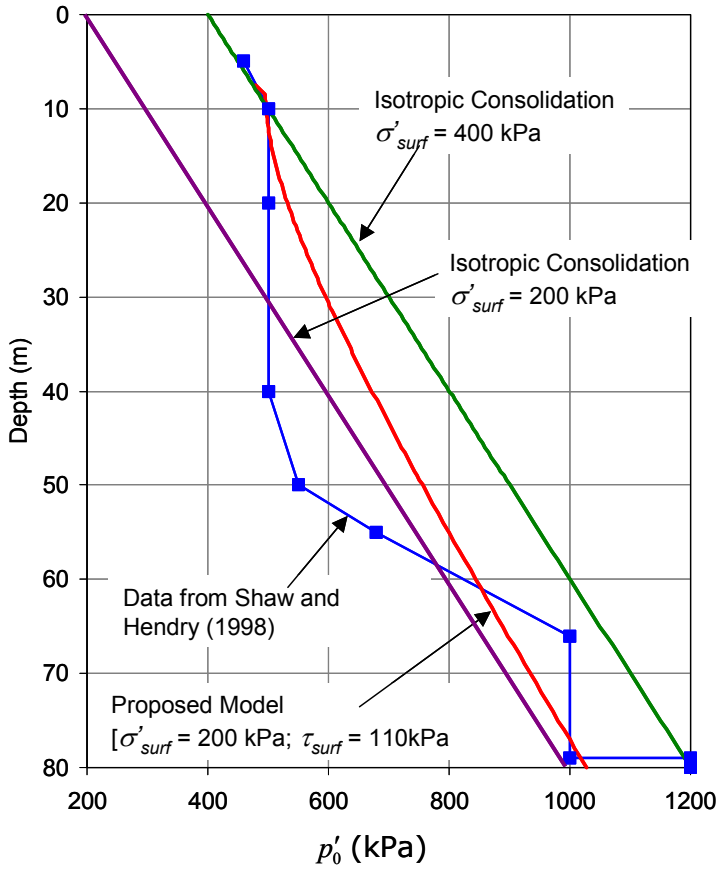

Fig 6.21 Comparison of measured and predicted values of p'_0 (without drainage considerations)

6.7.1 Effect of drainage conditions

For the convenience of disclosing the general effects imposed by the proposed model, the foregoing predictions do not consider the influence of drainage during the consolidation process. In fact, the formation process of tills involves a "drainage-consolidation" process (Section 2.3.5). This factor should be considered for the real case study.

As shown in Fig 6.22, a load increment on the sediment in a pressure cell sets up a potential pressure in the interstitial water. This causes water to flow out of the cell and permits grain packing to improve until the soil skeleton carries the entire additional load and the potential pressure has decayed to zero. Beneath a melting glacier, there is a continuous water flux into the sediment. Discharge from this water requires a permanent potential gradient. Thus, the effective pressure (load pressure minus water pressure) will be smaller than in the case of non-glacial consolidation beneath a similar load. The

effective pressure gradient underneath a glacier is then given by Equation (6.28) (Boulton and Dobbie, 1993; see Section 2.3.5).

$$\frac{\partial \sigma'}{\partial z} = \left(\frac{\partial \sigma'}{\partial z}\right)_g - \frac{\partial u_e}{\partial z} \tag{6.28}$$

The first term is the gravitational effective pressure gradient and is normally about 10 kPa/m (Boulton and Dobbie, 1993). The second term is due to the potential gradient generated by the flux through the sediment. Boulton and Dobbie (1993) further suggested $\partial\sigma'/\partial z \geq (\partial\sigma'/\partial z)_g$ ($\approx$ or >> depends on the permeability of aquitard) due to a "downward" drainage. However, Casagrande (1936) proposed that both "downward" and "upward" drainage could take place; especially the "upward" drainage should not be discounted in low permeabilty glaciated soils.

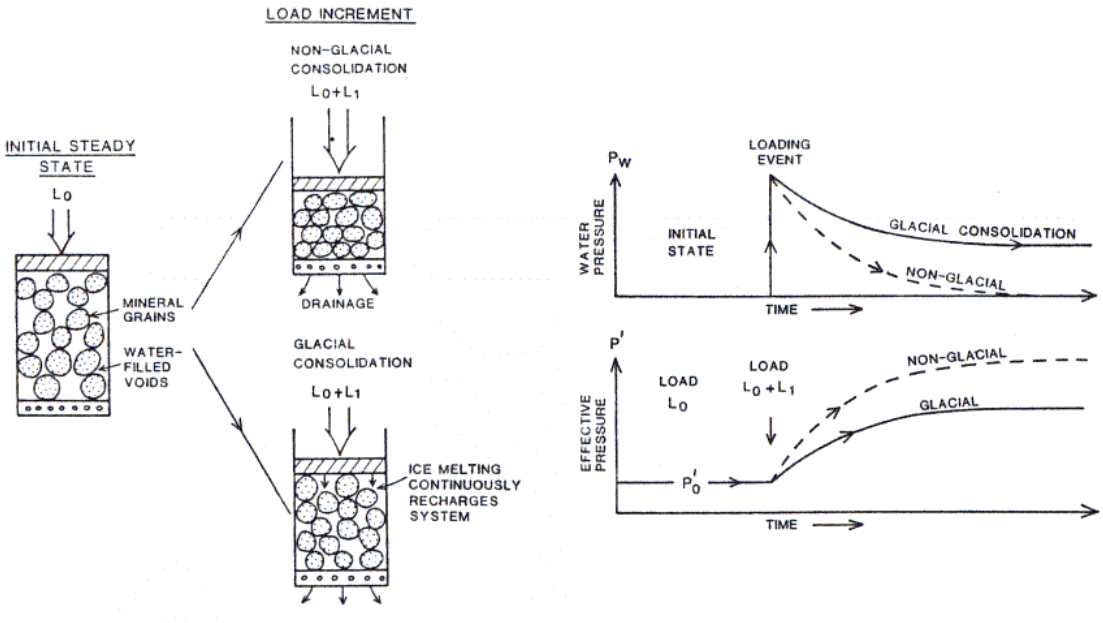

Fig 6.22 Glacial and non-glacial consolidation (After Boulton and Dobbie, 1993)

At Birsay, about 80 meters thickness of Battleford till unconformably overlies Cretaceous shale of the Bearpaw Formation. Shaw and Hendry (1998) reported that the *k* values within the Battleford till were between 2.7 $\times 10^{-11}$ and 5.4 $\times$ 10^{-11} m/s and were about one order lower for the underlying Cretaceous shale. In the Saskatchewan area, many tailings piles with well-recorded piezometric data provide excellent cases for

studying the hydraulic response of glaciated soils to the superimposed loads. The footprint area of a typical pile is usually around 10 km^2, and the height is between 30 m and 80 m. The stratigraphic sequence (from top downward) generally consists of surficial stratified drifts and glacial tills overlying Cretaceous shale. It has been observed that the piezometer data from several tailings pile sites in Saskatchewan collected over a span of more than 10 years shows a freshwater total head within the Cretaceous shale that is consistently greater than that at the bottom of the pile (Haug, 2005). This suggests that an "upward" drainage exists below the salt tailings and implies that the identical drainage conditions may have prevailed during the past glaciations.

A second model simulation was conducted by assuming that an "upward" drainage exists during the formation process of Battleford till. The potential gradient ($\partial\sigma'/\partial z$) of 4.9 kPa/m was used in the model. This value is equivalent to a freshwater head within the Cretaceous shale layer that is 40 m higher than that at the bottom of the tailings pile. Since the drainage follows the Darcy's law, the flux rate (m) can be expressed as

$$m = \left(\frac{-k}{\rho_w g}\frac{\partial u_e}{\partial z}\right) \tag{6.29}$$

If the k value within the Battleford till is equal to 4×10^{-11} m/s, this assumption means that an "upward" flux at a rate of 1.6×10^{-9} m/s occurs. The gravitational gradient was simply assumed to be equal to 10 kPa/m (equivalent to bulk density of 2020 kg/m^3). The outputs of the model are presented in Fig 6.23. The p_0' profile predicted by the proposed model is very close to a vertical line. The p_0' profile predicted by the one-dimensional consolidation theory even after the consideration of upward drainage continues to deviate significantly from the "vertical" pattern. The value of the effective pressure at the base of the glacier that is consistent with this one-dimensional consolidation profile is likely unreasonable. It can also be seen from Fig 6.23 that the predictions of p_0' values from the proposed model are close to the observed p_0' values only in the top 50 m of the layer. It is worth noting that the pattern of steeply increasing p_0' values followed by

nearly constant p_0' values is repeated beyond 50 m depth. A thickness of 80 m for the Battleford till is not common in Saskatchewan. It may be possible that the bottom 30 m of the layer was deposited by the previous glaciation.

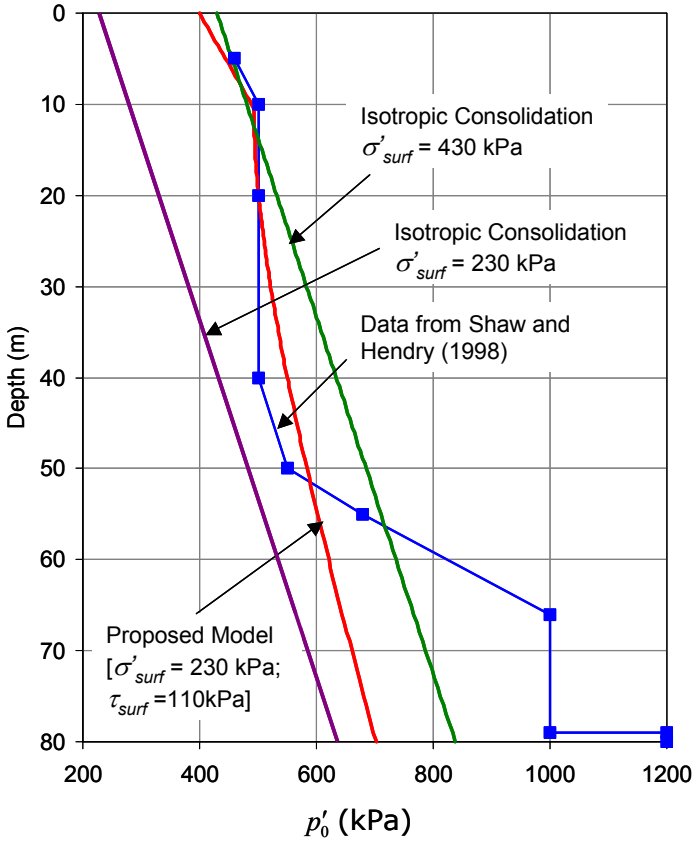

Fig 6.23 Measured and predicted p'_0 profiles (upward drainage considered)

6.8 Summary

It is generally observed that the patterns of p_0' do not follow the gravitational gradient, but much closer to vertical with depth; and the magnitude p_0' is not compatible with the measured effective pressure value at the bed of the glacier. So far, all the theories suggested by other authors are significantly dependent on the boundary conditions. The model proposed in this thesis provides another explanation for these phenomena by taking subglacial shear action into account. The proposed model does not exclude the effects of specific boundary conditions. In fact, the potential water pressure gradient that is related to the specific boundary conditions and generally used by other researchers

(Sauer et al., 1993; Boulton and Dobbie, 1993) can also be easily included in this model if the environmental factors are definite.

The case study on the Battleford till at Birsay represented that a much more reasonable effective pressure could result in the observed p_0' magnitude by using the proposed model. The proposed model also predicted a p_0' profile much closer to the vertical profile than the gravitational gradient. More careful study suggested that a slight "upward" flux likely existed during the formation process of the Battleford till.

Chapter 7 Conclusions

7.1 Overview

In geotechnical practice, soils are generally assumed to be "cross-anisotropic", indicating that the geomechanical properties (e.g. stiffness, in situ stresses, permeability, etc.) in the horizontal plane are isotropic. This assumption is based on elasticity and one-dimensional consolidation theory. Unfortunately, this assumption is applied for soils that have been affected by processes other than one-dimensional consolidation and rebound, such as glaciated soils. Several models of deposition of glaciated soils that are based on one-dimensional consolidation have been suggested in the literature. These models depend significantly on the boundary conditions imposed and assume that glaciated soils reach their present (overconsolidated) state as a result of compression under the effective (or buoyant) weight of glacier ice followed by erosion. It has been observed that the preconsolidation pressure for glaciated soils is nearly constant with depth. Such patterns of preconsolidation pressure can be difficult to explain solely on the basis of one-dimensional consolidation theory. Several evidences exist that demonstrate that shear deformation is present beneath the ice sheets. It has also been reported that anisotropic horizontal stresses have likely occurred in glaciated soils as a result of subglacial shearing. Anisotropic lateral stresses also suggest that one-dimensional consolidation may not be the main process that resulted in the present stress state of these soils. None of these models of glacial deposition consider subglacial shearing and its effect on the formation of glaciated soils. Therefore, a need to examine the effect of subglacial shear stresses on the geomechnical properties of glaciated soils was identified. It was envisaged that by studying the mechanics of glaciation vis-à-vis measurements on glaciated soils, significant contributions could be made to our understanding of spatial distribution of soil properties leading to a reduction in uncertainty in geotechnical design of structures founded on glaciated soils. The main objectives of this research were to find evidence of anisotropic geomechanical properties (yield stress, stiffness and in situ

stress) and to explain the patterns of preconsolidation pressure observed in glaciated soils.

These objectives were achieved by first conducting an extensive review of published literature. Several theories of subglacial deformation and deposition were reviewed. In particular, the one-dimensional consolidation theory applied on glacial soils was discussed in detail so as to reveal its limitations in explaining the geomechanical behaviour of glaciated soils. A glaciated soil from the province of Saskatchewan, namely Battleford till, was selected for the experimental study. Conventional oedometer tests were conducted on vertical, horizontal and inclined samples of Battleford till to explore the anisotropy of yield stress. Anisotropy of stiffness was investigated using the newly developed lateral stress oedometer. Anisotropy of in situ stresses was examined by conducting field measurement of in situ stresses in a glaciolacustrine clay, namely Pot clay, from the Netherlands using a self-boring Load Cell Pressuremeter (LCPM). In order to explain the patterns of preconsolidation pressure observed in glaciated soils, a new glacial process model was developed in which the effects of consolidation were coupled with the effects of basal shear.

7.2 Key Findings

- Preliminary evidence of a correlation between the maximum stiffness in a horizontal plane and the known direction of glacial shear was observed, although the results show some scatter and more tests are needed on other glaciated soils in order to confirm this correlation.
- Conventional oedometer tests on directional Battleford till samples showed that the correlation between yield stress and known direction of glaciation was rather poor.
- The data of LCPM tests conducted on Pot clay suggested that the horizontal anisotropy of in situ stresses that is consistent with the direction of glacier advance likely does not exist.
- Using the proposed glacial process model that couples the effects of consolidation and basal shear, it was possible to obtain the patterns (both magnitude and profile) of preconsolidation pressure generally observed within a

subglacial deforming zone. The proposed glacial process model was combined with Casagrade's hypothesis to explain the diversity of the preconsolidation pressure patterns.

- The proposed glacial process model was used successfully to "predict" the preconsolidation pressure pattern of Battleford till at Birsay. It provided an outcome that was much closer to the practical observations than that provided by traditional one-dimensional consolidation theory. The model also suggested that a slight "upward" flux likely existed during the formation process of the Battleford till.

Given the rather limited scope of the research, the reader is advised to refrain from deriving general conclusions on the behaviour of glaciated soils. Clearly, more results (and their statistical interpretation) are needed in order to achieve a better understanding of the role of subglacial shear in imparting anisotropic geomechanical properties to glaciated soils.

7.3 Recommendations for Future Work

- True-anisotropy of soil properties has not been well understood so far. Rather than testing natural glaciated soils, it might be better to begin by conducting laboratory studies using remolded natural soils or ideal soils such as kaolin that are consolidated in the lab. The stress history and the properties of such soils can be controlled precisely, thus eliminating the uncertainty associated with using natural soils. It is worth noting that much of modern soil mechanics was developed in light of the studies using these ideal, remoulded soils.
- Geomechanical properties of natural soils are extremely sensitive to many factors such as sample disturbance and size limitations. Field tests (e.g. expansion self-boring pressuremeter tests, dilatometer tests, plate loading tests, etc) can eliminate some of these factors and provide more convincing results, especially when the data interpretation is based on statistical analysis.
- Studies of the microstructure of soils may also be useful as a means to analyze anisotropy. Actually, the fact that particles can develop specific fabric

arrangements as a response to bulk sediment strain driven by stresses at the base of a glacier has long been used to investigate the formation and deformation of sediments in structural geology.

- Innovative experimental techniques are necessary for the studies of anisotropy; the newly developed lateral stress oedometer ring is a good example. The possibility of developing a triaxial shear apparatus with non-contact radial deformation measurements using, for example laser transducers or digital imaging, should be explored. Such an apparatus would be capable of subjecting glaciated soils to a wide variety of stress paths in the principal stress space and therefore, it would be extremely useful in the characterization of the three-dimensional yield surface (state boundary surface) for these soils.
- Salt tailings piles in Saskatchewan area provide a perfect analogy for better understanding the subglacial hydraulic conditions that likely existed beneath Quaternary ice sheets. For instance, the drainage pattern below a tailings pile could be explored using a combination of field instrumentation and groundwater modelling.
- The newly developed lateral stress oedometer could be used in other research projects. For instance, it is feasible to measure the $\overline{B}$ values of foundation materials of tailings piles in the lab using this equipment. The outcome of such a research project might be extremely valuable for the stability analysis of tailings piles.

References

Airey, D. W., 1984: Clays in simple shear apparatus. *PhD thesis, Cambridge University Engineering Department, Cambridge, UK*.

Al-Tabbaa, A., 1984: Anisotropy of clay. *MPhil thesis, Cambridge University Engineering Department, Cambridge, UK*.

Alley, R. B., Blankenship, D. D., Bentley, C. R. and Rooney, S. T., 1986: Deformation of till beneath Ice Stream B, West Antarctica. *Nature* 322, 57-59.

Banham, P. H., 1977: Glacitectonites in till stratigraphy. *Boreas,* 6, 101-105.

Becker, D. E., Crooks, J. H., Been, K. and Jefferies, M. G., 1987: Work as a criterion for determining in situ and yield stresses in clays. *Canadian Geotechnical Journal* 24, 549-564.

Benn, D. I. and Evans, D. J., 1996: The interpretation and classification of subglacially-deformed materials. *Quaternary Science Reviews* 15, 23-32.

Blake, E. W. and Clake, G.K.C. 1989: In situ bed strain measurements beneath a surge-type glacier (abstract). *EOS* 70, 1084.

Boulton, G. S. and Jones, A. S., 1979: Stability of temperate ice caps and ice sheets resting on beds of deformable sediment. *Journal of Glaciology* 24, 29-44.

Boulton, G. S. and Hindmarsh, R.C.A., 1987: Sediment deformation beneath glaciers: rheology and geological consequences. *Journal of Geophysical Research* 92, 9059-9082.

Boulton, G. S. and Dobbie, K. E., 1993: Consolidation of sediments by glaciers: relations between sediment geotechnics, soft-bed glacier dynamics and subglacial ground-water flow. *Journal of Glaciology* 39, 26-44.

Boulton, G. S., 1996: Theory of glacial erosion, transport and deposition as a consequence of subglacial sediment deformation. *Journal of Glaciology* 42, 43-62.

BSI, 1990a: British Standard 1377-6: 1990 - Methods of test for soils for civil engineering purposes. Consolidation and permeability tests in hydraulic cells and with pore pressure measurement, BSI British Standards, London, UK.

BSI, 1990b: British Standard 1377-5: 1990 - Methods of test for soils for civil engineering purposes. Compressibility, permeability and durability tests, BSI British Standards, London, UK.

Brooker, E. N. and Ireland, H. O., 1965: Earth pressures at rest related to stress history. *Canadian Geotechnical Journal* 11(1), 1-15.

Burland, J. B., 1990: On the compressibility and shear strength of natural clays. *Geotechnique* 40(3), 329-378.

Butterfield, R., 1979: A natural compression law for soils. *Geotechnique* 29(4), 469-480.

Casagrande, A., 1936: The determination of preconsolidation load and its practical significance. *Proceedings, 1st International Conference on Soil Mechanics, Cambridge* Vol.3, 60-64.

Christiansen, E. A., 1968: Pleistocene stratigraphy of the Saskatoon area, Saskatchewan, Canada. *Canadian Journal of Earth Sciences* 5, 1167-1173.

Christiansen, E. A., 1992: Pleistocene stratigraphy of the Saskatoon area, Saskatchewan, Canada: an update. *Canadian Journal of Earth Sciences* 29, 1767-1778.

Colmenares, J. E., 2001: Suction and volume changes of compacted sand bentonite mixtures. *PhD thesis, University of London, Imperial College*, 112-141.

Dalton, J.C.P. and Hawkins, P.G., 1982. Fields of Stress- Some measurements of the in situ stress in a meadow in the Cambridgeshire countryside. *Ground Engineering*, May 1982.

Douma, J., and Helbig, K., 1990. Shear-wave splitting in shallow clays observed in a multi-offset and walk-around VSP. *Geologie en Mijnbouw*, 69 (4), 417-428.

Drescher, A. and de Jong, G., 1972: Photoelastic verification of a mechanical model for the flow of a granular material. *J. Mech. Phys. Solids,* 20(5), 337-351.

Dyvik, R., Laclasse, S. and Martin, R., 1985: Coefficient of lateral stress from oedometer cell. *Proceedings of the Eleventh International Conference on Soil mechanics and foundation engineering, San Francisco,* V2, 1003-1006.

Echelmeyer, K. and Wang, Z. X., 1987: Direct observation of basal sliding and deformation of basal drift at sub-freezing temperatures. *Journal of Glaciology* 33, 89-98.

Engelhardt, H., Humphrey, N., Kamb, B. and Fahnestock, M., 1990: Physical conditions at the base of a fast moving Antarctic ice stream. *Science* 248, 57-59.

Eybergen, F. A., 1987: Glacier snout dynamics and contemporary push moraine formation at the Turtmannglacier, Wallis, Switzerland. *Tills and Glaciotectonics*, Balkema, Rotterdam, 217-233.

Feeser, V., 1988: On the mechanics of glaciotectonic contortion of clays. *Balkema, Rotterdam,* 63-76.

Flint, R. F., 1971: *Glacial and Quaternary Geology*, John Wiley and Sons Inc., New York, 892 pages.

Fountain, A. G., 1994: Borehole water-level variations and implications for the subglacial hydraulics of South Cascade Glacier, Washington State, U.S.A. *Journal of Glaciology* 40(135), 293-304.

Fowler, A. C., 2003: On the rheology of till. *Annals of Glaciology* 37, 55-59.

Gareau, L. F., Molenkamp, F., Sharma, J. and Hegtermans, B., 2004: Engineering geology of glaciated soils, *Proceedings of the Skempton Memorial Conference, London.*

Hart, J. K., 1995: Subglacial erosion, deposition and deformation associated with deformed bed. *Progress in Physical Geography* 19 173-191.

Hart, J. K. and Boulton, G. S., 1991: The inter-relation of glaciotectonite and glaciodepositional processes within the glacial environment. *Quaternary Science Reviews* 10, 335-350.

Haug, M. D., 2005: Personal communications.

Hindmarsh, R. C., Boulton, G. S. and Hutter, K., 1989: Modes of operation of thermo-mechanically coupled ice sheets. *Ann. Glaciol.* 12, 57-69

Holtz, R. D. and Kovacs, W. D., 1981: *An Introduction to Geotechnical Engineering*, Prentice Hall, New Jersey, 733 pages.

Hooke, R. Le B. 1984: On the role of mechanical energy in maintaining subglacial water conduits at atmospheric pressure. *Journal of Glaciology* 30, 180-187

Howell, D., Bchringer, R. and Veje, C., 1999: Stress fluctuations in a 2D granular Couette experiment: a continuous transition. *Phys. Rev. Lett.,* 82(96), 5241-5244.

Iverson, R. M., Reid, M. E., Iverson, N. R., LaHusen, R. G., Logan, M., Mann, J. E. and Brien, D. L., 2000: Acute sensitivity of landslide rates to initial soil porosity. *Science*, 290(5491), 513-516.

Iverson, N. R., Hooyer, T. S., and Baker, R. W., 1997: A ring-shear device for the study of till deformation: Tests on till with contrasting clay contents. *Quaternary Science Reviews* 16, 1057-1066.

Iverson, N. R. and Iverson, R. M., 2000: Distributed shear of subglacial till due to Coulomb slip. *Journal of Glaciology* 47(158), 481-488.

Kamb, W. B. 1991: Rheological nonlinearity and flow instability in the deforming-bed mechanism of ice stream motion. *Journal of Geophysical Research* 96, 16585-16595.

Kavvadas, M. J., 1982: Non-linear consolidation around driven piles in clays, *Ph.D. Thesis, Massachusetts Institute of Technology, Cambridge, USA*.

Khera, R. P. and Schulz, H., 1984: Past consolidation stress estimates in Cretaceous clay. *ASCE, Journal of Geotechnical Engineering* 110(2), 189-202.

Lade, P. V. and Duncan, J. M., 1973: Cubical triaxial tests on cohesionless soil. ASCE, *Journal of the Soil Mechanics and Foundation Engineering, ASCE,* 99(10), 793-810.

Lambe, T. W. and Whitman, R. V., 1979: *Soil Mechanics, SI Version*. John Wiley & Sons.

Liu, G. H. and 6 others, 1995: Force fluctuations in bead packs. *Science,* 269(5223), 513-515.

Logan, J. M et al., 1992: Fabrics of experimental fault zones: their development and relation to mechanical behaviour. *Fault mechanics and transport properties of rocks,* London, Academic Press.

Mandl, G., de Jong, N. J. and Maltha, A., 1977: Shear zones in granular material – an experimental study of their structure and mechanical genesis. *Rock Mechanics* 9(2-3), 95-144.

Moore, P. L. and Iverson, N. R., 2002: Slow episodic shear of granular materials regulated by dilatant strengthening. *Geology* 30(9), 843-846.

Morgan, J. K. and Boettcher, M. S. 1999: Numerical simulations of granular shear zones using the distinct-element method. I. Shear zone kinematics and the micromechanics of localization. *Journal of Geophysical Research* 104, 2721-2732.

Oikawa, H., 1987: Compression curve of soft soils. *Soils and Foundations* 27(3), 99-104.

Onitsuka, K., Hong, Z., Hara, Y. and Yoshitake, S., 1995: Interpretation of oedometer test data for natural clays. *Soils and Foundations* 35(3), 61-70.

PDE Solutions Inc., 2005: FlexPDE Product Overview and Manual, http://www.pdesolutions.com/product.html.

Roscoe, K. H. and Burland, J. B., 1968: On the generalized stress-strain behaviour of wet clay. In *Engineering Plasticity*, Cambridge University Press, 535-609.

Roscoe, K. H., Schofield, A.N. and Wroth, C. P., 1958: On the yielding of soils. *Geotechnique* 8, 22-52.

Sauer, E. K. and Christiansen, E. A., 1991: Preconsolidation pressures in the Battleford Formation, southern Saskatchewan, Canada. *Canadian Journal of Earth Sciences* 28, 1613-1623.

Sauer, E. K., Egeland, A. K. and Christiansen, E. A., 1993: Compression characteristics and index properties of tills and intertill clays in southern Saskatchewan, Canada. *Journal of Glaciology* 40(135), 293-304.

Sauer, E. K., Gareau, L. F. and Christiansen, E. A., 1990: Softening of overconsolidated Cretaceous clays by glacial erosion. *Quarterly Journal of Engineering geology* 20, 307-324.

Schokking, F., 1998: Anisotropic geotechnical properties of a glacially overconsolidated and fissured clay, *PhD Thesis, Delft University of Technology, Delft, The Netherlands*.

Schreiner, B. T., 1990: Lithostratigraphic correlation of Saskatchewan tills, a mirror image of Cretaceous bedrock, *PhD Thesis, University of Saskatchewan, Saskatoon, Canada*.

Senneset, K., 1989: A new oedometer with splitted ring for the measurement of lateral stresses. *Proceedings of the Twelfth International Conference on Soil mechanics and foundation engineering, Rio de Janeiro*, V1, 115-118.

Shaw, R. J. and Hendry, M. J., 1998: Hydrogeology of a thick clay till and cretaceous clay sequence, Saskatchewan, Canada, *Canadian Geotechnical Journal,* 35(6) 1041-1052.

Shreve, R. L. 1972: Movement of water in glaciers. *Journal of Glaciology* 11, 205-214.

Song, L., Fujiwara, T. and Karube, D., 1995: Lateral stress and pore pressure behaviour in oedometer test. *Compression and Consolidation of Clayey Soils, Balkema, Rotterdam*, 177-182.

Sridharan, A. and Sreepada Rao, A., 1981: Rectangular hyperbola fitting method for one dimensional consolidation. *Geotechnical Testing Journal* 4(4), 161-168.

Taylor, D. W., 1948: *Fundamentals of Soil Mechanics*, John Wiley and Sons Inc, New York, 700 pages.

Timoshenko, S. P. and Goodier, J. N. 1970: *Theory of Elasticity*, McGraw-Hill Engineering Mechanics Series, Mc-Graw Hill Book Company, New York.

Tulaczyk, S., Kamb, W. B. and Engelhardt, H. F. 2000: Basal mechanics of Ice Stream B, West Antarctica: 1. Till mechanics. *Journal of Geophysical Research* 105, 463-481.

Weertman, J. 1979: The unsolved general glaciers sliding problem. *Journal of Glaciology* 23(89), 97-115.

Wood, D. M., 1992: *Soil Behaviour and Critical State Soil Mechanics*. Cambridge University Press, New York.

Whittle, A. J. and Kavvadas, M., 1994: Formulation of the MIT-E3 constitutive model for overconsolidated clays. *Journal of Geotechnical Engineering division, ASCE* 120(1), 173-198.

Whittle, R., 2004. Personal communications.

APPENDIX A – A Generalized Approach for the Analysis of Lateral Stress Anisotropy

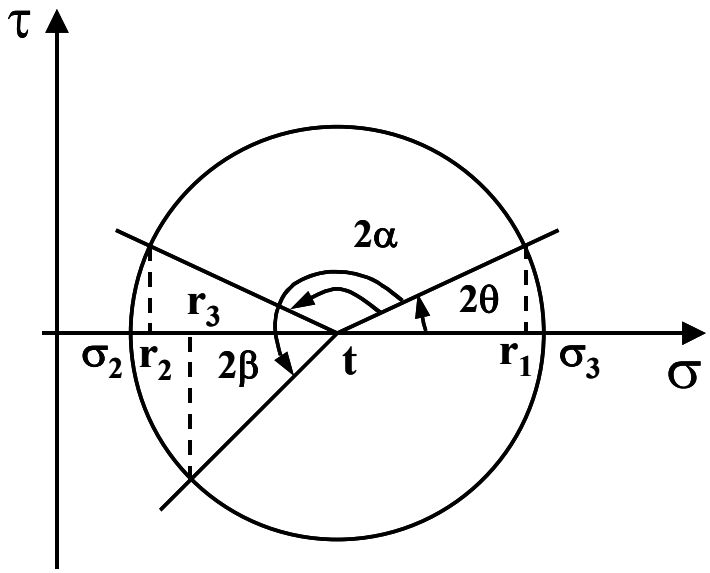

Set $-\frac{\pi}{2} \le \theta \le \frac{\pi}{2} \qquad 0 < \alpha < \pi \qquad 0 < \beta < \pi$

And

$$t = \frac{1}{2}(\sigma_2 + \sigma_3)$$

$$r = \frac{1}{2}(\sigma_3 - \sigma_2)$$

Obviously,

$$r_1 - t = r\cos 2\theta \tag{1}$$

$$r_2 - t = r\cos(2\theta + 2\alpha) \tag{2}$$

$$r_3 - t = r\cos(2\theta + 2\beta) \tag{3}$$

Equations (2) and (3) can be transformed as

$$r_2 - t = r(\cos 2\alpha \cos 2\theta - \sin 2\alpha \sin 2\theta)$$

$$r_3 - t = r(\cos 2\beta \cos 2\theta - \sin 2\beta \sin 2\theta)$$

Further,

$$(\sin 2\beta)(r_2 - t) = r(\cos 2\alpha \cos 2\theta \sin 2\beta - \sin 2\alpha \sin 2\theta \sin 2\beta) \quad (4)$$

$$(\sin 2\alpha)(r_3 - t) = r(\cos 2\beta \cos 2\theta \sin 2\alpha - \sin 2\beta \sin 2\theta \sin 2\alpha) \quad (5)$$

Equation (4)-(5) yields

$$(\sin 2\beta)(r_2 - t) - (\sin 2\alpha)(r_3 - t) = r(\cos 2\theta)[\sin(2\beta - 2\alpha)] \quad (6)$$

Substituting (1) into (6) gives

$$(\sin 2\beta)(r_2 - t) - (\sin 2\alpha)(r_3 - t) = (r_1 - t)\sin(2\beta - 2\alpha) \quad (7)$$

Therefore,

$$t = \frac{r_1 \sin(2\beta - 2\alpha) - r_2 \sin 2\beta + r_3 \sin 2\alpha}{\sin 2\alpha - \sin 2\beta + \sin(2\beta - 2\alpha)} \quad (8)$$

Equations (2) and (3) can also be transformed as

$$(\cos 2\beta)(r_2 - t) = r(\cos 2\alpha \cos 2\theta \cos 2\beta - \sin 2\alpha \sin 2\theta \cos 2\beta) \quad (9)$$

$$(\cos 2\alpha)(r_3 - t) = r(\cos 2\beta \cos 2\theta \cos 2\alpha - \sin 2\beta \sin 2\theta \cos 2\alpha) \quad (10)$$

Equation (9)-(10) gives

$$(\cos 2\beta)(r_2 - t) - \cos 2\alpha(r_3 - t) = r \sin 2\theta \sin(2\beta - 2\alpha)$$

Thus,

$$[(\cos 2\beta)(r_2 - t) - (\cos 2\alpha)(r_3 - t)]^2 / \sin^2(2\beta - 2\alpha) = r^2 \sin^2 2\theta \quad (11)$$

and equation (1) can be transformed as

$$(r_1 - t)^2 = r^2 \cos^2 2\theta \quad (12)$$

Equation (11)-(12) gives

$$[(\cos 2\beta)(r_2 - t) - (\cos 2\alpha)(r_3 - t)]^2 / \sin^2(2\beta - 2\alpha) + (r_1 - t)^2 = r^2$$

Or

$$r = \frac{1}{\sin(2\beta - 2\alpha)} \left\{ [(\cos 2\beta)(r_2 - t) - (\cos 2\alpha)(r_3 - t)]^2 + \sin^2(2\beta - 2\alpha)(r_1 - t)^2 \right\}^{1/2}$$

Or by using equation (7) it can be rewritten as

$$r = \frac{1}{\sin(2\beta - 2\alpha)}\left[(r_2 - t)^2 + (r_3 - t)^2 - 2(r_2 - t)(r_3 - t)\cos(2\beta - 2\alpha)\right]^{1/2} \quad (13)$$

From equations (1), (8) and (13),

$$\theta = \pm\frac{1}{2}\cos^{-1}\left(\frac{r_1 - t}{r}\right) \quad (14)$$

APPENDIX B – Derivation of Equation (6.18)

From,

$$p' = \sigma' - \frac{\tau}{3} \tag{1}$$

$$q = 2\tau \tag{2}$$

And

$$\eta = q / p' \tag{3}$$

$$\frac{p'}{p'_0} = \frac{M^2}{M^2 + \eta^2} \tag{4}$$

We have

$$p'_0 M^2 = p' M^2 + p' \eta^2 \tag{5}$$

$$p'_0 M^2 = (\sigma' - \frac{\tau}{3}) M^2 + (\sigma' - \frac{\tau}{3}) \left(\frac{2\tau}{(\sigma' - \frac{\tau}{3})} \right)^2 \tag{6}$$

Equation (6) can be rearranged as

$$\left(\frac{M^2 + 36}{9M^2} \right) \tau^2 + \left(\frac{p'_0 - 2\sigma'}{3} \right) \tau + \left(\sigma'^2 - p'_0 \sigma' \right) = 0 \tag{6.18}$$

APPENDIX C – Derivation of Equations (6.23) & (6.24)

From,

$$v = N + (\kappa - \lambda)\ln p_0' - \kappa \ln p' \tag{1}$$

We have

$$\frac{\partial v}{\partial \sigma'} = \frac{(\kappa - \lambda)}{p_0'}\frac{\partial p_0'}{\partial \sigma'} - \frac{\kappa}{p'}\frac{\partial p'}{\partial \sigma'} \tag{2}$$

For consolidation with constant shearing (see Section 6.5.3), we have

$$p' = \sigma' - \frac{\tau_{surf}}{3}$$

$$q = 2\tau_{surf}$$

Therefore,

$$\frac{\partial p'}{\partial \sigma'} = 1 \tag{3}$$

From MCC model, we have

$$\eta = q / p' \tag{4}$$

$$\frac{p'}{p_0'} = \frac{M^2}{M^2 + \eta^2} \tag{5}$$

From equation (4) and equation (3), we have

$$\frac{\partial \eta}{\partial \sigma} = -\frac{q}{(p')^2}\frac{\partial p'}{\partial \sigma'} = -\frac{q}{(p')^2} \tag{6}$$

Equation (5) can be rewritten as

$$p_0' = \frac{M^2 + \eta^2}{M^2} p' = p' + \frac{\eta^2}{M^2} p' \tag{7}$$

Therefore,

$$\frac{\partial p_0'}{\partial \sigma'} = 1 \cdot \frac{\partial p'}{\partial \sigma'} + \frac{\eta^2}{M^2} \cdot \frac{\partial p'}{\partial \sigma'} + p'\left(\frac{2\eta}{M^2}\right)\frac{\partial \eta}{\partial \sigma'} \tag{8}$$

Substituting equations (3) (6) into equation (8) yields

$$\frac{\partial p_0'}{\partial \sigma'} = 1 - \frac{\eta^2}{M^2} \tag{9}$$

Combining equations (2) (3) (7) and (9) yields

$$\frac{\partial v}{\partial \sigma'} = \frac{(\kappa - \lambda)}{\left(\frac{M^2 + \eta^2}{M^2}\right)p'}\left(1 - \frac{\eta^2}{M^2}\right) - \frac{\kappa}{p'} \tag{10}$$

Equation (10) can be transformed as

$$\frac{\partial v}{\partial \sigma'} = \left(\frac{\kappa}{p'}\right)\left(\frac{-2\eta^2}{M^2 + \eta^2}\right) - \left(\frac{\lambda}{p'}\right)\left(\frac{M^2 - \eta^2}{M^2 + \eta^2}\right) \tag{6.23}$$

Considering equations (6.19a) (6.19b) and

$$v = 1 + e$$

Equation (11) can be rewritten as

$$\frac{\partial e}{\partial \sigma'} = a_s\left(\frac{-2\eta^2}{M^2 + \eta^2}\right) - a_v\left(\frac{M^2 - \eta^2}{M^2 + \eta^2}\right) \tag{6.24}$$